

8-15-2014

## POPC Phospholipid Bilayer Failure Under Biaxial Deformations Using Molecular Dynamics

Michael Anthony Murphy

Follow this and additional works at: <https://scholarsjunction.msstate.edu/td>

---

### Recommended Citation

Murphy, Michael Anthony, "POPC Phospholipid Bilayer Failure Under Biaxial Deformations Using Molecular Dynamics" (2014). *Theses and Dissertations*. 3562.  
<https://scholarsjunction.msstate.edu/td/3562>

This Graduate Thesis - Open Access is brought to you for free and open access by the Theses and Dissertations at Scholars Junction. It has been accepted for inclusion in Theses and Dissertations by an authorized administrator of Scholars Junction. For more information, please contact [scholcomm@msstate.libanswers.com](mailto:scholcomm@msstate.libanswers.com).

POPC phospholipid bilayer failure under biaxial deformations using molecular dynamics

By

Michael Anthony Murphy

A Thesis  
Submitted to the Faculty of  
Mississippi State University  
in Partial Fulfillment of the Requirements  
for the Degree of Master of Science  
in Biomedical Engineering  
in the Department of Agricultural and Biological Engineering

Mississippi State, Mississippi

August 2014

Copyright by  
Michael Anthony Murphy  
2014

POPC phospholipid bilayer failure under biaxial deformations using molecular dynamics

By

Michael Anthony Murphy

Approved:

---

Lakiesha N. Williams  
(Major Professor)

---

Mark F. Horstemeyer  
(Committee Member)

---

Rajkumar Prabhu  
(Committee Member)

---

Steven R. Gwaltney  
(Committee Member)

---

Tonya W. Stone  
(Committee Member)

---

Steven H. Elder  
(Graduate Coordinator)

---

Jason M. Keith  
Interim Dean  
Bagley College of Engineering

Name: Michael Anthony Murphy

Date of Degree: August 15, 2014

Institution: Mississippi State University

Major Field: Biomedical Engineering

Major Professor: Lakiesha N. Williams

Title of Study: POPC phospholipid bilayer failure under biaxial deformations using molecular dynamics

Pages in Study: 116

Candidate for Degree of Master of Science

Mechanical injuries to the cell often lead to disruptions of the cell's phospholipid bilayer membrane and potential detrimental effects including cell death. Understanding the mechanical states required to disrupt the phospholipid bilayer would result in better multiscale constitutive models and further knowledge of cell injury. The objectives of this research were to perform biaxial deformations of the phospholipid bilayer to quantify phospholipid bilayer disruption and to identify potential parameters that can be used in multiscale constitutive equations. We show that the von Mises stress, 26.6-61.1, increases linearly with the von Mises strain rate,  $1.7e8$ - $6.7e8$ , and that the strain at failure is dependent on the stress state with non- and equibiaxial being the most detrimental when failing at  $<.73$  von Mises strain. Understanding the effects of nanoscale mechanical trauma to the cell provides a better understanding of cell injury and may provide insight regarding initiation and progression of cell damage.

## DEDICATION

This research is dedicated to Mary K. Murphy, my wife, who has given me strength and supported me through this process. She has done so much to help me focus on school and research rather than the typical distractions of life.

To Aaron Moses Murphy, my son, who continues to serve as my motivation to work and still be home as much as possible. Bedtime reading was the one distraction I refused to give up—although often done over Skype.

To Charles and Sharlene Murphy, my parents, who pushed me to be curious and to explore my interests no matter where they took me and supported me to the best of their abilities.

To all my friends and family who both continue to help guide me and give me projects to play with as I travel through this life.

And to God who has given me guidance, strength, and patience to get through this process and given me blessings that I did not even know I needed as well as the individuals in my life who have helped me through it.

## ACKNOWLEDGEMENTS

I would like to acknowledge groups and individuals who contributed to the completion of this work. A special thanks to Dr. Lakiesha Williams, my major professor, and Dr. Rajkumar Prabhu who served as guides both in work and life and were always willing to listen when truly needed. I also would like to acknowledge Steven Gwaltney, Mark Horstemeyer, and Tonya Stone, the remaining members of my graduate committee who have been a huge source of help with completing this work and often made themselves available for discussions and to give feedback. They have given so much time and knowledge helping me throughout this study.

I would also like to acknowledge the support of the professors in the Department of Agricultural and Biological Engineering (ABE) as well as the rest of Mississippi State University. So many are willing to help when they do not already have a vested interest in a project and willing to meet when though they have such busy schedules already.

I would like to acknowledge my fellow graduate students who are going through this process as well and who are always willing to give guidance, help, knowledge, or to just lend an ear whenever needed.

And as a final acknowledgement, I acknowledge the support and resources of the Department of Agricultural and Biological Engineering and the Center for Advanced Vehicular Systems (CAVS) without which this study would not have been possible. This is especially true of the computational resources provided through CAVS.

## TABLE OF CONTENTS

DEDICATION .....	ii
ACKNOWLEDGEMENTS .....	iii
LIST OF TABLES .....	vii
LIST OF FIGURES .....	viii
CHAPTER	
I. MOTIVATION .....	1
1.1 Research Objectives .....	2
1.2 Overview .....	2
II. INTRODUCTION .....	3
2.1 Molecular Dynamics .....	3
2.1.1 Background .....	3
2.1.2 Force Fields .....	5
2.1.3 CHARMM Force Field .....	6
2.1.4 Advantages and Disadvantages .....	7
2.2 Phospholipid Bilayer .....	7
2.2.1 Function .....	7
2.2.2 Structure .....	9
2.2.3 Experimental Methods .....	9
2.2.4 Mechanical Properties .....	11
2.2.5 Types of Phospholipids .....	12
2.2.6 Previous Simulations .....	14
2.2.6.1 Equilibration .....	14
2.2.6.2 Deformations .....	15
2.3 Molecular Mechanics Background .....	17
2.3.1 Biological Materials .....	17
2.3.2 Virial Stress .....	18
2.4 Traumatic Brain Injury .....	19
2.5 Multiscale Modeling .....	21
2.5.1 Background .....	21
2.5.2 Constitutive Equations .....	23
2.5.3 Benefits .....	24



2.5.4	Error .....	25
2.5.5	Verification .....	25
2.5.6	Validation.....	26
III.	METHODS .....	27
3.1	System Equilibration.....	27
3.2	Deformation Simulations .....	30
3.3	Analysis.....	32
3.3.1	Image Analysis.....	32
3.3.2	Quantitative Analysis.....	33
3.3.2.1	Surface Tension .....	33
3.3.2.2	Von Mises Stress and Strain .....	35
3.3.2.3	Calculation of Elastic Properties.....	36
IV.	RESULTS .....	37
4.1	Strain Rate Comparison .....	37
4.2	Phospholipid Bilayer Size Comparison .....	48
4.3	Stress State Comparison .....	56
4.4	Overall Curve Trends.....	72
4.5	Elastic Properties .....	74
V.	DISCUSSION .....	76
5.1	Area per Lipid.....	76
5.2	Surface Tension vs von Mises Stress.....	76
5.3	Selection of Deformation Rates .....	79
5.4	Strain Rate Dependency.....	81
5.4.1	Effect of Strain Rate.....	81
5.4.2	Effect on Pore Formation and Water Penetration .....	82
5.4.3	Comparison with Literature .....	83
5.5	Phospholipid Bilayer Size Effect.....	85
5.6	Stress States .....	86
5.7	Elastic Constants.....	89
5.8	Relevance.....	89
5.9	Multiscale Modeling.....	90
5.10	Future Work.....	91
5.10.1	Verification and Validation.....	91
5.10.1.1	Further Analysis and Validation .....	91
5.10.1.2	Comparative Studies for Verification .....	91
5.10.1.3	Comparative Study with Other Force Fields .....	92
5.10.2	Add Model Complexity .....	92
5.10.3	Other Stress States .....	93
VI.	CONCLUSIONS.....	95

REFERENCES .....96

APPENDIX

A. FORCE FIELD PARAMETERS .....101

B. MODEL RELAXATION OF THE 72x1y0 CASE .....107

C. DEFORMATION REVERSAL OF THE 72x1y0 CASE.....112

## LIST OF TABLES

3.1	Summary of Atom and Molecule Count with Corresponding Sizes in Nanometers for Each Structure.....	28
3.2	Summary of Deformation Simulations.....	31
4.1	Mechanical Properties of the Seventy-Two Phospholipid Bilayer Under Strip Biaxial Tension at Different von Mises Strain Rates.....	38
4.2	Mechanical Properties of the Phospholipid Bilayer Under Strip Biaxial Tension at a von Mises Strain Rate of $6.7e8$ /sec for Different Sizes .....	49
4.3	Mechanical Properties of the Seventy-Two Phospholipid Bilayer Under Different Stress States at a von Mises Strain Rate of $6.7e8$ /sec .....	57

## LIST OF FIGURES

2.1	Generic Neuron Cell Diagram .....	8
2.2	Fluid Mosaic Model of the Cell Membrane.....	9
2.3	Labeled line diagram of POPC displaying the components making the phospholipid structure.....	13
2.4	POPC molecule with hydrophobic and hydrophilic regions labeled. ....	14
3.1	Size comparisons of the equilibrated lipid bilayer structures .....	29
3.2	Representative perpendicular (top) view of the deformations performed where the initial structure is represented by a solid black line and the deformed structure by a lighter dashed line .....	30
3.3	Side view of the phospholipid bilayer with all lipids hidden for the 72x1y0 case.....	32
3.4	Comparison of true box height and a linear estimate of phospholipid bilayer height. ....	35
4.1	Pore formation during phospholipid bilayer deformations are shown for strip biaxial tension at von Mises equivalent strain rates of $1.7e8$ , $5.0e8$ , and $6.7e8$ /s.....	38
4.2	Surface tension-von Mises strain curve displaying the effect of the von Mises strain rate. ....	39
4.3	Von Mises stress-strain curve displaying the effect of the von Mises strain rate.....	40
4.4	Pore count for different von Mises strain rates. ....	42
4.5	Area density for different von Mises strain rates.....	43
4.6	Total pore area for different von Mises strain rates .....	44
4.7	Mean pore area for different von Mises strain rates. ....	45

4.8	Area fraction for different von Mises strain rates. ....	46
4.9	Mean nearest neighbor distance for different von Mises strain rates. ....	47
4.10	Correlation of von Mises Strain Rate and the von Mises Stress at the first peak results in a linear trend. ....	48
1.1	Von Mises stress-strain curve displaying the effect of phospholipid bilayer size. ....	49
4.11	Pore count for different phospholipid bilayer size. ....	51
4.12	Area density for different phospholipid bilayer size. ....	52
4.13	Total pore area for different phospholipid bilayer size. ....	53
4.14	Mean pore area for different phospholipid bilayer size. ....	54
4.15	Area fraction for different phospholipid bilayer size. ....	55
4.16	Mean nearest neighbor distance for different phospholipid bilayer size. ....	56
4.17	Von Mises stress-strain curve displaying the effect of the stress state. ....	58
4.18	Surface tension-true strain curve displaying the effect of the stress state. ....	59
4.19	Pore count for different stress states. ....	61
4.20	Area density for different stress states. ....	62
4.21	Total pore area for different stress states. ....	63
4.22	Mean pore area for different stress states. ....	64
4.23	Area fraction for different stress states. ....	65
4.24	Mean nearest neighbor distance for different stress states. ....	66
4.25	Von Mises stress-strain curve for the strip biaxial deformation conditions resulting in a von Mises strain rate of $6.7e8$ /sec. ....	68
4.26	Plot of von Mises stress and strain for the equibiaxial deformation conditions resulting in von Mises strain rate of $6.7e8$ /sec. ....	69
4.27	Plot of von Mises stress and strain for the non-equibiaxial deformation conditions resulting in a von Mises strain rate of $6.7e8$ /sec. ....	70

4.28	Von Mises stress-strain curve for the uniaxial deformation conditions resulting in a von Mises strain rate of $6.7 \times 10^8$ /sec. ....	71
4.29	Examination of the strain space for different stress states. ....	72
4.30	Linear portions of the 72x2.8y2.7 case. ....	73
4.31	Elastic modulus determination using the uniaxial stress-strain curve and a trendline. ....	75
5.1	Comparison of the surface tension-von Mises strain curves and the von Mises stress-strain curves. ....	79
5.2	Comparison of principle pressures (stress) and overall pressure for the 72x4y0 (left) and 72x2.8y2.7 (right) cases. ....	87

## CHAPTER I

### MOTIVATION

Traumatic brain injury (TBI) has become a great concern for many nations of the world. In the United States alone, there are approximately 1.7 million new cases every year resulting in both human and economic losses (Faul, Xu, Wald, & Coronado, 2010). Additionally, a multitude of symptoms, potentially including long-term disability and death, may be present in each case based on the severity of the injury (Faul et al., 2010). Despite the large number of cases and potentially severe side effects, there is still much that is not understood about TBI. This is partially due to the complexity of TBI. However, through the use of finite element simulations, macroscale details of traumatic brain injuries are being discovered (R. Prabhu, 2014). These finite element simulations consider the simulated structure as a whole and can be complemented by simulations and experiments exploring lower length scale phenomena.

Investigations into nanoscale cellular mechanics can then be implemented into existing finite element simulations through multiscale damage parameters. Due to the complexity of the cell and the role of the cell membrane during cell injury, only a representative phospholipid bilayer is used during deformation simulations. Although many studies have examined experimental deformations of the phospholipid bilayer, few studies have performed this examination via simulation and none with the view of multiscale modeling from the atomistic level. Our goal is to provide data from the

nanoscale that will serve to enable more accurate constitutive finite element models in the future and aid the human body simulation research group's development of the human body constitutive model at Mississippi State University.

## **1.1 Research Objectives**

The primary objective of this study is to analyze a simplified phospholipid bilayer for disruption and failure when placed under simulated mechanical loading via molecular dynamics. There are two goals for this study: (i) analyze the effects of different stress states, strain rates, and phospholipid bilayer size on the phospholipid bilayer and (ii) consider properties such as the strains, von Mises stress, and surface tension which are properties that can potentially be passed up to the next length scale of a multiscale model.

## **1.2 Overview**

In this study, we examine computationally the effects of varying the phospholipid bilayer size, the deformation strain rate, and the stress state allowing for analysis of which factors have the greatest effect on pore formation. The equivalent von Mises strain rates are considered in place of x and y individual rates so that multiple stress states can be considered including strip biaxial, equibiaxial, non-equibiaxial, and uniaxial tension.



## CHAPTER II

### INTRODUCTION

#### **2.1 Molecular Dynamics**

The molecular dynamics (MD) simulation method combines aspects of physics, chemistry, mechanics, and biology to create a novel way to examine phenomena that were previously prohibitively difficult or impossible to study using experimental methods. This is particularly useful when considering biological materials which are often complex to test and visualize effectively due to their physical structure being non-uniform and anisotropic. Furthermore, viewing damage to specimens post experimental testing is often difficult because many biological specimens degrade over time. Chemical fixing is often used to prevent degradation, but the process often leads to artifacts and does not allow a mid-experiment view of the current specimen.

##### **2.1.1 Background**

Macroscale properties of materials are greatly affected by sub-macro material structures and their properties (Cranford & Buehler, 2012; M. F. Horstemeyer, 2012). As technology progresses, better methods have been developed for testing and determining the sub-macro properties of materials (M. F. Horstemeyer, 2012). However, experiments are often inefficient due to limitations and costs (M. F. Horstemeyer, 2012). Powerful computational resources have also been increasing, which allows a gain in understanding

by utilizing *in silico* methods (M. F. Horstemeyer, 2012). The boosts in computational power allow for larger models and longer-running simulations which allow for a more thorough examination of phenomena that were previously unexplorable because of cost and time limitations.

Simulation methods pertaining to the quantum scale provide a way to calculate solutions that are the most accurate through the use of wave functions which allow for detailed solutions of the electron locations and atomic interactions (Cranford & Buehler, 2012; M. F. Horstemeyer, 2012; Leach, 2001). Although quantum simulations theoretically have the ability to calculate solutions that are exact in many cases, semi-empirical methods have been developed that calculate approximate solutions (Leach, 2001). Depending on the method, these approximations are achieved by ignoring or approximating portions of the wave functions and the subset of electrons explicitly considered (Leach, 2001). Although these approximations help to reduce the computational cost and time of the simulations, quantum simulations are still extremely expensive computationally leading to the need of simulations using empirical force fields (Leach, 2001). Empirical force fields, which allow for atomic interactions, are described by a simplified set of parameters and functional form of the energy equations rather than a wave function (Leach, 2001). Each atom is treated as an individual unit allowing for much larger simulations, but they cannot be used to calculate the locations of electrons (Leach, 2001).

Molecular dynamics are the result of combining empirical force fields with Newton's equations of motion. At each time step, the current positions and velocities are used to calculate attractive and repulsive forces between each atom and all of its

neighbors within a defined range to determine the velocities and positions for the next time step resulting in a continual history of positions (Cranford & Buehler, 2012). As a consequence of calculating new positions every time step, time steps must be small to avoid simulation instabilities such as losing atoms. Additionally, values must be averaged with respect to time to obtain meaningful information rather than instantaneous values (Cranford & Buehler, 2012; M. F. Horstemeyer, 2012; Leach, 2001).

### **2.1.2 Force Fields**

Results from molecular dynamics simulation results and runtimes are largely reliant on the force field being utilized. As mentioned above, force fields provide necessary information about parameters describing how any individual atom interacts with all the atoms around it along with the functional forms of the energy equations needed to describe them (Leach, 2001). It should be noted that two force fields can define different parameters and functional form of the energy equations for a system and they both be technically correct, but it is not possible to interchange parameters between the two force fields as the parameters are defined based on the derived functional form of the energy equations and one force field may provide a more accurate approximation. These parameters can include properties such as bond, angle, improper, and dihedral coefficients and how long range interactions are calculated. The force field parameters can be derived through a mix of experimental methods and quantum mechanics simulations (Cranford & Buehler, 2012; M. F. Horstemeyer, 2012; Leach, 2001).

Many force fields exist with each having its own unique parameters designed for a specific purpose and is largely restricted to that purpose. The modified embedded atom method (MEAM) is an excellent example of force field specialization because it was

originally designed to model metals where there are no long-range electrostatics (M. F. Horstemeyer, 2012). Although MEAM can be used to effectively predict metal phenomenon such as dislocations and twinning, the use of MEAM in biological simulations is highly limited because it would not capture the much needed long-range interactions (M. F. Horstemeyer).

Alternatively, many force fields have been designed specifically for biological simulations and account for long-range electrostatics. A few of these representative biological force fields are the general AMBER force field (Wang, Wolf, Caldwell, Kollman, & Case, 2004), CHARMM (Chemistry at HARvard Macromolecular Mechanics) (Jeffery B. Klauda et al., 2010), and GROMACS (GRoningen MACHine for Chemical Simulations) (Pronk et al., 2013) which are considered non-reactive force fields. In other words, they do not allow bonds to be broken or created (Cranford & Buehler, 2012).

### **2.1.3 CHARMM Force Field**

The CHARMM36 all-atom lipid parameters are calibrated specifically for lipids (as opposed to general force fields) and corrected the flaw in previous versions ability to run in the NPT ensemble without external pressures being applied or artificially restraining the area by using NPAT (Jeffery B. Klauda et al., 2010). Additionally, CHARMM was originally developed using the TIP3P water model which has become dated and is not as accurate as more modern water models, but to change the water model would potentially require significant revisions to the CHARMM force field itself (Pastor & MacKerell, 2011).

#### **2.1.4 Advantages and Disadvantages**

MD simulations are often computationally expensive due to the requirement of small time steps and the need to perform calculations for all atoms in a simulation. This becomes prohibitive when large systems or phenomena lasting more than a few nanoseconds are simulated. Due to these restrictions, molecular dynamics are often best suited for analyzing very short phenomenon to determine specific mechanisms in a longer series of phenomena. However, the chosen phenomenon can be viewed in great detail allowing for analysis in ways otherwise impossible and provides a view of the most basic properties of materials with force fields that are often transferable between systems (Cranford & Buehler, 2012).

### **2.2 Phospholipid Bilayer**

#### **2.2.1 Function**

In a cell, the most basic functions of the phospholipid bilayer include serving as the primary constituent of membranes where it is a platform for protein placement and inhibits free molecule transport through the membranes. In extension to the transport inhibition, the phospholipid bilayer also serves as a protective barrier by preventing many molecules and organisms from passing through the cell membrane without protein facilitation and help maintain appropriate, and often necessary, internal and external molecular concentrations (Barbee, 2006). During injuries which disrupt the phospholipid bilayer, the ability to fulfil these functions are greatly diminished. Understanding the mechanical states that result in disruption of the lipid bilayer is critical to understanding mechanical injuries to the cell. Any disruption of the bilayer can lead to devastating results for the cell, including the ability of molecules to freely penetrate the bilayer

according to their gradients which can disrupt normal cell functions and can lead to necrosis or apoptosis (Barbee, 2006; Farkas & Povlishock, 2007). One example of a possible injury resulting in bilayer disruption is traumatic brain injury which is believed to be directly influenced by mechanoporation of the phospholipid bilayer. *In vivo* recovery from this mechanoporation has been shown to be less effective than *in vitro* (Farkas & Povlishock, 2007). Therefore, understanding the mechanisms resulting in disruption of the phospholipid bilayer will lead to a better understanding of injuries to cell membranes. The cell membrane can be seen in the cell diagram of a generic neuron in Figure 2.1.

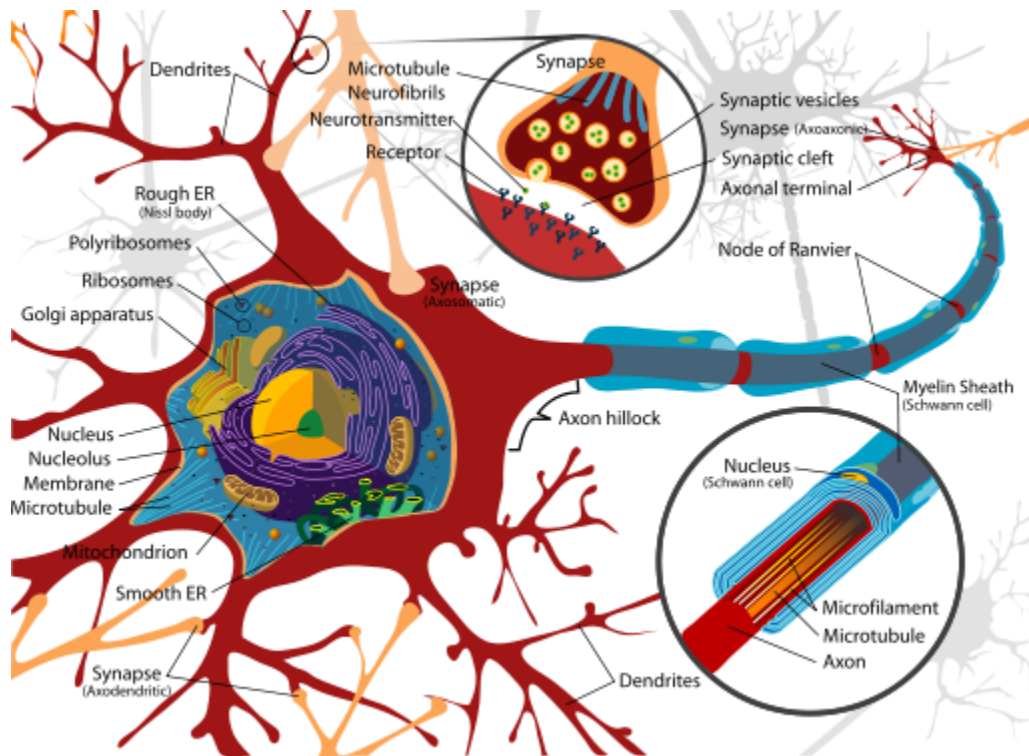


Figure 2.1 Generic Neuron Cell Diagram

Notes: By LadyoffHats (Own work) [Public domain], via Wikimedia Commons, Retrieved September 12, 2012

### 2.2.2 Structure

The structure of phospholipid bilayers were determined in the past using methods such as X-ray diffraction as seen in Worthington and Kharf (1978) and fluorescence spectroscopy as seen in Bramhall (1986). The fluid mosaic model was then developed by Singer and Nicolson (1972). This new model was based on immunofluorescence models performed by others as well as other experimental procedures at the time. They hypothesized in the model that the cell membrane consisted of phospholipids and embedded proteins in a two-dimensional viscous fluid where lipids and proteins could move freely (Singer & Nicolson, 1972). This model remains popular today because it largely captured the general nature of the cell membrane as can be seen in Figure 2.2.

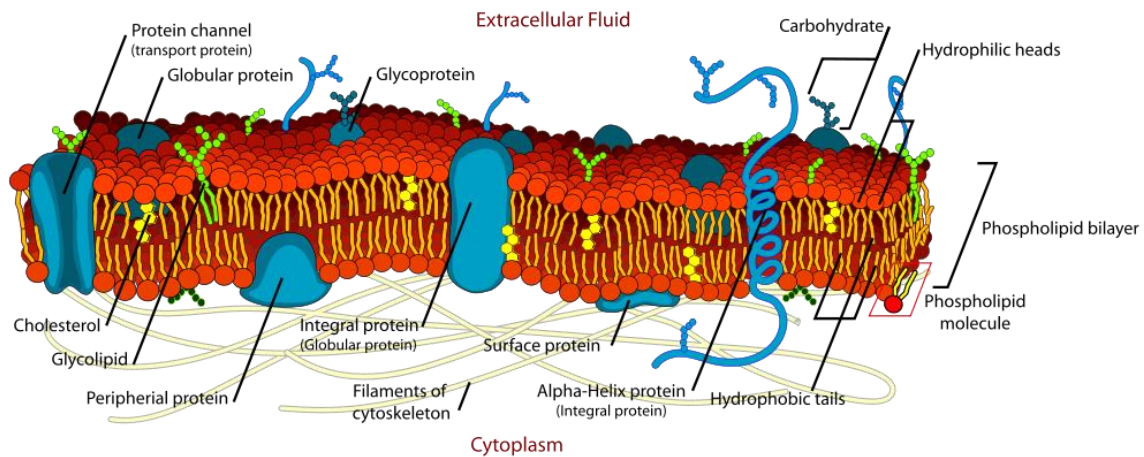


Figure 2.2 Fluid Mosaic Model of the Cell Membrane

Notes: By LadyofHats (Own work) [Public domain], via Wikimedia Commons, Retrieved September May 5, 2014

### 2.2.3 Experimental Methods

Many experimental studies have provided insights into the properties of the lipid bilayer. The fluid nature of the bilayer was officially noted by FRYE and EDIDIN

(1970) who used immunofluorescent antigen markers to observe the movement of the lipids in the cell membrane.

Methods have been developed as a way of deforming cells and the primary constituent of the cell membrane, the phospholipid bilayer, as well. A few of note are micropipette aspiration via a vacuum (E. Evans, V. Heinrich, F. Ludwig, & W. Rawicz, 2003; Evans & Smith, 2011; Needham & Nunn, 1990), electric fields (Thom, 2009), and atomic force microscopy (AFM) (Ovalle-García, Torres-Heredia, Antillón, & Ortega-Blake, 2011; Picas, Milhiet, & Hernández-Borrell, 2012).

Micropipette aspiration has long provided a method of testing phospholipid bilayers. Using this method, a micropipette is used to aspirate phospholipid structures while measuring the pressure which allows for the stress at failure to be determined and elastic moduli to be determined. One example of this is Needham and Nunn (1990) who investigated the effects of cholesterol concentration on the rupture strength of phospholipid vesicles and the area compressibility modulus. Additionally, (E. Evans et al., 2003) used micropipette aspiration to determine defect-limited and cavitation-limited equations for the rupture strength of vesicles in the loading rate range of  $0.01-100\frac{mN}{s}$ .

Alternatively, some, such as Thom (2009), have performed deformation experiments using electric fields and an ionic solution. Despite micropipette aspiration being the most common method for determining mechanical properties, using the electric fields method is necessary at lower temperatures when freezing is an issue (Thom, 2009).

Despite its name, AFM is not the typical device a person typical imagines when they hear the word microscope. Rather, it consists of a cantilever beam equipped with a sharp tip for which a laser and photodiode are used to measure the cantilever deflections



(Picas et al., 2012). The AFM is a diverse tool that can be used in a variety of modes to determine mechanical properties of biological specimen, including living supported bilayers (Picas et al., 2012). Although the resolution of the AFM is similar to that of scanning electron microscopy (SEM), AFM does not require the sample to be fixed in place before imaging and can even still be living (Picas et al.). This fact is a great advantage when dealing with biological specimen because they are constantly changing and the act of chemically fixing a cell will kill it and can leave many artifacts. AFM has also been used to study unsupported phospholipid bilayers and to determine values such as the bending modulus and adhesion constant. However, when using AFM an appropriate elastic model must be selected or the results will not be correct (Ovalle-García et al., 2011; Picas et al., 2012).

#### **2.2.4 Mechanical Properties**

*In vitro* methods have been utilized in attempts to determine phospholipid properties by deforming the phospholipid lipid bilayer previously. Methods utilizing a vacuum and micropipette have been used to experimentally determine values for the strength and moduli of the lipid bilayer under tension for rupture analyses (E. Evans et al., 2003; Evans & Smith, 2011; Needham & Nunn, 1990). Needham and Nunn (1990) reported the area compressibility modulus as  $0.193 \pm .02 \frac{N}{m}$  while Cevc (1993) noted a value of  $0.15 \frac{N}{m}$  for the area compressibility modulus and  $\leq 3GPa$  for the bulk modulus. This enabled pore formation to be examined experimentally but was pressure controlled which limited the control of the deformations. These experiments also proved that the phospholipid bilayer rupture is rate dependent (E. Evans et al., 2003). Additionally,

atomic force microscopy has been used as a method of determining the elastic properties of the lipid bilayer as seen in Ovalle-García et al. (2011) who reported values of  $\kappa = 1.5 \pm .6 \times 10^{-19}$  for the bending modulus and  $w = 4.6 \pm 2.2 \frac{mJ}{m^2}$  for the adhesion constant.

### 2.2.5 Types of Phospholipids

Although the phospholipid bilayer consists of two layers of tightly packed phospholipids with the same overall structure, many different configurations exist resulting in a wide range of phospholipid types. Connected by a glycerol, the headgroup and fatty acid chains vary between phospholipid types allowing a classification system where subunits are used to classify individual types (B. & B., 2013). The headgroups are named based on substituent of the phosphate group (B. & B., 2013). Namely, when the phosphate is attached to serine it forms phosphatidylserine (B. & B., 2013). Similarly, ethanolamine forms phosphatidylethanolamine, choline forms phosphatidylcholine, and polyalcohol inositol forms phosphatidylinositol (B. & B., 2013).

Only 1-Palmitoyl-2-oleoylphosphatidylcholine, also known as POPC and 1-palmitoyl-2-oleoyl-sn-glycero-3-phosphocholine, is considered in the current study. As the name suggests, this phospholipid is comprised of a glycerol backbone, palmitoyl and oleoyl fatty acid chains, a phosphate group, and a choline group. These individual parts can be seen labeled in Figure 2.3. Note that the phosphate group has a net charge and is highly hydrophilic. In contrast, the fatty acid chains are neutrally charged and highly hydrophobic. These two areas are labeled in Figure 2.4. This combination of both hydrophilic and hydrophobic properties in the same molecule give rise to the ability for

phospholipid bilayers to exist and spontaneously form (Bramhall, 1986; Singer & Nicolson, 1972).

Additionally, POPC was one of the phospholipids used to test the CHARMM36 all-atom lipid force field parameters which enforces the assumption it has been investigated extensively and is common (Jeffery B. Klauda et al., 2010). POPC also serves as a representative molecule for the phosphatidylcholine family of phospholipids which comprise a large composition of the cell membrane, albeit they are more prominent in the external leaflet (Fontaine, Adron Harris, & Schroeder, 1979).

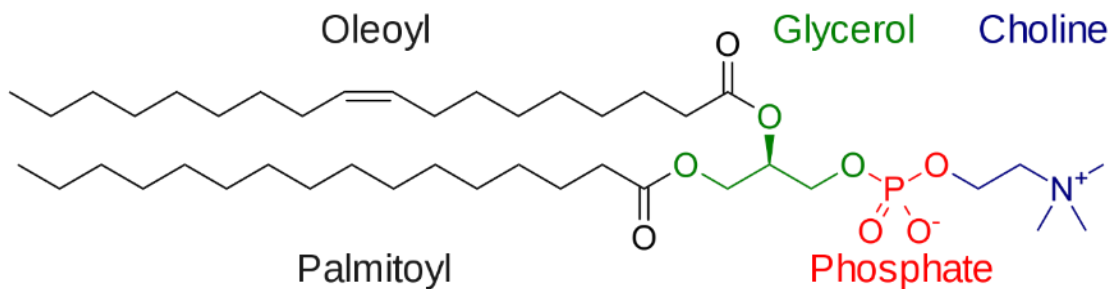


Figure 2.3 Labeled line diagram of POPC displaying the components making the phospholipid structure.

Notes: By VIGNERON, Edgar181 (Own work) [Public domain], via Wikimedia Commons. Retrieved March 1, 2013.

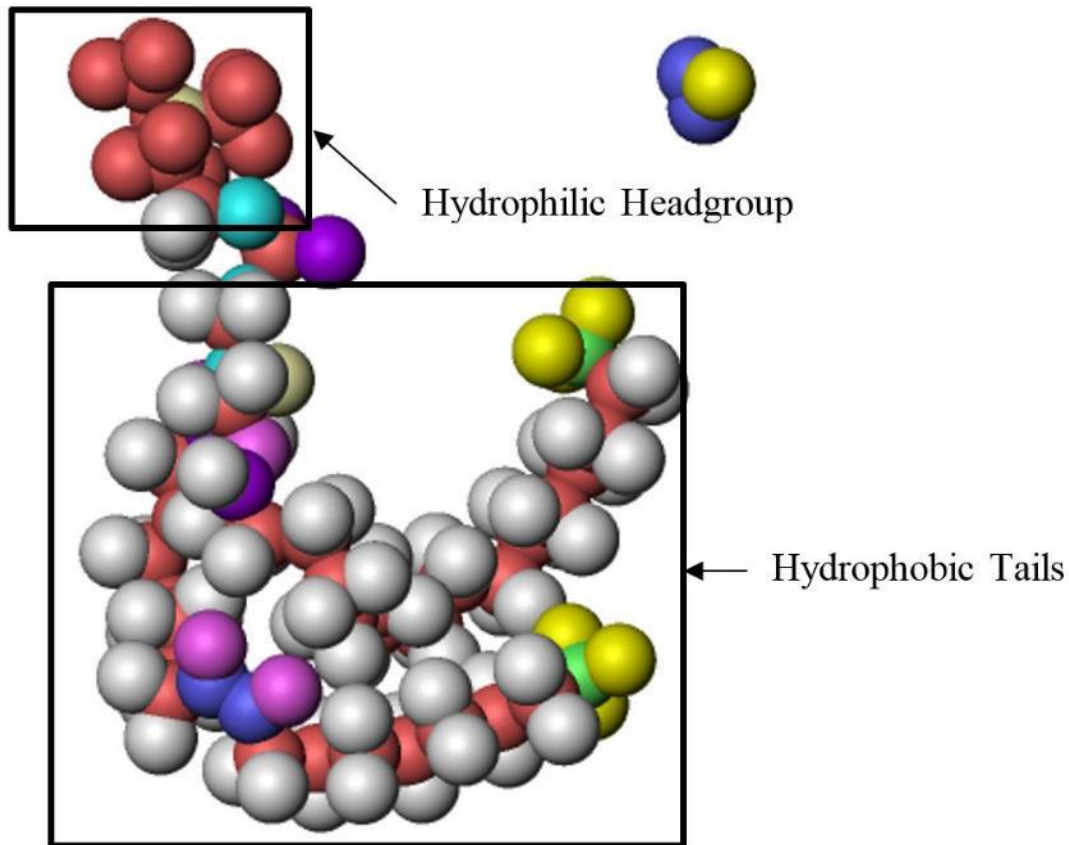


Figure 2.4 POPC molecule with hydrophobic and hydrophilic regions labeled.

## 2.2.6 Previous Simulations

### 2.2.6.1 Equilibration

The simulations of lipid bilayers have continually advanced to create larger systems with more accurate mechanics for longer time scales. For a time, the structures were limited to using a pseudo-isothermal-isobaric ensemble where the surface area is held constant (NPAT) or a constant surface area was implemented (NP $\gamma$ T) due to the phospholipid bilayer structures not maintaining the proper phase even during temperatures known to be above their phase transitions (Jeffery B. Klauda et al., 2010). The NPAT variation of the isothermal-isobaric (NPT) ensemble involved artificially

restricting the lipid bilayer dimensions in the in-plane directions to maintain the correct surface area (Jeffery B. Klauda et al., 2010). The NP $\gamma$ T achieved a similar goal by implementing negative pressures in the in-plane directions. This maintains a minimum surface tension on the structure and keeps it from condensing into the gel phase. Recent force fields, however, have corrections to fix this problem allowing for the use of full NPT simulations while still maintaining appropriate structure behavior (Jeffery B. Klauda et al., 2010).

#### **2.2.6.2 Deformations**

Despite experimental studies involving deformations of phospholipid bilayers, many properties of the lipid bilayer and their immediate physical results still require simulations due to the small time and length scales involved. These simulations can then be used to represent and interpret the physical phenomena that occur on the nanoscale and can give a more realistic understanding for why a particular influence results in a particular structural function or failure.

Several papers have previously examined deforming phospholipid bilayers and the formation of pores. Many of these deformed the bilayer under a state of tension based on the lateral in-plane pressures. Tieleman, Leontiadou, Mark, and Marrink (2003) varied the lateral plane pressure to deform the lipid bilayer. The applied lateral pressures resulted in pore formations at higher pressures and led to phospholipid bilayer destabilization. It was also noted that during the mechanical deformations the phospholipid bilayer thinned considerably in the perpendicular direction during deformations. Leontiadou, Mark, and Marrink (2004) used this method to display that pores were stable at low lateral pressures when the pore was inserted prior to simulations

and resulted in rupture at higher lateral pressures. However, controlling the deformations in this fashion is imprecise when considering the rate at which the bilayer is deformed which can affect the properties of the phospholipid bilayer. Additionally, controlling deformations using pressure can result in tearing the bilayer apart due to barostat feedback rather than pore formation (Tolpekina, den Otter, & Briels, 2004).

Alternatively, the phospholipid bilayer can be deformed under tension via changing the dimensions of the in-plane box dimensions and in effect allowing the phospholipids to adjust to the box. Tomasini, Rinaldi, and Tomassone (2010) used incremental tension to deform the bilayer equibiaxially in the lateral plane, but the deformations are performed with relaxation periods between each stretch. These increments do not represent a continuous deformation. Koshiyama and Wada (2011) performed simulations using equibiaxial tension using unsteady state stretching in the in-plane direction by using coordinate scaling. This provided a continuous deformation method to allow the lipid bilayer to form pores without allowing the structure to partially recover between changes in tension. Both Tomasini et al. (2010) and Koshiyama and Wada (2011) noted the rate dependence of the phospholipid bilayer structure.

Note that all of the above computational methods were used to deform the phospholipid bilayer structures only under equibiaxial conditions.

Studies on fluid shearing of the phospholipid bilayer have also been performed, but are much less common than studies involving tensile deformations of the phospholipid bilayer. By generating an uneven acceleration profile dependent on the  $z$  height of each individual atom, Tomasini et al. (2010) performed a simulation where shear was created between the bilayer leaflets.

*In silico* deformation studies have focused primarily on deformations using equibiaxial pressure or in-plane tension with little focus given to other stress states. In addition to further exploring the rate dependence of the phospholipid bilayer, the current study explores the effects of additional stress states and the phospholipid bilayer structure size on deformation results.

## **2.3 Molecular Mechanics Background**

### **2.3.1 Biological Materials**

It has long been standard practice to determine the mechanical properties and methods of failure for non-biological materials such as metals. More recently, however, a growing idea has been pushing for multiscale design. Two implementations of this idea are Biomateriomics which focuses on biological materiomes (Cranford & Buehler, 2012) and Integrated Computational Materials Engineering (ICME) which focuses primarily on bridging length scales in engineered materials (but is also being implemented in biological systems) (M. F. Horstemeyer, 2012). Although the implementation between these two is different, the general idea is the same: properties of lower length scales must be understood and implemented in higher length scales to gain a better understanding of materials and problems as a whole to get the best approximation to the answer.

Otherwise, only part the problem is considered and that means we don't get the best approximation to our problem which may result in more than acceptable error.

And excellent example is spider silk. It is extremely strong given the weight of the material despite being composed from components that are much weaker than many engineered materials (Bratzel & Buehler, 2012). Based on general material design, this fact does not make sense given many designs employ the idea that to make stronger

materials use stronger components. Therefore, determining the components of spider silk and how they are arranged to make it strong would allow for better materials to be designed (Cranford & Buehler, 2012). To do this, molecular dynamics must be utilized because molecular arrangements cannot be viewed or changed easily experimentally, but these changes are much easier to implement in simulations and can be run repeatedly to view the effects from minute changes. Similarly, molecular dynamics must be used to complement current macroscale models so that a better understanding can be obtained.

### 2.3.2 Virial Stress

Stress provides an excellent rubric for determining when elastic or plastic deformations will occur on the macroscale, with the simplest form being

$$\sigma = \frac{F}{A} \quad (2.1)$$

where  $\sigma$  is stress,  $F$  is force, and  $A$  is cross sectional area and can be easily determined using macroscale simulation methods. However, in molecular dynamics the volume, and in extension the area, of individual atoms are not well defined creating a need for an alternative definition of stress (M. F. Horstemeyer, 2012). Additionally, macroscale stress formulations make the assumption that the material in question is a continuum which also fails to hold true when considering molecular dynamics (Cranford & Buehler, 2012; M. F. Horstemeyer, 2012).

The virial form of stress has become common for atomic stress calculations. Rather than determining the stress for each individual atom, the virial stress takes an averaged value of all atoms in the specified volume which makes inappropriate to use the



virial stress as a point stress for individual atoms (Cranford & Buehler, 2012; M. F. Horstemeyer, 2012; Zimmerman et al.).

Unfortunately, however, there is yet to be an agreement for a best stress that translates to the Cauchy stress definition of the macroscale. There are even proposed variations for the definition of the virial stress. Zhou (2003) claimed that the virial equation was only comparable with Cauchy stress when including only the interatomic force term. However, others have indicated that this is incorrect and that the velocity force term must be included and that omitting the velocity term typically results in significant errors (Liu & Qiu, 2009; Zimmerman et al., 2004).

Alternatively, Liu and Qiu (2009) argued that a Lagrangian frame of reference is more appropriate and will always equal the Cauchy stress due to their definitions being the same, but Zimmerman et al. (2004) claimed that a Lagrangian definition must be done carefully and requires that other equations must be modified to do so because molecular dynamics simulations typically are performed in a Eulerian reference frame.

## **2.4 Traumatic Brain Injury**

Traumatic Brain Injury (TBI) is a condition that can potentially have permanent effects on the brain and affects 1.7 million people in the United States each year (Faul et al., 2010). As a general definition, “TBI is defined as an alteration in brain function, or other evidence of brain pathology, caused by an external force” (Menon, Schwab, Wright, & Maas, 2010). In other words, TBI is any acceleration or impact that affects brain function or pathology because these changes would indicate an injury, and likely neuron death to some degree, occurred. The death of neurons presents a prominent problem because they do not readily heal as most other cells of the body. Considering

the fact that cognitive functions are known to correlate to particular portions of the brain, damage to the brain can have many side effects including behavioral changes and lack of motor functions (Cummings, 1993). Therefore, injuries can be debilitating and long-lasting depending on the severity of the injury.

Many aspects of TBI have become more understood with the advent of better diagnostic imaging techniques, such as magnetic resonance imaging (MRI) and diffusion tensor imaging (DTI), which allow for *in vivo* observations (Kraus et al., 2007). However, these can only be used to view TBI post-injury and are limited both by resolution and the time it takes to administer and perform the imaging scan.

Other recent attempts to study traumatic brain injury have focused on trying to replicate the damaging effects of TBI experimentally. By performing tests on standardized lab animals, TBI can be observed and then documented along with the type and magnitude of the impact used. An example would be Cernak, Stoica, Byrnes, Giovanni, and Faden (2005) who used a fluid percussion head injury device to study TBI. However, experiments are limited by imaging techniques and the necessity of sacrificing the animals for cell staining.

Finite elements have been used to create models of the brain and models of parts of the brain (Cloots, Gervaise, van Dommelen, & Geers, 2008; Colgan, Gilchrist, & Curran, 2010; R. Prabhu, 2014). These studies implemented constitutive models to replicate the anisotropic material properties of the brain to obtain more accurate stress responses (Cloots et al., 2008; Colgan et al., 2010; R. Prabhu, 2014). However, biological materials often do not have a simple failure point because they are a combination of smaller dissimilar structures and can even self-repair in many cases. This

dissimilarity means that molecular dynamics is needed to determine the point of irreversible damage so that this information can be incorporated into constitutive material models being used for finite element models.

The current study investigates one aspect of TBI, mechanoporation, which potentially plays a large part in the resulting detrimental effects of TBI. The mechanical stimulus resulting in TBI causes mechanoporation which disrupts the membrane of the cell and allows it to become permeable to molecules that normally cannot pass through the membrane (Farkas & Povlishock, 2007). The temporary increase in permeability may increase the ability of excitotoxic ions, such as calcium, to enter the cell due to a diffusion gradient.

## **2.5 Multiscale Modeling**

### **2.5.1 Background**

In an ideal world, multiscale modeling would comprise of the ability to computationally perform the calculations for every variable on every length scale concurrently in a short period of time with little to no error. Unfortunately, this is currently far from reality due to current hardware and software limitations which restrict simulation speed, size, and accuracy. These restrictions necessitate that each length scale be handled separately for only a few chosen variables (M. F. Horstemeyer, 2012). To determine what variables need to be passed up, the information for higher scales must first be considered (M. F. Horstemeyer, 2012). Then the chosen variables can be solved for and passed up from lower length scale simulations (M. F. Horstemeyer, 2012). In other words, rather than running all simulations concurrently, the simulations are

performed sequentially for each needed length scale and parameters from each length scale are implemented into the next higher length scale level (M. F. Horstemeyer, 2012).

These limitations require that assumptions be made during the simulation setup leading to a model that is often highly simplified. Often, real world applications need answers regarding the macroscale. By treating the structure as a continuum and assigning material properties to the continuum media, the Finite Element Method (FEM) can often be used to provide approximations that are relatively close to the desired answer (M. F. Horstemeyer, 2012). However, due to the inherent requirement of the medium being continuous in the FEM, no information regarding the lower length scales are discernable from performing only Finite Element Analysis (FEA). Although more real-world material testing can be performed to create better material models to capture a better simulated macroscale material response, the model still cannot return information for length scales lower than the length scale being simulated.

Combined with the fact that many properties are difficult to measure experimentally because of time and length scales, the inability to determine sub-length scale mechanisms via FEA simulations creates problems when considering any complex material system where history effects and stress states affect the material behavior (M. F. Horstemeyer, 2012). This fact becomes increasingly true when one begins to consider materials of biological origin where many system changes cannot be viewed easily. Unlike metals which can often be imaged long after the test through a variety of methods without significant change, biological tissues often require a complex test apparatus for simple tests and must be fixed post experiment before staining and imaging. This makes it difficult to view mechanisms occurring during testing. In addition, testing the

macroscale properties alone is often insufficient for determining the relevant material properties and mechanisms (Cranford & Buehler, 2012; M. F. Horstemeyer, 2012). We will revisit the spider silk example from above. Bratzel and Buehler (2012) determined that there are molecular sequence-structure correlations related to the strength of the silk. Testing the silk on the macroscale would have never provided the information needed to make the sequence-structure correlation. The ideas behind multiscale modeling also extends into bioinspired design. Bosia, Buehler, and Pugno (2010) performed hierarchical multiscale simulations in an attempt to design high strength nanofibers based on the structure of spider silk.

### **2.5.2 Constitutive Equations**

As mentioned above, macroscale FEA simulations do not have the ability to return details for lower length scales. To obtain higher fidelity FEA models, an internal state variable (ISV) constitutive model must be implemented (M. F. Horstemeyer, 2012).

Although it is possible to obtain the values needed to build the ISV model through experimental methods, these experiments can be expensive and may fail to provide information relevant to the researcher due to only seeing the final specimen result (M. F. Horstemeyer, 2012). In some cases, it may be possible to stop mid experiment to perform imaging of a sample, but doing so is disruptive and may require the experiment to be restarted with a new specimen. Therefore, it is more economically suitable to perform lower length scale simulations because they can be repeated any number of times without problem, provide information for the entire experiment, allow for a wider set of parameter changes to be examined, and the original model can be reused indefinitely (Cranford & Buehler, 2012; M. F. Horstemeyer, 2012).

These internal state variables allow for the effects from phenomenon that are typically seen on lower length scales to be implemented in macroscale simulations (M. F. Horstemeyer, 2012). One potential lower length scale is the nanoscale which could be simulated using molecular dynamics. The exact formulations and relevant parameters will depend on the phenomenon being modeled, such as hardening or fatigue (M. Horstemeyer, Baskes, Prantil, Philliber, & Vonderheide, 2003; M. F. Horstemeyer, 2012).

### **2.5.3 Benefits**

Multiscale modeling bridges lower length scales details to higher length scales providing a variety of benefits such as access to information that higher length scales and experiments do not provide (Cranford & Buehler, 2012; M. F. Horstemeyer, 2012). A more accurate idea of lower length scale damage, introducing history effects, and how a material responds at different length scales are all benefits of multiscale modeling (Cranford & Buehler, 2012; M. F. Horstemeyer, 2012). These benefits are significant in creating a higher fidelity model. For example, when considering biological models, the lower length scale damage could be analogous to the effects of some injury, history affects would potentially affect the recoverability or higher susceptibility to repeated injury, and how the material responds at different length scales could represent anisotropic tissues which have macroscale properties that are very different from those of its constituents on lower length scales. In addition, performing simulations makes investigating the effects of defects, modifying material parameters, or other changes much simpler than creating entirely new models for every experiment (Cranford & Buehler, 2012; M. F. Horstemeyer, 2012).

Applying this to the current model of the phospholipid bilayer, investigating the disruptive mechanics at the nanoscale will provide a better idea of cell damage and may help to better predict when cells will die which could affect the brain as a whole. Additionally, history effects can be incorporated if some areas are known to be damaged (dead) and, therefore, behave differently.

#### **2.5.4 Error**

Error is introduced from length scale bridges, model boundary conditions, and experimental setup. The uncertainty resulting from these errors must be addressed when values are scaled up into a higher length scale model. For molecular dynamics, there are several sources of error. A large source of error is due to rounding and cutoffs because computers can only maintain so many digits and properties for the atoms are approximated using cutoffs to reduce computational cost (Leach, 2001). Additionally, numerical errors may be introduced if an algorithm is not implemented correctly (Leach, 2001). Another source of error is noise when calculating molecular properties because they vary greatly and must be averaged to obtain a meaningful value. Performing a running averaging also creates a source of error depending on the averaging interval chosen and the chosen averaging method (Leach, 2001). It should also be noted that smaller systems are more noisy, but due to computational costs the models cannot be enlarged without a considerable increase in cost.

#### **2.5.5 Verification**

Verification requires that the codes and algorithms used are consistent and being implemented correctly. This can be achieved by implementing the equations in a

different program/performing the calculations by some other means for comparison or running a previously published study for comparison (M. F. Horstemeyer, 2012).

Verification would require ensuring the equations are calculating the velocities and positions both consistently and according to the values from the force field parameters and the equations in LAMMPS. Verifying consistency is simple because it can be checked by running two jobs with the same input parameters because both jobs should return the same answer within numerical error. Verifying the equations are calculated properly is a bit more difficult, but one method is to verify the simulation results against others who have run the simulation before on a different system because they should be relatively similar.

#### **2.5.6 Validation**

Validation requires checking the model against experimental data to verify the results are consistent and fall within error expectations. This process is needed to ensure the equations have been implemented correctly in the program and that there are no strange computational issues giving incorrect results (M. F. Horstemeyer, 2012).

Validation would require comparing the values found using the simulations to experimental values and having them match within some degree of accuracy.



## CHAPTER III

### METHODS

#### 3.1 System Equilibration

A 1-palmitoyl-2-oleoylphosphatidylcholine (POPC) lipid bilayer structure was used as a representative structure for a cell membrane. Atomic coordinates for a pre-equilibrated lipid bilayer were obtained from the website of the Laboratory of Computational Biology: Membrane Biophysics Section ("Laboratory of Computational Biology, National Heart, Lung, and Blood Institute, National Institutes of Health, Bethesda, MD 20892," n.d.) based on the paper by Jeffery B. Klauda et al. (2010). The phospholipid bilayer structure contained seventy-two phospholipids and two thousand two hundred forty-two TIP3P water molecules. The molecular dynamics simulator LAMMPS (Large-scale Atomic/Molecular Massively Parallel Simulator, <http://lammms.sandia.gov>) (Plimpton, 1995) paired with the CHARMM36 all-atom lipid (Chemistry at HARvard Molecular Mechanics) (Jeffrey B. Klauda, n.d.; Jeffrey B. Klauda et al., 2010) force field was used for all simulations. The force field parameters for the CHARMM force field can be seen in Appendix A.

Blocks of water containing one thousand one hundred thirty-eight water molecules were created using the water present in the lower half of the original phospholipid bilayer structure. Three blocks of water were then added to the top and bottom of the bilayer structure to limit interactions between the periodic images during

deformations. This addition resulted in a total of nine thousand and seventy water molecules.

The temperature for the structure was chosen to be 310 K to replicate the natural human body temperature. The simulation temperature was ramped to three hundred and ten kelvin using the NVT (canonical) ensemble. Then, the NPT (isothermal-isobaric) ensemble was used to allow the simulation box to equilibrate anisotropically under a pressure of one atm in all principal dimensions resulting in a total of five nanoseconds of equilibration. All simulations were performed utilizing periodic boundary conditions (PBCs), a half femtosecond time step, and a particle-particle particle-mesh (PPPM) solver grid of  $1 \times 10^{-5}$  with analytical differentiation.

The structure was then replicated by a factor of two in the x dimension to create a lipid bilayer structure that had dimensions of approximately ten by five nanometers. Both structures were then equilibrated for an additional five nanoseconds. A summary of properties for both structures with true sizes can be seen in Table 3.1. A size comparison of lipid bilayer structures can be seen in Figure 3.1.

Table 3.1 Summary of Atom and Molecule Count with Corresponding Sizes in Nanometers for Each Structure

<b>Approximate Bilayer Size</b>	<b>Atoms</b>	<b>Lipids</b>	<b>Area per Lipid</b>	<b>Water Molecules</b>	<b>x length</b>	<b>y length</b>	<b>z length</b>
5x5	36858	72	0.63	9070	4.88978	4.61298	13.78242
10x5	73716	144	0.60	18140	9.32324	4.65756	14.28650

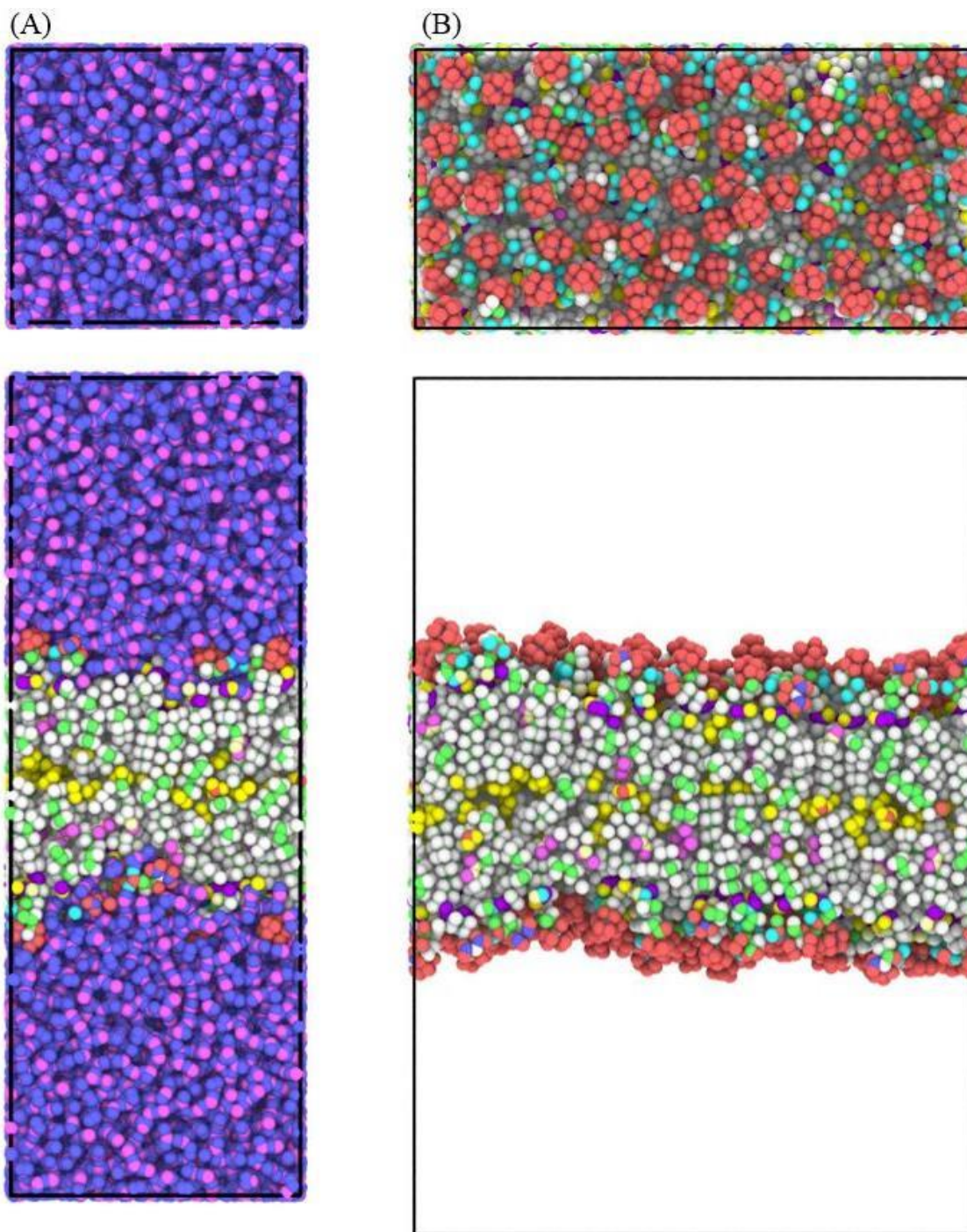


Figure 3.1 Size comparisons of the equilibrated lipid bilayer structures

Notes: (A) 72 phospholipid structure with water displayed (B) 144 phospholipid structure with water hidden

### 3.2 Deformation Simulations

Each structure was subjected to constant velocity deformations in the x and y dimensions as seen in Table 3.2 to examine the strain rate ( $1.7e8$ ,  $5.0e8$ , and  $6.7e8$  /sec), phospholipid bilayer size (72 and 144 phospholipids), and stress state dependence (strip biaxial, equibiaxial (strain rate based), non-equibiaxial, and uniaxial tension).

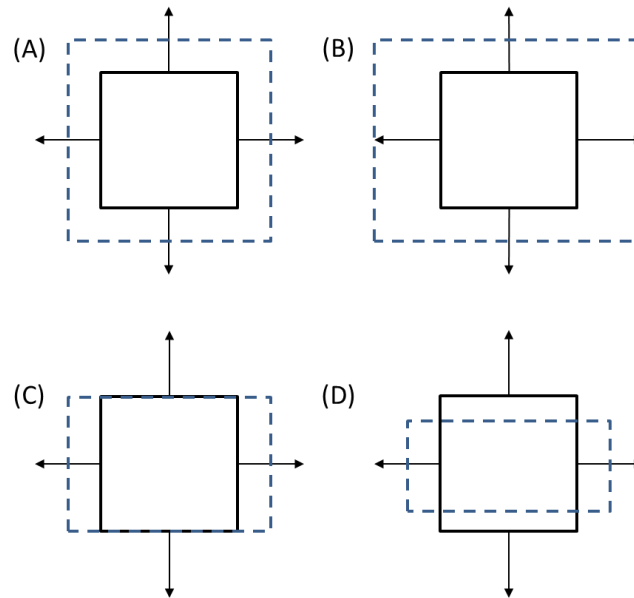


Figure 3.2 Representative perpendicular (top) view of the deformations performed where the initial structure is represented by a solid black line and the deformed structure by a lighter dashed line

Notes: (A) Equibiaxial Tension, (B) Non-Equibiaxial Tension, (C) Strip Biaxial Tension, and (D) Uniaxial Tension

Deformation velocities for the different stress states and larger phospholipid bilayer under strip biaxial tension were determined using von Mises strain rates and correspond to the  $72 \times 4 \times 0$  case. The z dimension was allowed to adjust freely while being subjected to a pressure of one atm for all cases. The y dimension was allowed to adjust

freely in the case of uniaxial deformations. All other parameters remained the same as during the equilibration simulations.

Table 3.2 Summary of Deformation Simulations

<b>Case Name</b>	<b>Number of Lipids</b>	<b>von Mises Strain Rate (1/sec)</b>	<b>~Deformation Rate x (m/s)</b>	<b>~Deformation Rate y (m/s)</b>
72x1y0	72	1.7e8	1.0	0
72x3y0	72	5.0e8	3.0	0
72x4y0	72	6.7e8	4.0	0
144x7.6y0	144	6.7e8	7.6	0
72x2.8y2.7	72	6.7e8	2.8	2.7
72x3.6y1.7	72	6.7e8	3.6	1.7
72x4yR	72	6.7e8	4.0	Relax

The structure was visualized using the program OVITO. Various methods of visualization in OVITO were utilized to monitor pore formation and determine when failure occurred. The primary visualizations performed involved 1. Hiding all water molecules with the phospholipids visible so that pores could be visually monitored and 2. Hiding all phospholipids with water visible to determine when a water bridge had formed. The phospholipid bilayer was considered to have failed when water fully penetrated through both the top and bottom phospholipid leaflet and connected forming a water bridge through both leaflets.

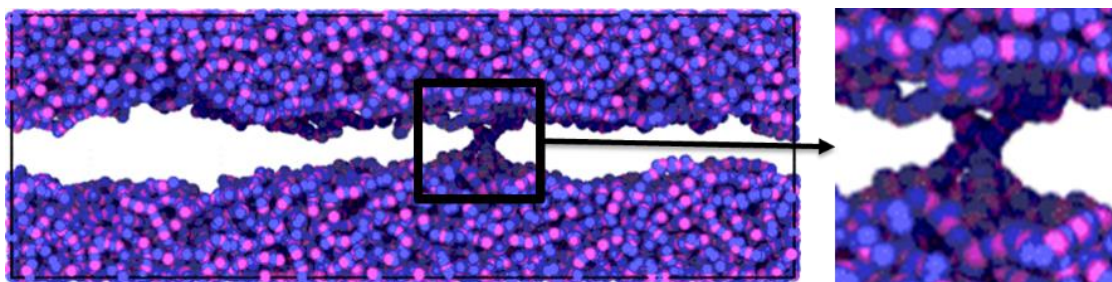


Figure 3.3 Side view of the phospholipid bilayer with all lipids hidden for the 72x1y0 case

Notes: The water bridge had just connected and is enlarged on the right.

### 3.3 Analysis

#### 3.3.1 Image Analysis

OVITO (Stukowski, 2010) was used to render images every 50 ps. The OpenGL renderer with an antialiasing value of 6 was used for images used in analysis. All waters were hidden, phospholipid atoms were colored black, and the images had a white background. Additionally, the box lines were allowed to remain visible creating a definitive boundary for the structure. These were imported into the image analysis software ImageJ (Rasband, 1997-2014; Schneider, Rasband, & Eliceiri, 2012) as a virtual stack. Black and white thresholding was performed with values of 200 and 255 and the “Dark background” option was selected making the phospholipids white and the pores black. The scale was set using the box size and visible box lines. Additionally, the following options were selected under “Set Measurements”: Area, Area fraction, Mean gray value, Centroid, and Stack position. “Analyze Particles” was utilized to generate the following results for all pores and then for pores only greater than  $.1 \text{ nm}^2$  in size: pore number, pore area, centroid coordinates, and pore slice which corresponded to the time at which the pore occurred.

These values were saved and read into a custom written MATLAB script which calculated the following for each slice: total pore area ( $nm^2$ ), the number of pores, the pore density ( $Pores/nm^2$ ), area fraction, mean pore area ( $nm^2$ ), and mean nearest neighbor distance (nm). All pores reported by ImageJ were treated as unique and did not account for periodic boundary conditions leading to potentially higher pore counts than actually seen.

OVITO was also used for rendering images for creating figures. The Tachyon renderer was utilized to create higher quality images for publishing. The following settings were used when creating images with the Tachyon renderer: anti-aliasing of 50, ambient occlusion brightness of .9 and sample count of 12, and shadows were included.

### **3.3.2 Quantitative Analysis**

Values of interest, such as: temperature, total energy, potential energy, kinetic energy, pressure, van der Waals energy, coulomb energy, bond energy, angle energy, dihedral energy, improper energy, long range kspace energy, volume, max force, normal force, were output every five femtoseconds. These were monitored to determine if the structures were equilibrated. Additionally, the pressure tensor and the box height perpendicular to the phospholipid bilayer were output every five femtoseconds during deformations.

#### **3.3.2.1 Surface Tension**

The equation for surface tension as discussed in Zhang, Feller, Brooks, and Pastor (1995) is:

$$\gamma = \left( P_z - \frac{P_x + P_y}{2} \right) * L_z \quad (3.1)$$

Where  $\gamma$  is surface tension,  $P_x$ ,  $P_y$ , and  $P_z$  are the principle stresses (principle system pressures on the respective faces), and  $L_z$  is the box height. Another form exists where a factor of one half is introduced for systems with two interfaces, such as phospholipid bilayers, however, the form omitting this factor is used to maintain consistency with published literature (Koshiyama & Wada, 2011; Leontiadou et al., 2004; Tomasini et al., 2010).

Additionally, it is noted that only the region near the interface affects the surface tension, therefore an assumption of a small layer of water is required (Koshiyama & Wada, 2011; Zhang et al., 1995). This is problematic due to the need of a large water layer to prevent periodic images from interacting as the bilayer is deformed. Therefore, the bilayer height is assumed to decrease linearly from an initial approximate height of sixty angstroms (which allows a small water layer) to the minimum recorded height of the box because the box height and bilayer height are approximately equal at the end of deformations. A representative comparison of the heights can be seen in Figure 3.4. The uniaxial case was treated differently due to the box and bilayer not relaxing as much in the z dimension. In fact, the z height does not fall below the initial bilayer height as seen in all other cases. Therefore, the assumption that the box and bilayer size become increasingly the same as the simulation progressed was incorrect. To correct this, the actual bilayer height was viewed and set to forty-five angstroms instead of the minimum box height.



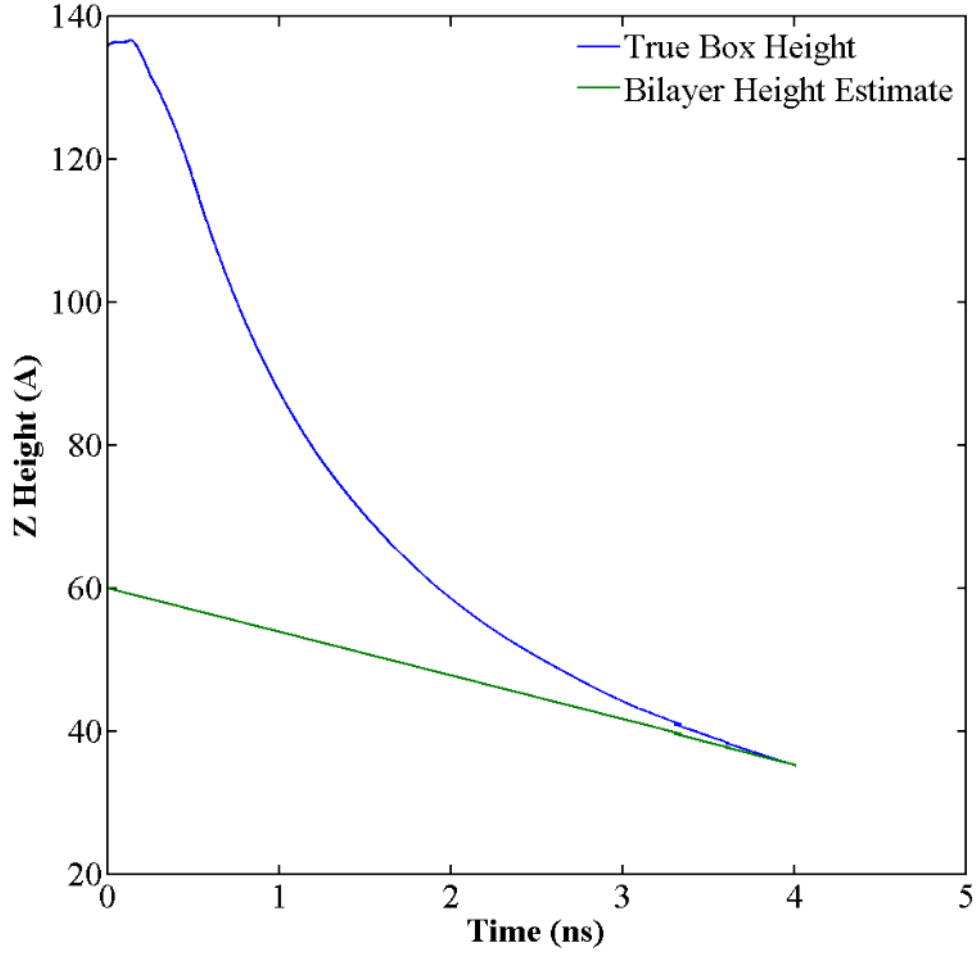


Figure 3.4 Comparison of true box height and a linear estimate of phospholipid bilayer height.

Notes: True box height taken from the the seventy-two phospholipid bilayer deformed under strip biaxial tension at a Von Mises strain rate of  $6.7e8/\text{sec}$ .

### 3.3.2.2 Von Mises Stress and Strain

The equivalent von Mises stress and strain were also utilized for quantifying deformations. The shear stresses were significantly smaller than the principle stresses and did not change with deformations, so they were omitted, resulting in:

$$\sigma_{VM} = \sqrt{\frac{1}{2}[(\sigma_1 - \sigma_2)^2 + (\sigma_2 - \sigma_3)^2 + (\sigma_1 - \sigma_3)^2]} \quad (2.2)$$

where  $\sigma_{VM}$  is the equivalent von Mises stress and  $\sigma_1, \sigma_2, \text{ and } \sigma_3$  are the principle stresses.

Additionally, the box remained orthogonal, therefore, no shear strains occurred allowing for the use of the following equivalent von Mises strain equation:

$$\epsilon_{VM} = \frac{2}{3} * \sqrt{\frac{3}{2} * (\epsilon_1^2 + \epsilon_2^2 + \epsilon_3^2)} \quad (3.3)$$

where  $\epsilon_{VM}$  is the equivalent von Mises stress and  $\epsilon_1, \epsilon_2, \text{ and } \epsilon_3$  are the principle strains.

To obtain equivalent von Mises strain rates between different stress states, any dimensions allowed to relax are assumed to be zero. In other words, only dimensions strained by controlled deformations were included in von Mises strain calculations.

### 3.3.2.3 Calculation of Elastic Properties

For the uniaxial case,  $\sigma_1$  was plotted against  $\epsilon_{11True}$  to determine the elastic modulus. The modulus was taken to be the slope of a trend line plotted against the initial linear portion of the stress-strain curve.

Poisson's ratio was determined for this region as well. These were used to calculate the bulk and shear modulus.

The area compressibility modulus was similarly measured using the surface tension vs true strain curve. This was compared to the results of the bulk modulus via the equation:

$$K_a = K_b * L_{bilayer} \quad (3.4)$$

where  $K_a$  is the area compressibility modulus,  $K_b$  is the bulk modulus, and  $L_{bilayer}$  is the bilayer height.

## CHAPTER IV

### RESULTS

#### 4.1 Strain Rate Comparison

0 shows that the pores develop differently between the three cases. Starting from the same initial configuration, it is apparent that at a von Mises strain of .57, the phospholipid headgroups of the structure were already being pulled away from one another into smaller groups which left areas where the hydrocarbon tails were more exposed to water. At full water penetration, for which the strains of each case can be seen in 0, it was apparent that the initial pore formations were not appearing in the same location. At a von Mises strain of 1.3, it is apparent that the higher strain rates appear to form multiple smaller pores capable of forming water tunnels instead of the pores seen at lower rates which were fewer in number but larger.











Von Mises Strain Rate (1/sec)	1.7e8	5.0e8	6.7e8
Initial Structure			
Von Mises Strain of 0.57			
Full Water Penetration			
Von Mises Strain of 1.13			

Figure 4.1 Pore formation during phospholipid bilayer deformations are shown for strip biaxial tension at von Mises equivalent strain rates of 1.7e8, 5.0e8, and 6.7e8 /s.

The first peak stress for each von Mises strain rate can be seen in Table 4.1 along with the strains corresponding to points of interest.

Table 4.1 Mechanical Properties of the Seventy-Two Phospholipid Bilayer Under Strip Biaxial Tension at Different von Mises Strain Rates

Strain Rate <sup>VM</sup> (1/sec)	$\sigma_{FirstPeak}^{VM}$ (MPa)	$\epsilon_{FirstPeak}^{VM}$	$\epsilon_{FirstPore}^{VM}$	$\epsilon_{Failure}^{VM}$
1.7e8	26.6	0.071	0.097	0.884
5.0e8	49.0	0.220	0.155	0.861
6.7e8	61.1	0.224	0.127	0.919

Figure 4.2 shows that all of the simulations displayed an initial jump in surface tension when the box was initially deformed. They then decrease until they temporarily plateau, more apparent in the lower rates, before water penetration occurs.

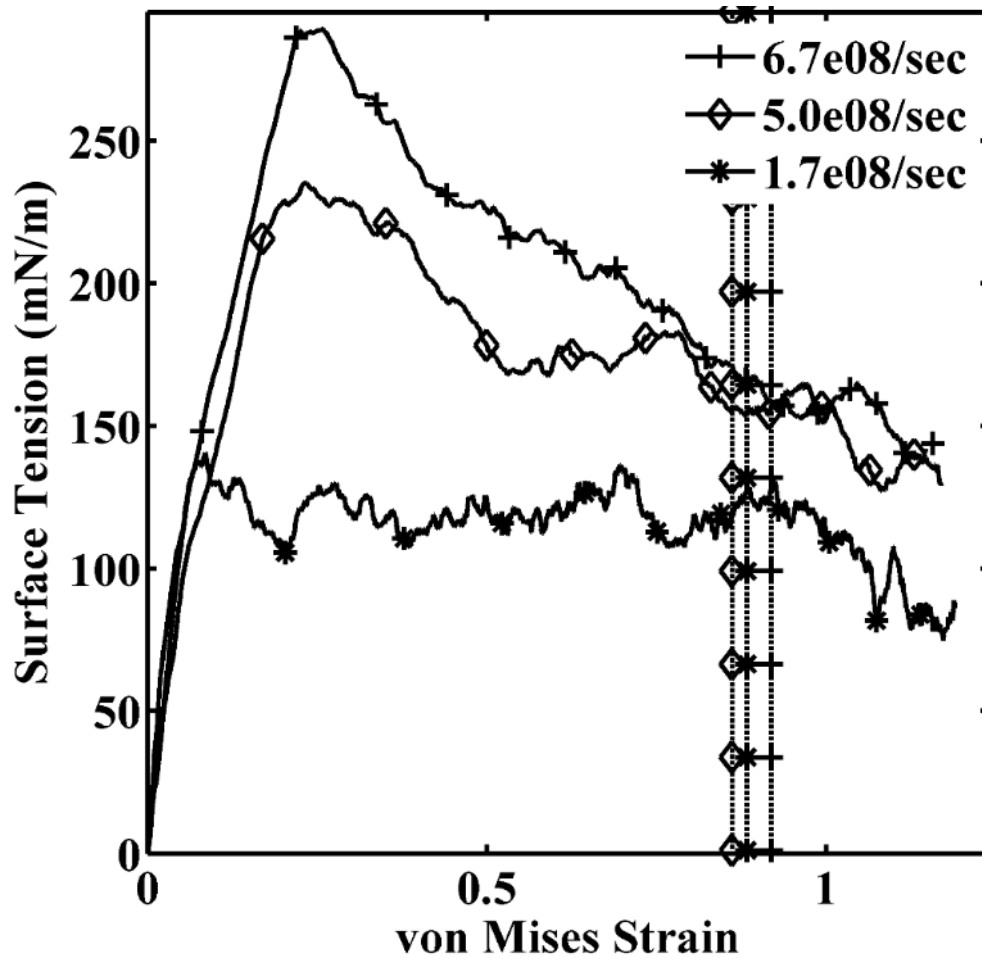


Figure 4.2 Surface tension-von Mises strain curve displaying the effect of the von Mises strain rate.

Notes: (von Mises strain rate = 6.7e8, 5.0e8, and 1.7e8 /sec)  
 Simulations performed on the seventy-two phospholipid bilayer when subjected to strip biaxial tension deformations. Vertical dash lines with markers matching their corresponding curve display when full water penetration occurs.

The von Mises stress-strain trend is very similar to that of the surface tension. The fluctuations are more pronounced and the von Mises stress-strain curve results in lower initial peak values and higher final values (relative to mid-curve) due to a lack of effect from the bilayer height.

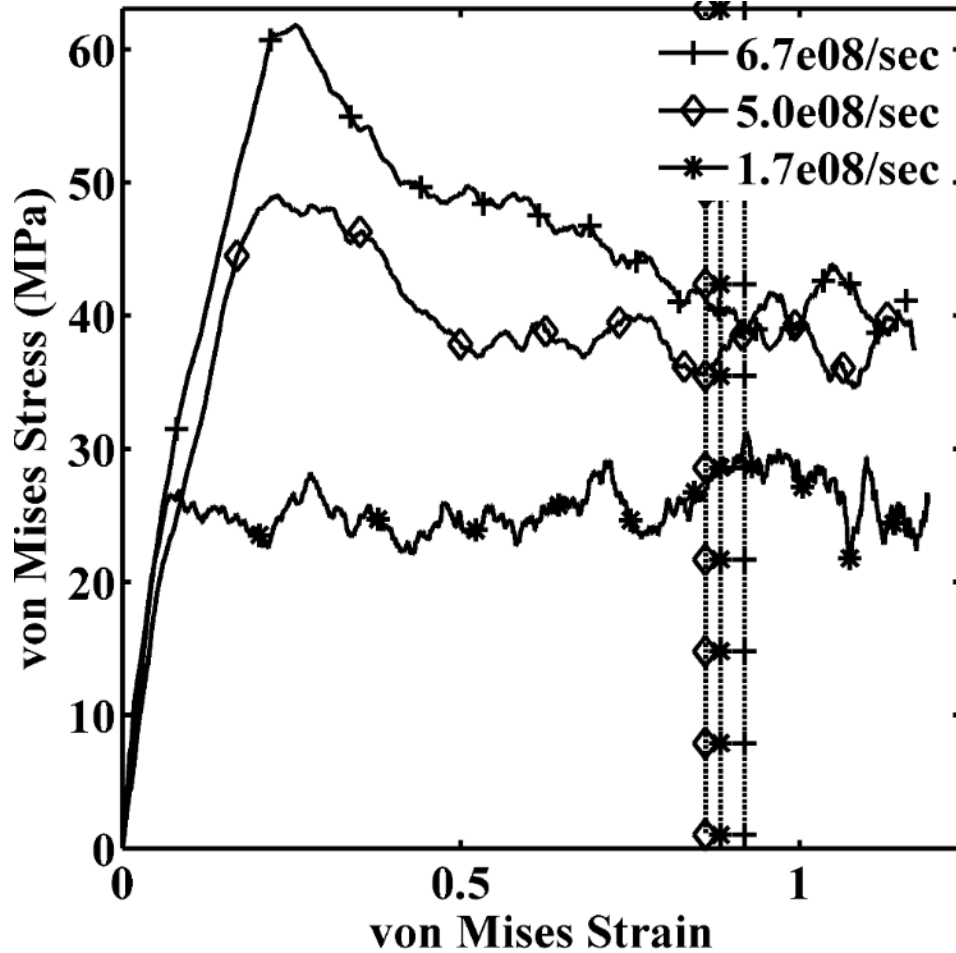


Figure 4.3 Von Mises stress-strain curve displaying the effect of the von Mises strain rate.

Notes: (von Mises strain rate =  $6.7e8$ ,  $5.0e8$ , and  $1.7e8$  /sec)  
 Simulations performed on the seventy-two phospholipid bilayer when subjected to strip biaxial tension deformations. Vertical dash lines with markers matching their corresponding curve display when full water penetration occurs.

In both Figure 4.2 and Figure 4.3, the von Mises strain rate increases resulted in increased peak stress values.

The image analysis results for the strip biaxial strain rate comparison can be seen in the following figures. Each figure has values for curves for all pores and for only pores  $> .1 \text{ nm}^2$ . Colored vertical dash lines correspond to water penetration for each strain rate. Figure 4.4 displays the progression of pore formation, Figure 4.5 displays the area density, Figure 4.6 displays the total pore area, Figure 4.7 displays the mean pore area, Figure 4.8 displays the area fraction, and Figure 4.9 displays the mean neighbor distance.

It is apparent that initially there are no pores present in the bilayer structure. After the pores begin appearing, they continue to increase along with the total pore area, mean pore area, area fraction, and area density. The number of smaller pores is much greater than those greater than  $.1 \text{ nm}^2$ . However, in Figure 4.6, it is apparent that the larger pores make up the majority of the pore area when they begin forming. Conversely, the mean NND trend was the same as when all pores were considered in that it decreased as the pore count increased, but it began much later due to needing multiple large pores. Interestingly, the point of complete water penetration seems to at or shortly after the point when multiple pores began appearing consistently.

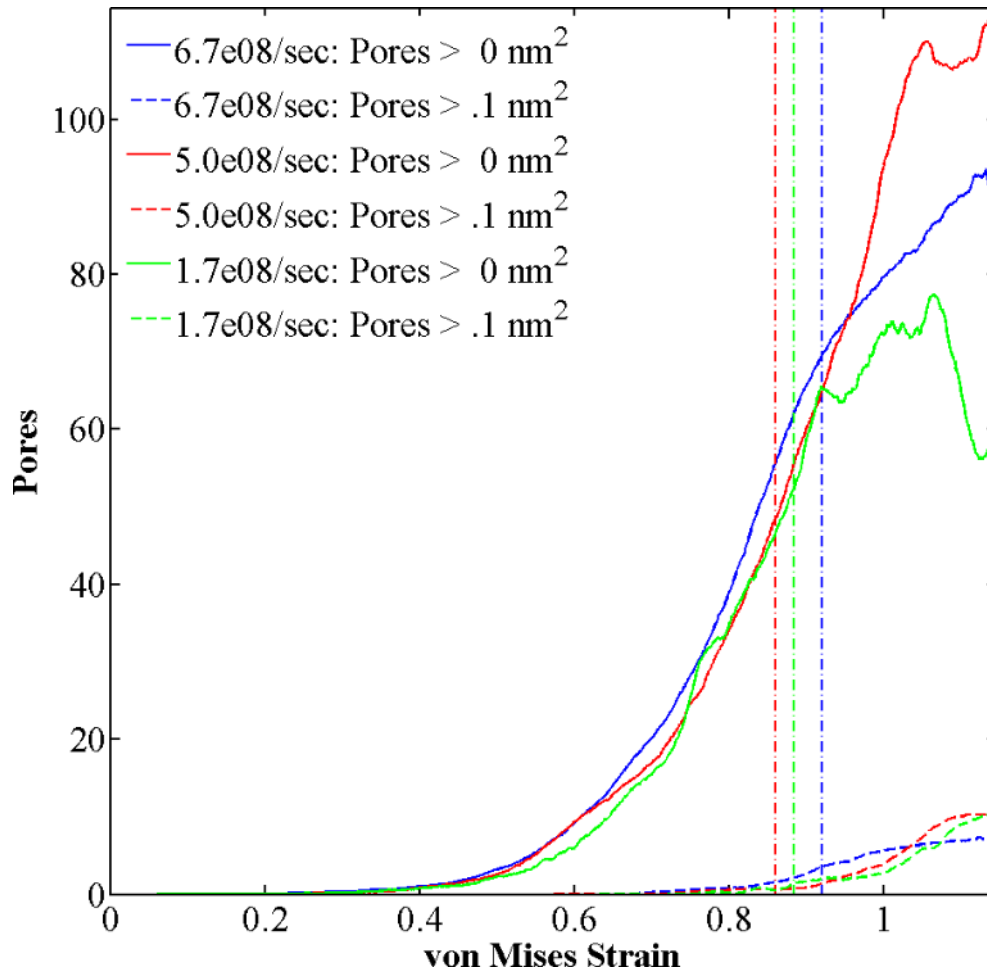


Figure 4.4 Pore count for different von Mises strain rates.

Notes: (=6.7e8, 5.0e8, and 1.7e8 /sec)

Simulations performed on the seventy-two phospholipid bilayer when subjected to strip biaxial tension deformations. Vertical dash lines color matched to their corresponding curve display when full water penetration occurs.



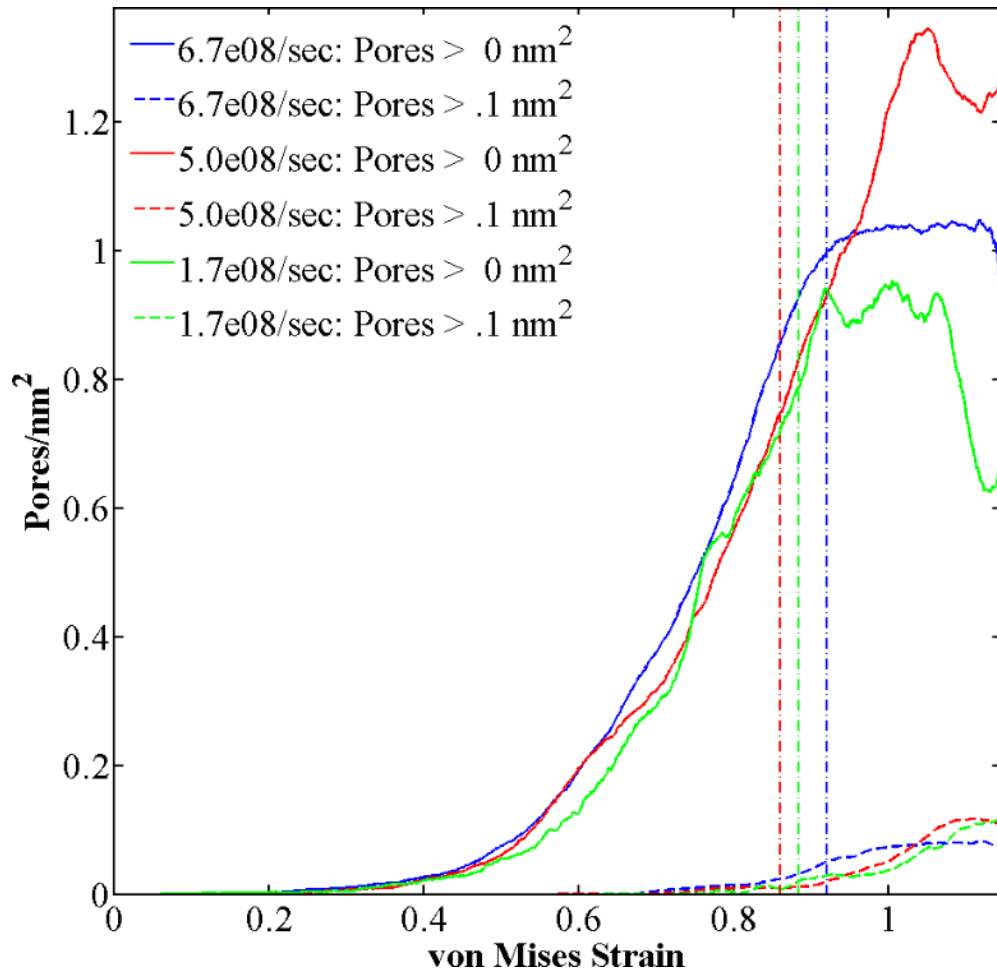


Figure 4.5 Area density for different von Mises strain rates.

Notes: (=6.7e8, 5.0e8, and 1.7e8 /sec)

Simulations performed on the seventy-two phospholipid bilayer when subjected to strip biaxial tension deformations. Vertical dash lines color matched to their corresponding curve display when full water penetration occurs.

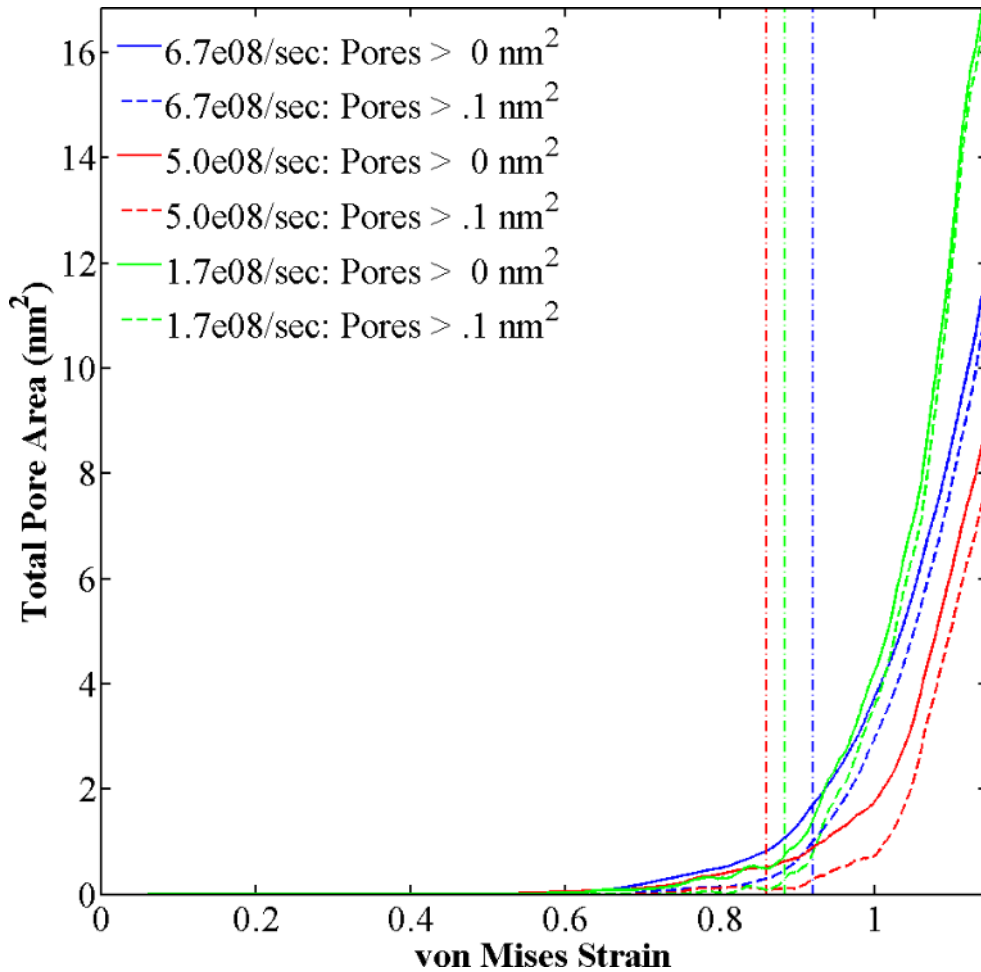


Figure 4.6 Total pore area for different von Mises strain rates

Notes: (=6.7e8, 5.0e8, and 1.7e8 /sec).

Simulations performed on the seventy-two phospholipid bilayer when subjected to strip biaxial tension deformations. Vertical dash lines color matched to their corresponding curve display when full water penetration occurs.

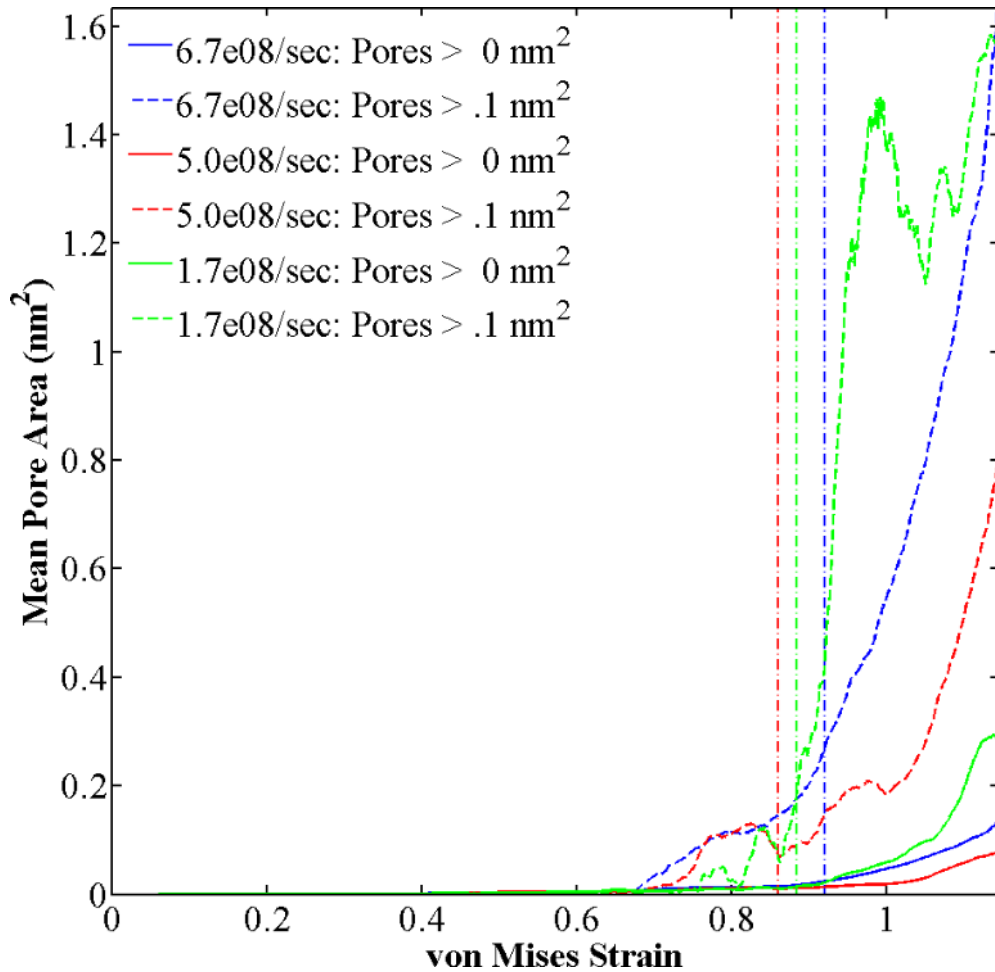


Figure 4.7 Mean pore area for different von Mises strain rates.

Notes: (=6.7e8, 5.0e8, and 1.7e8 /sec)

Simulations performed on the seventy-two phospholipid bilayer when subjected to strip biaxial tension deformations. Vertical dash lines color matched to their corresponding curve display when full water penetration occurs.

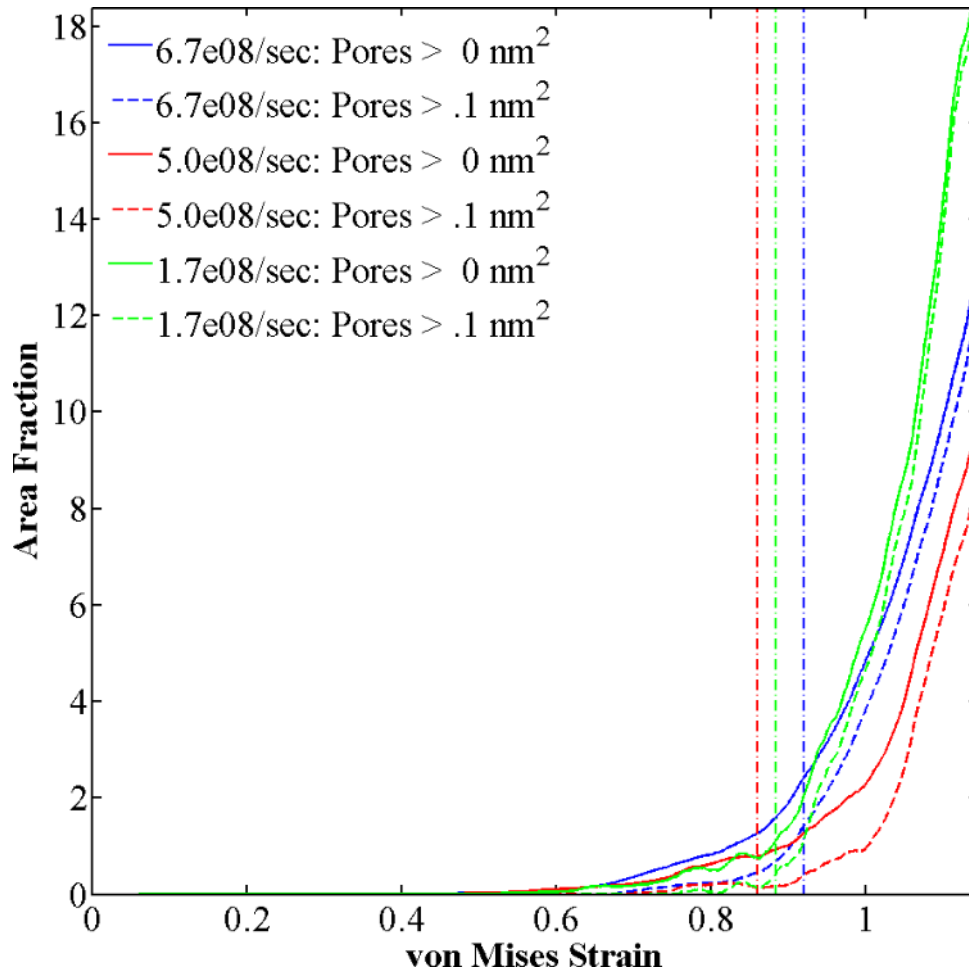


Figure 4.8 Area fraction for different von Mises strain rates.

Notes: (=6.7e8, 5.0e8, and 1.7e8 /sec)

Simulations performed on the seventy-two phospholipid bilayer when subjected to strip biaxial tension deformations. Vertical dash lines color matched to their corresponding curve display when full water penetration occurs.

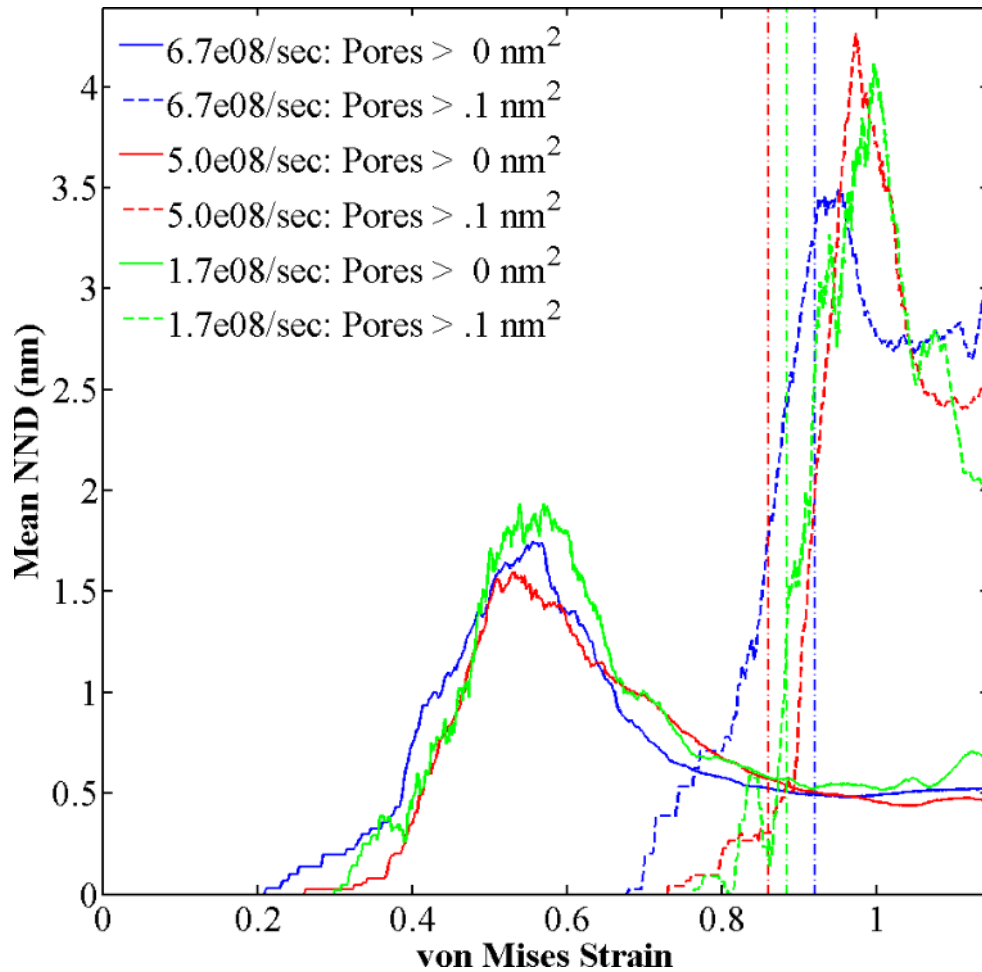


Figure 4.9 Mean nearest neighbor distance for different von Mises strain rates.

Notes: (=6.7e8, 5.0e8, and 1.7e8 /sec)

Simulations performed on the seventy-two phospholipid bilayer when subjected to strip biaxial tension deformations. Vertical dash lines color matched to their corresponding curve display when full water penetration occurs.

It is apparent in Figure 4.10 that the stress at the first peak is linearly proportional to the strain rate in the von Mises strain rates tested.

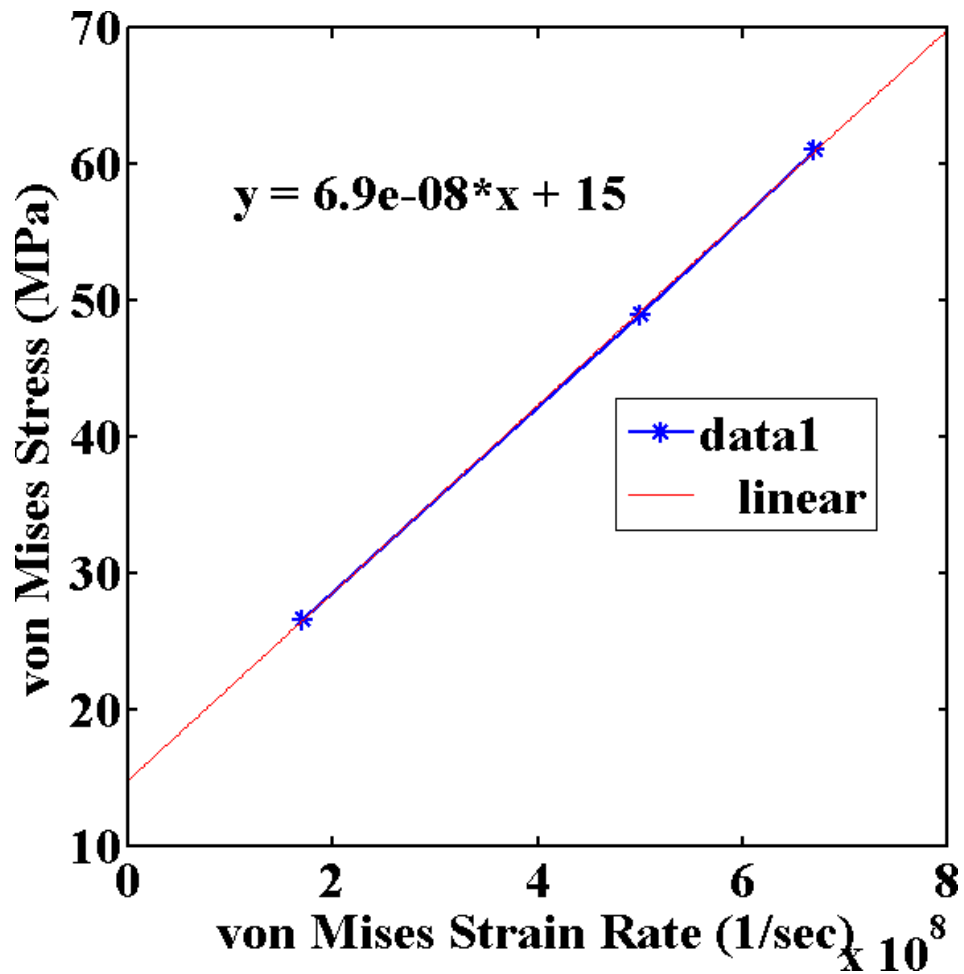


Figure 4.10 Correlation of von Mises Strain Rate and the von Mises Stress at the first peak results in a linear trend.

## 4.2 Phospholipid Bilayer Size Comparison

The first peak stress for each von Mises strain rate can be seen in Table 4.2 along with the strains corresponding to points of interest.

Table 4.2 Mechanical Properties of the Phospholipid Bilayer Under Strip Biaxial Tension at a von Mises Strain Rate of 6.7e8 /sec for Different Sizes

Number of Lipids	$\sigma_{FirstPeak}^{VM}$ (MPa)	$\epsilon_{FirstPeak}^{VM}$	$\epsilon_{FirstPore}^{VM}$	$\epsilon_{Failure}^{VM}$
72	61.1	0.224	0.127	0.919
144	60.3	0.233	0.315	0.911

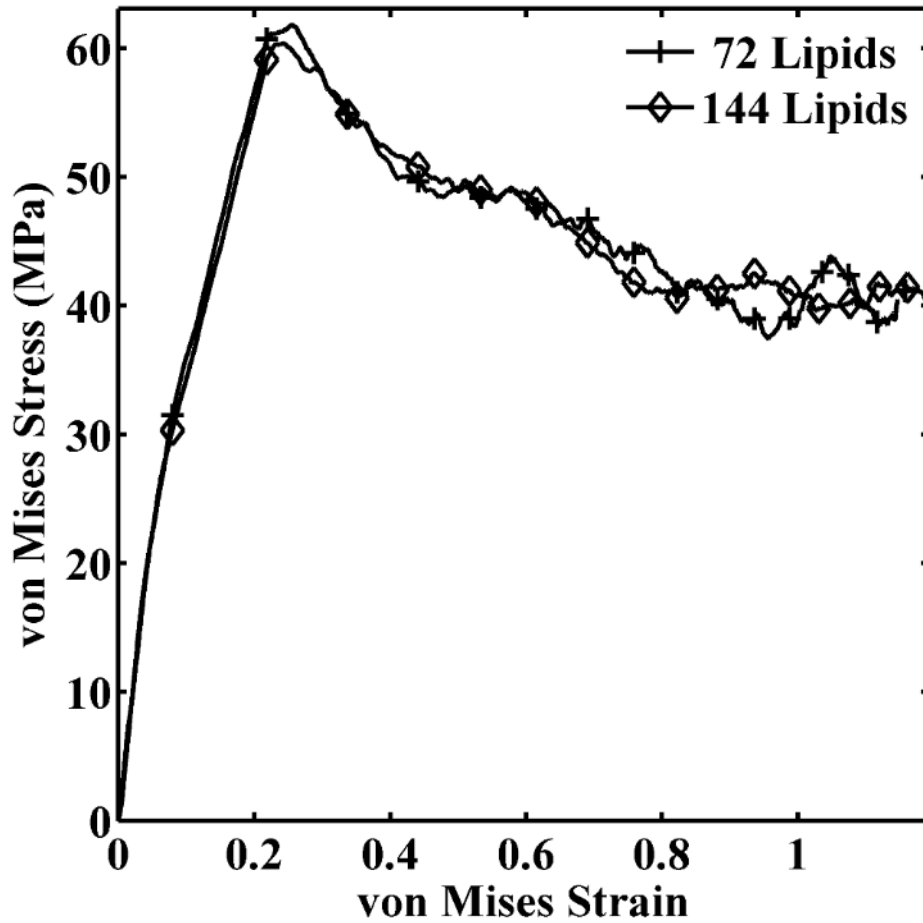


Figure 4.11 Von Mises stress-strain curve displaying the effect of phospholipid bilayer size.

Notes: (seventy-two and one hundred forty-four phospholipids)  
 Both simulation models subjected to strip biaxial tension deformations at the von Mises strain rate of 6.7e8 /sec.

The image analysis results for the strip biaxial phospholipid bilayer size comparison can be seen in the following figures. Each figure has values for curves for all

pores and for only pores  $> .1 \text{ nm}^2$ . Colored vertical dash lines correspond to water penetration for each strain rate. Figure 4.12 displays the progression of pore formation, Figure 4.13 displays the area density, Figure 4.14 displays the total pore area, Figure 4.15 displays the mean pore area, Figure 4.16 displays the area fraction, and Figure 4.17 displays the mean neighbor distance.

Although there was no difference in the resulting stresses, the image analysis data indicates there may be considerable differences. The seventy-two phospholipid structure begins producing pores much earlier and greatly exceeds the small pore count of than the larger structure. However, the larger structure exceeds the total pore area indicating that even though it has fewer pores, they pores are larger than those in the smaller bilayer.



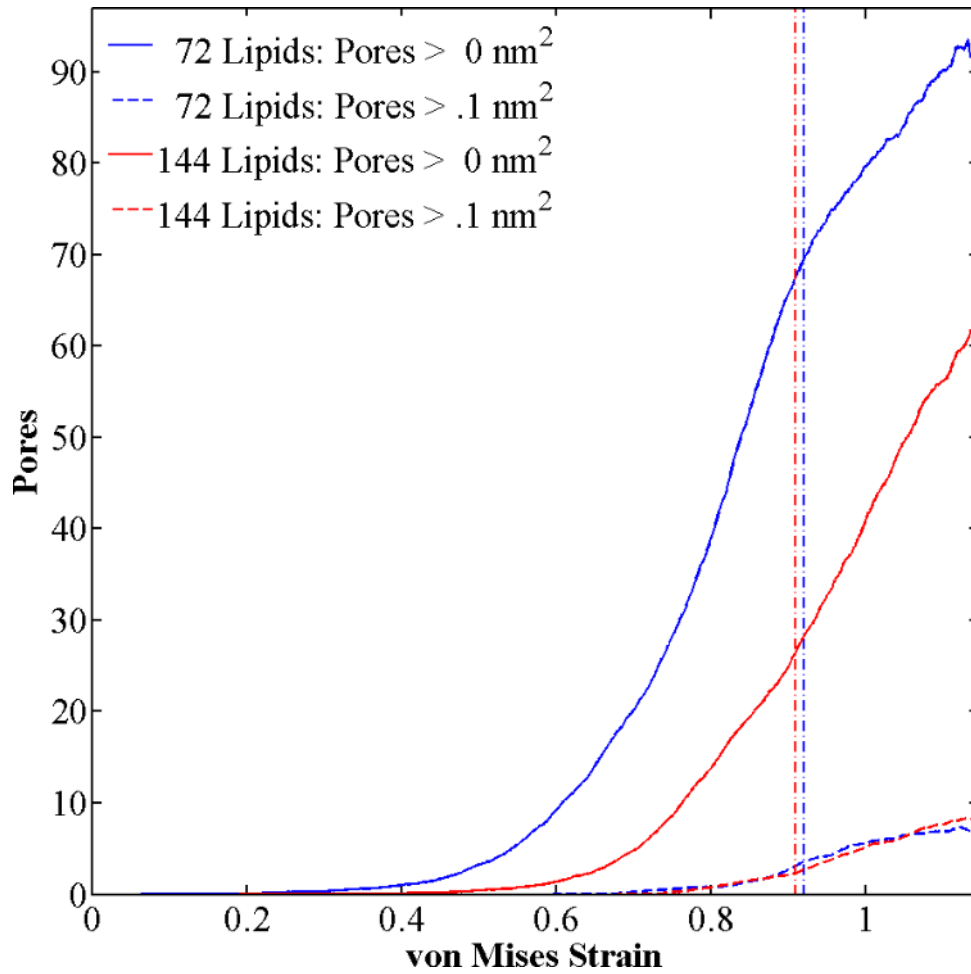


Figure 4.12 Pore count for different phospholipid bilayer size.

Notes: (seventy-two and one hundred forty-four phospholipids)

Both simulation models subjected to strip biaxial tension deformations at the von Mises strain rate of  $6.7e8$  /sec. Vertical dash lines color matched to their corresponding curve display when full water penetration occurs.

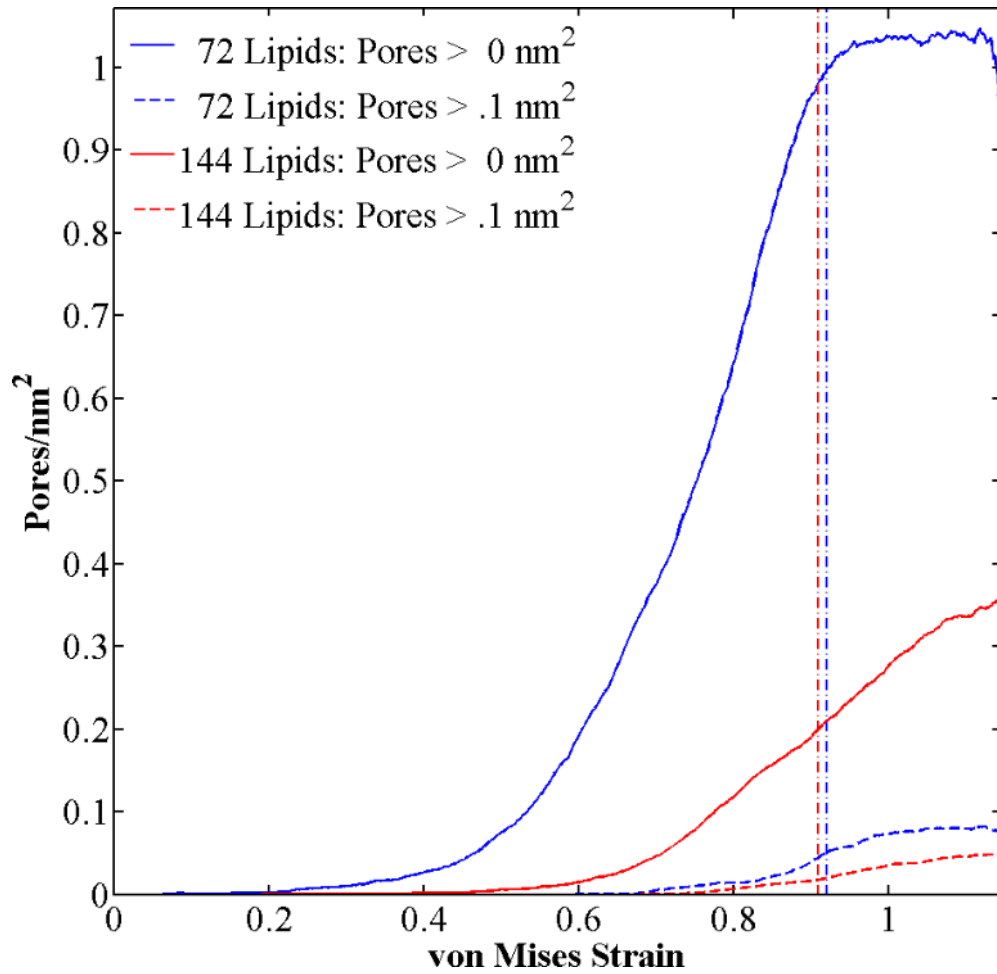


Figure 4.13 Area density for different phospholipid bilayer size.

Notes: (seventy-two and one hundred forty-four phospholipids)

Both simulation models subjected to strip biaxial tension deformations at the von Mises strain rate of  $6.7e8$  /sec. Vertical dash lines color matched to their corresponding curve display when full water penetration occurs.

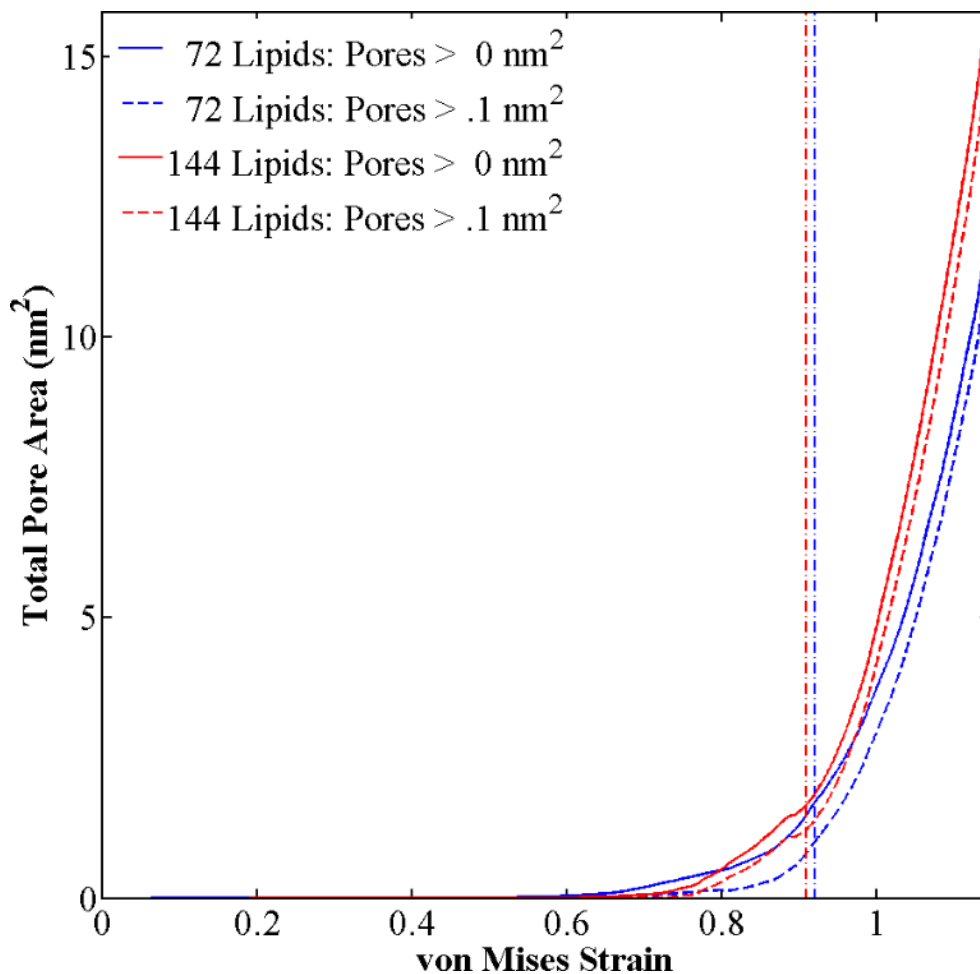


Figure 4.14 Total pore area for different phospholipid bilayer size.

Notes: (seventy-two and one hundred forty-four phospholipids)

Both simulation models subjected to strip biaxial tension deformations at the von Mises strain rate of  $6.7 \times 10^8$  /sec. Vertical dash lines color matched to their corresponding curve display when full water penetration occurs.

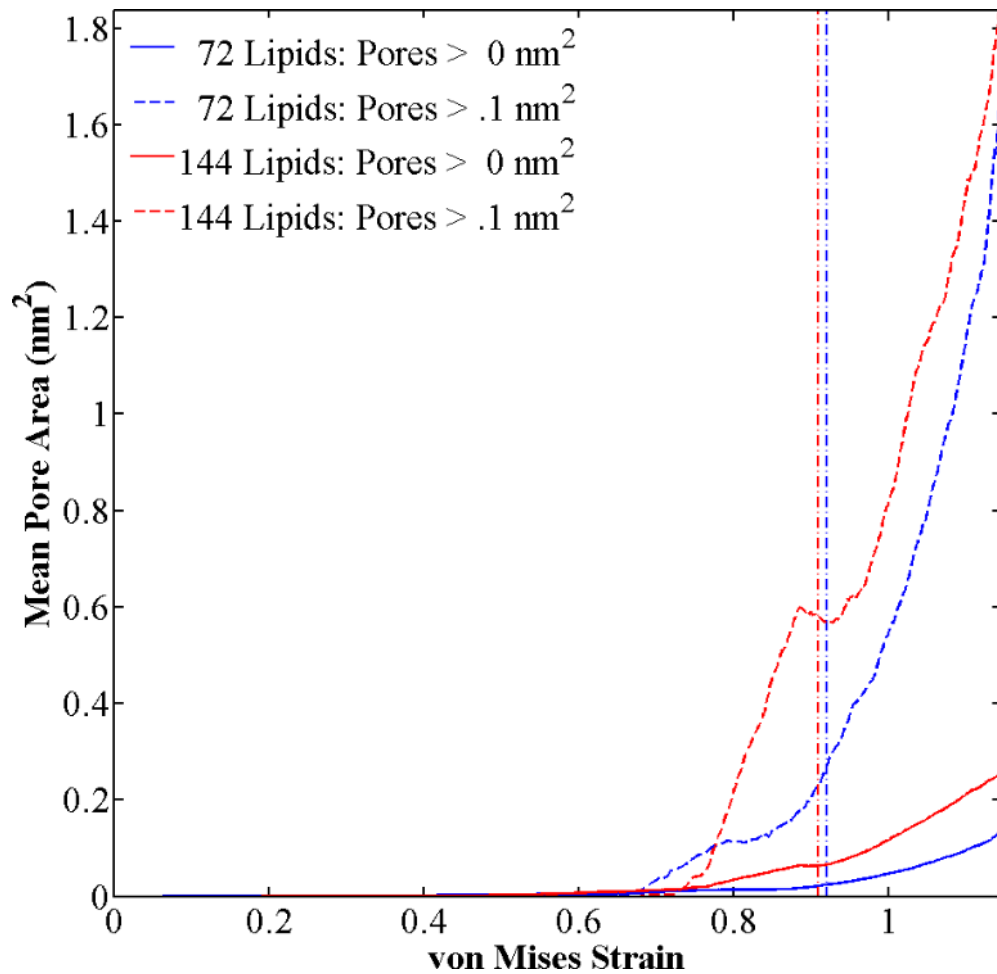


Figure 4.15 Mean pore area for different phospholipid bilayer size.

Notes: (seventy-two and one hundred forty-four phospholipids)

Both simulation models subjected to strip biaxial tension deformations at the von Mises strain rate of  $6.7e8$  /sec. Vertical dash lines color matched to their corresponding curve display when full water penetration occurs.

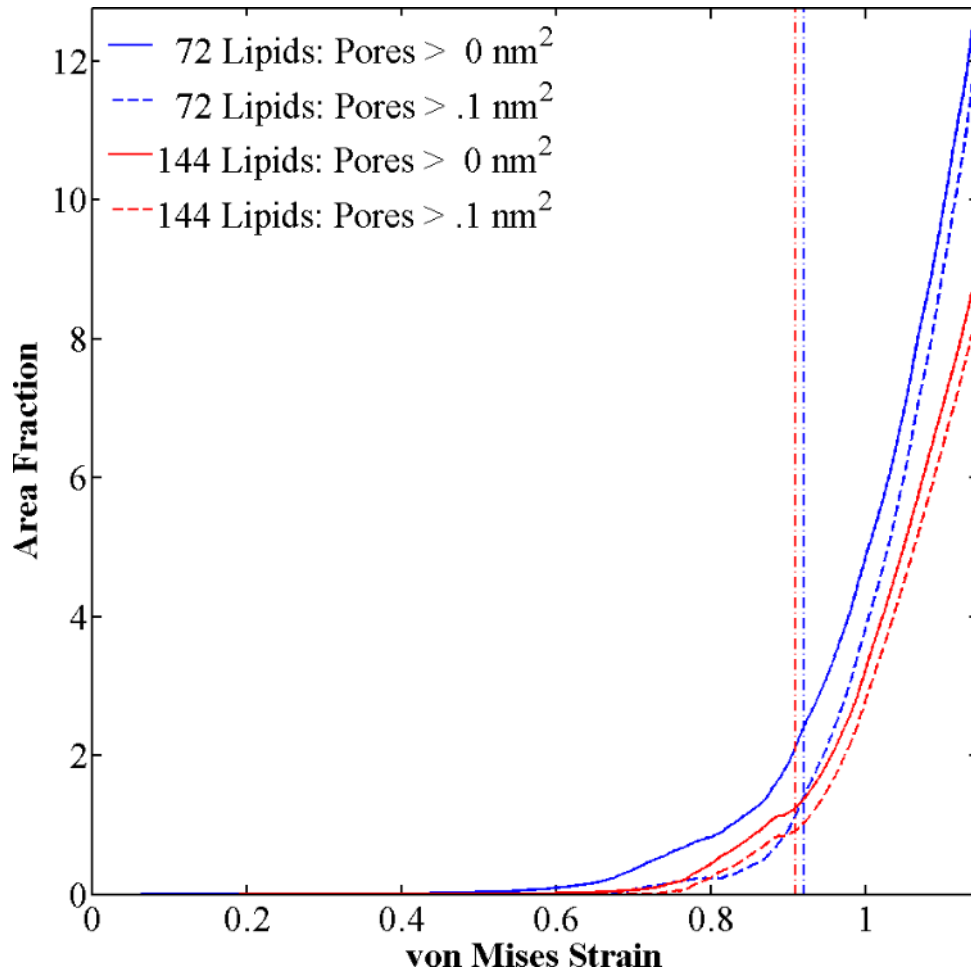


Figure 4.16 Area fraction for different phospholipid bilayer size.

Notes: (seventy-two and one hundred forty-four phospholipids)

Both simulation models subjected to strip biaxial tension deformations at the von Mises strain rate of  $6.7e8$  /sec. Vertical dash lines color matched to their corresponding curve display when full water penetration occurs.

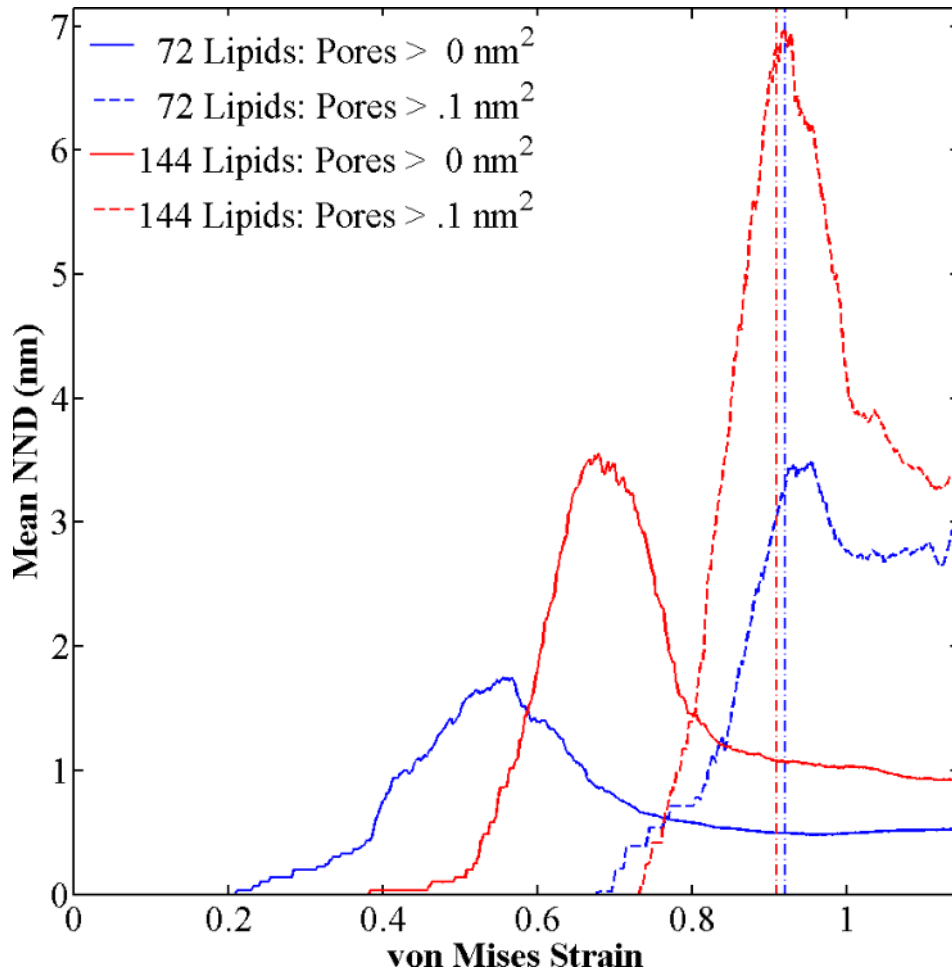


Figure 4.17 Mean nearest neighbor distance for different phospholipid bilayer size.

Notes: (seventy-two and one hundred forty-four phospholipids)

Both simulation models subjected to strip biaxial tension deformations at the von Mises strain rate of  $6.7e8$  /sec. Vertical dash lines color matched to their corresponding curve display when full water penetration occurs.

### 4.3 Stress State Comparison

The first peak stress for each von Mises strain rate can be seen in Table 4.3 along with the strains corresponding to points of interest.

Table 4.3 Mechanical Properties of the Seventy-Two Phospholipid Bilayer Under Different Stress States at a von Mises Strain Rate of  $6.7e8$  /sec

<b>Stress State</b>	$\sigma_{FirstPeak}^{VM}$ (MPa)	$\epsilon_{FirstPeak}^{VM}$	$\epsilon_{FirstPore}^{VM}$	$\epsilon_{Failure}^{VM}$
Strip Biaxial Tension	61.1	0.224	0.127	0.919
Uniaxial Tension	58.5	0.244	0.138	-
Equibiaxial Tension	65.0	0.232	0.111	0.728
Non-Equibiaxial Tension	64.0	0.233	0.152	0.711

It is apparent in Figure 4.18 that the stress state has affected the point of water penetration and, therefore, failure. Both the equibiaxial and non-equibiaxial cases both fail at von Mises strains that are considerably lower than that of the strip biaxial. Additionally, both the equibiaxial case and non-equibiaxial case maintain a higher consistent stress and the max stress values are similar in magnitude. Conversely, the uniaxial case seems comparable to the strip biaxial tension in stress, but does not have water penetration in the time simulated.

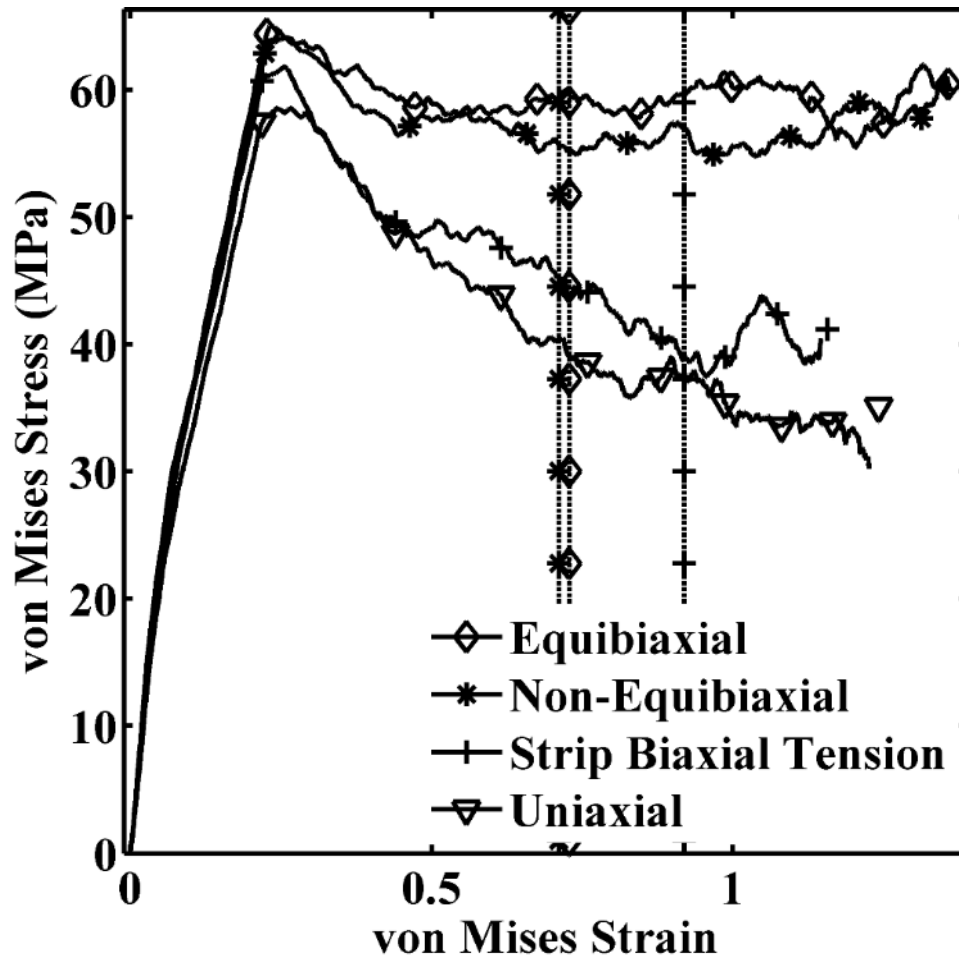


Figure 4.18 Von Mises stress-strain curve displaying the effect of the stress state.

Notes: (Equibiaxial, Non-Equibiaxial, Strip Biaxial, and Uniaxial Tension)  
 Simulations performed on the seventy-two phospholipid bilayer when subjected to a von Mises strain rate of  $6.7e8$  /sec. Vertical lines with markers matching their corresponding curve display when full water penetration occurs.

The surface tension in this case is very different in this case as can be seen in Figure 4.19. Although the same general trends exist, the surface tension is much more dampened and the decreasing z length seems to be making all cases decrease over time. Additionally, the differences in the magnitude of the max values are much more pronounced.



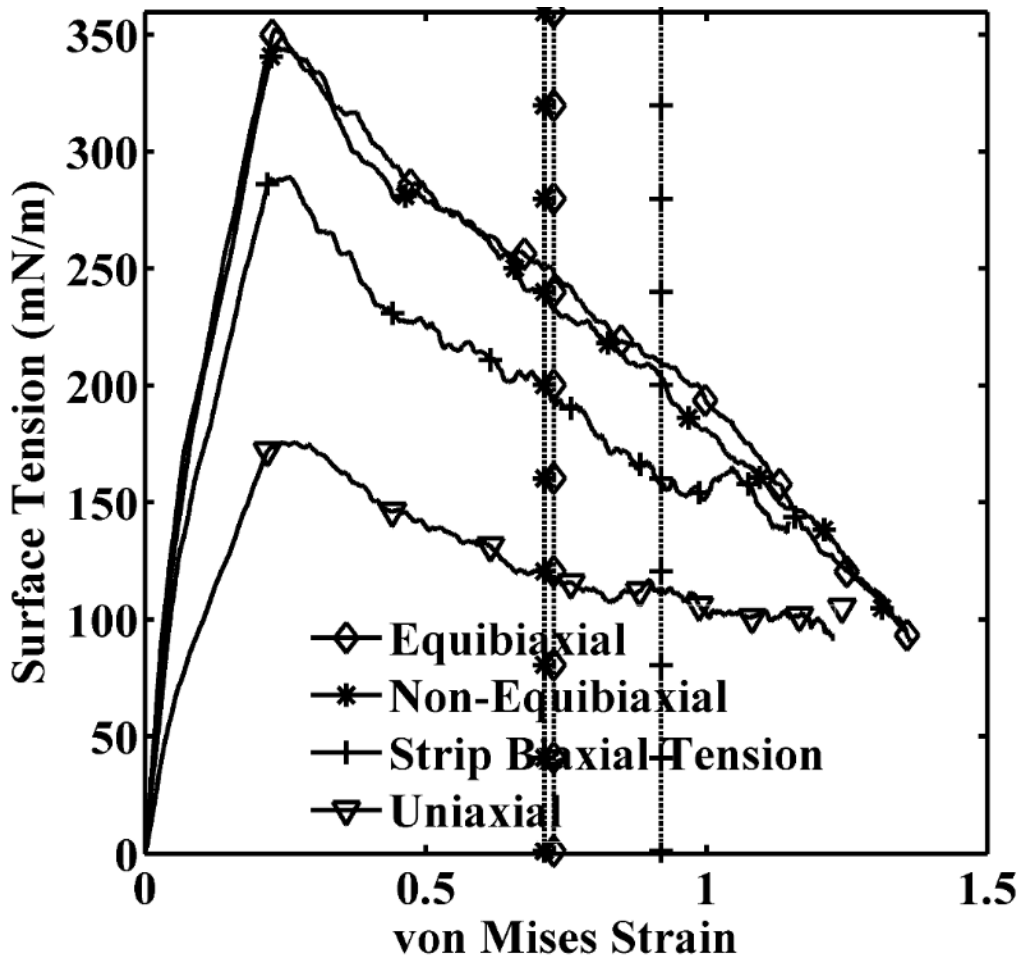


Figure 4.19 Surface tension-true strain curve displaying the effect of the stress state.

Notes: (Equibiaxial, Non-Equibiaxial, Strip Biaxial, and Uniaxial Tension)  
 Simulations performed on the seventy-two phospholipid bilayer when subjected to a von Mises strain rate of  $6.7 \times 10^8$  /sec. Vertical lines with markers matching their corresponding curve display when full water penetration occurs.

The image analysis results for the strip biaxial phospholipid bilayer size comparison can be seen in the following figures. Each figure has values for curves for all pores and for only pores  $> .1 \text{ nm}^2$ . Colored vertical dash lines correspond to water penetration for each strain rate. Figure 4.12 displays the progression of pore formation, Figure 4.13 displays the area density, Figure 4.14 displays the total pore area, Figure 4.15

displays the mean pore area, Figure 4.16 displays the area fraction, and Figure 4.17 displays the mean neighbor distance.

The equibiaxial and non-equibiaxial cases are close to one another in all properties examined. Both produce many more pores than the strip biaxial which forms only a few large pores.

These contrast greatly with the uniaxial case. Although it forms smaller pores as well, the magnitude of which is more comparative to the values for larger pores in the other cases and it forms few pores greater than  $.1\text{nm}^2$ . In accordance, it never achieves full water penetration which is reflected below by the missing black vertical dash line which would correspond to the uniaxial case.

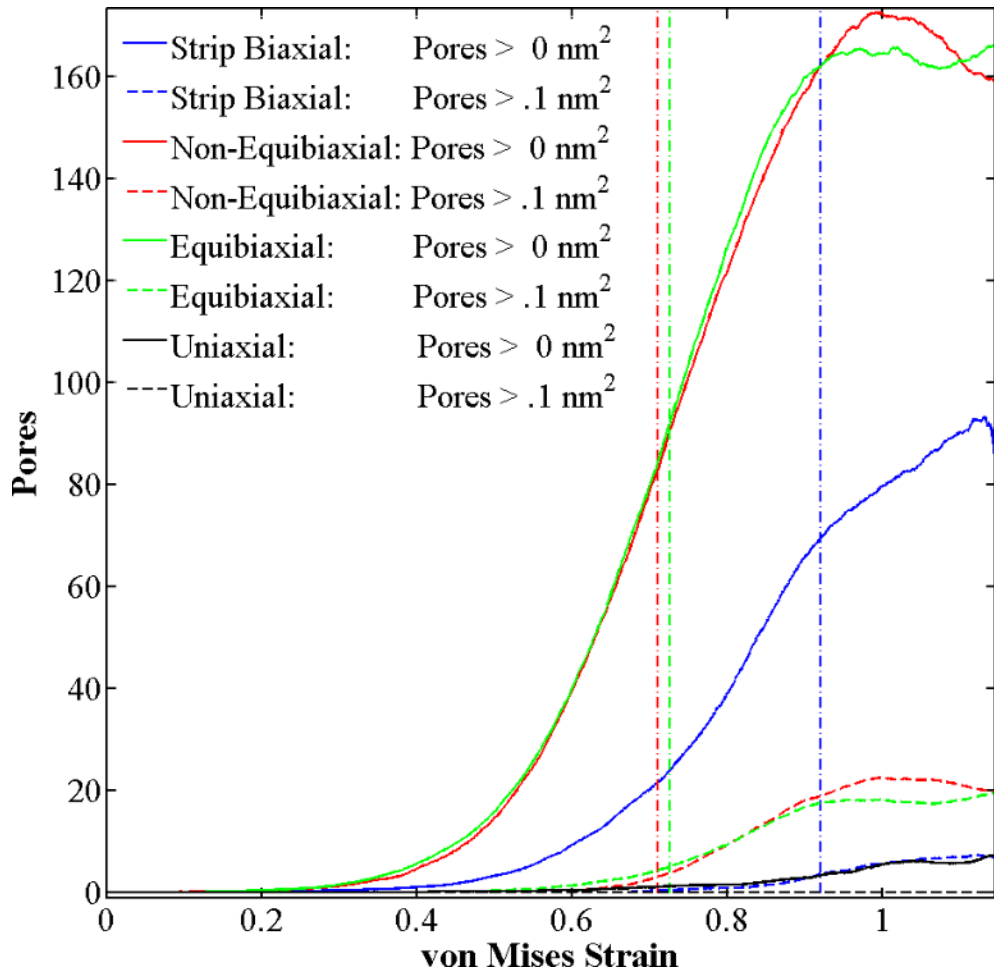


Figure 4.20 Pore count for different stress states.

Notes: (Equibiaxial, Non-Equibiaxial, Strip Biaxial, and Uniaxial Tension)

Simulations performed on the seventy-two phospholipid bilayer when subjected to a von Mises strain rate of  $6.7 \times 10^8$  /sec. Vertical dash lines color matched to their corresponding curve display when full water penetration occurs.

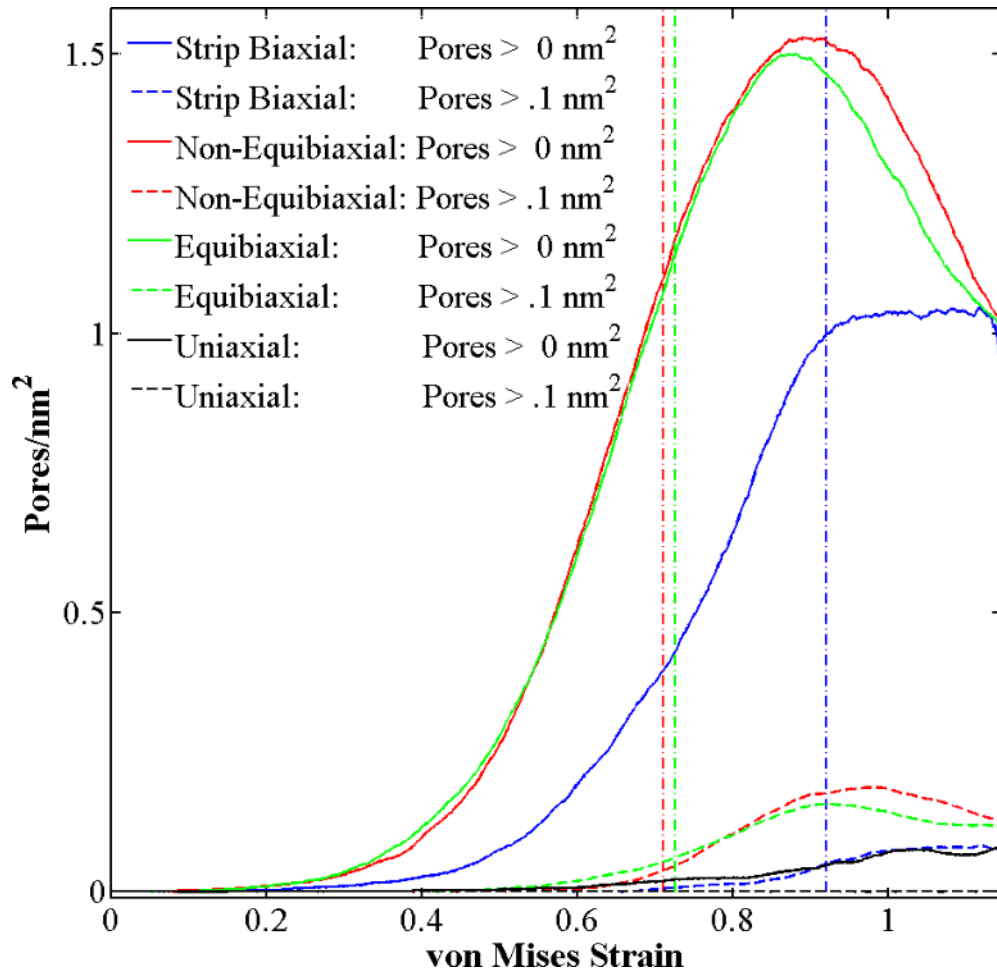


Figure 4.21 Area density for different stress states.

Notes: (Equibiaxial, Non-Equibiaxial, Strip Biaxial, and Uniaxial Tension)  
 Simulations performed on the seventy-two phospholipid bilayer when subjected to a von Mises strain rate of  $6.7 \times 10^8$  /sec. Vertical dash lines color matched to their corresponding curve display when full water penetration occurs.

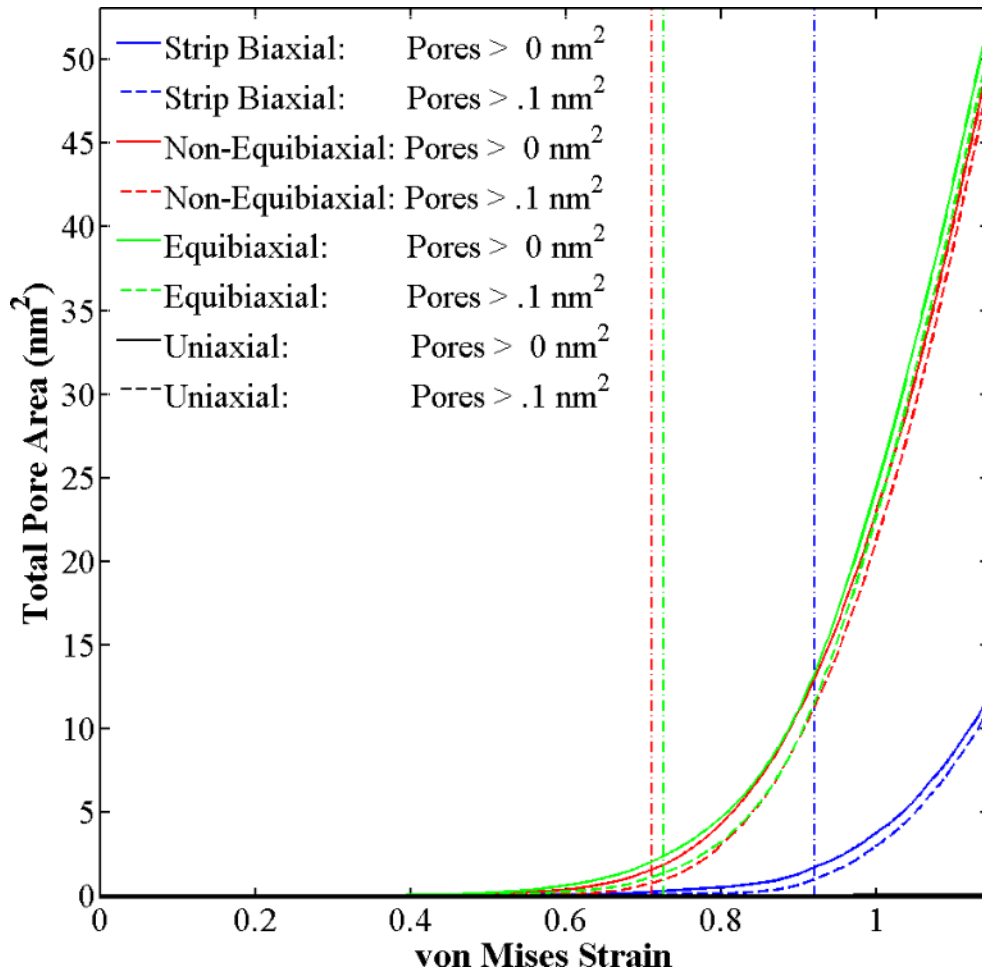


Figure 4.22 Total pore area for different stress states.

Notes: (Equibiaxial, Non-Equibiaxial, Strip Biaxial, and Uniaxial Tension)  
 Simulations performed on the seventy-two phospholipid bilayer when subjected to a von Mises strain rate of  $6.7 \times 10^8$  /sec. Vertical dash lines color matched to their corresponding curve display when full water penetration occurs.

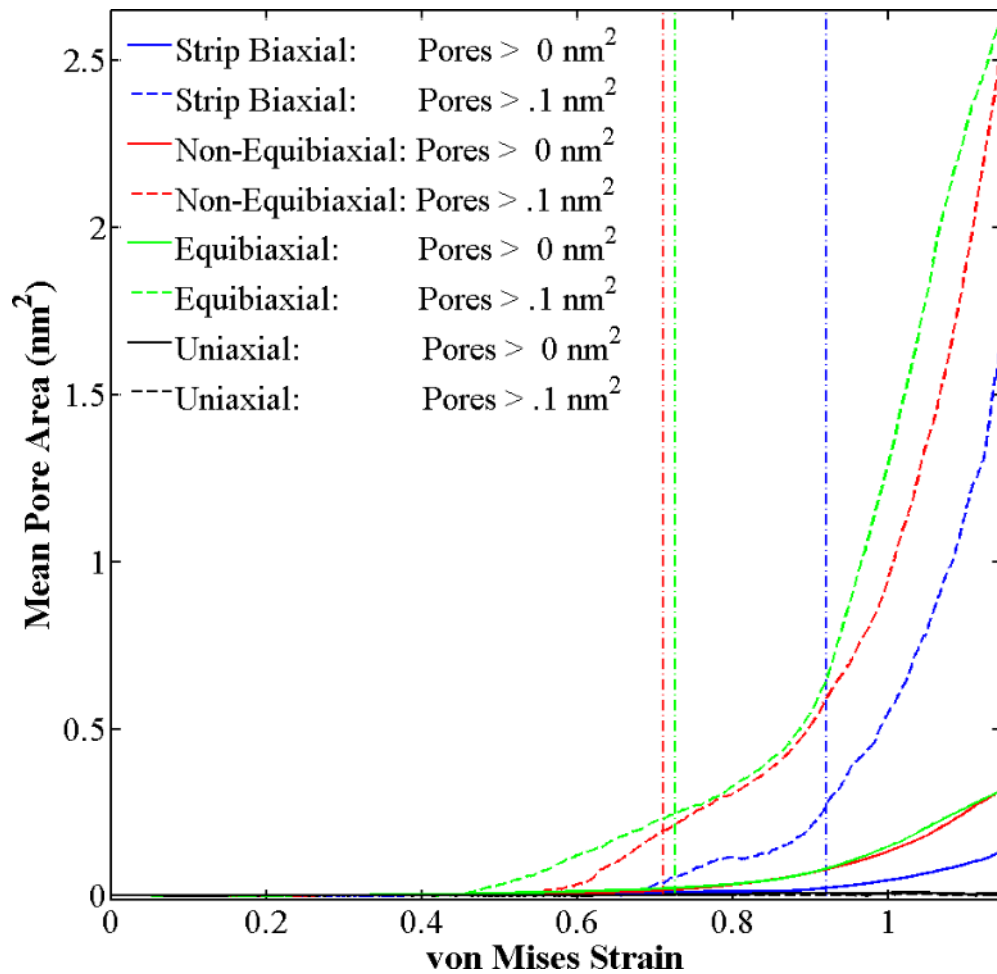


Figure 4.23 Mean pore area for different stress states.

Notes: (Equibiaxial, Non-Equibiaxial, Strip Biaxial, and Uniaxial Tension)

Simulations performed on the seventy-two phospholipid bilayer when subjected to a von Mises strain rate of  $6.7 \times 10^8$  /sec. Vertical dash lines color matched to their corresponding curve display when full water penetration occurs.

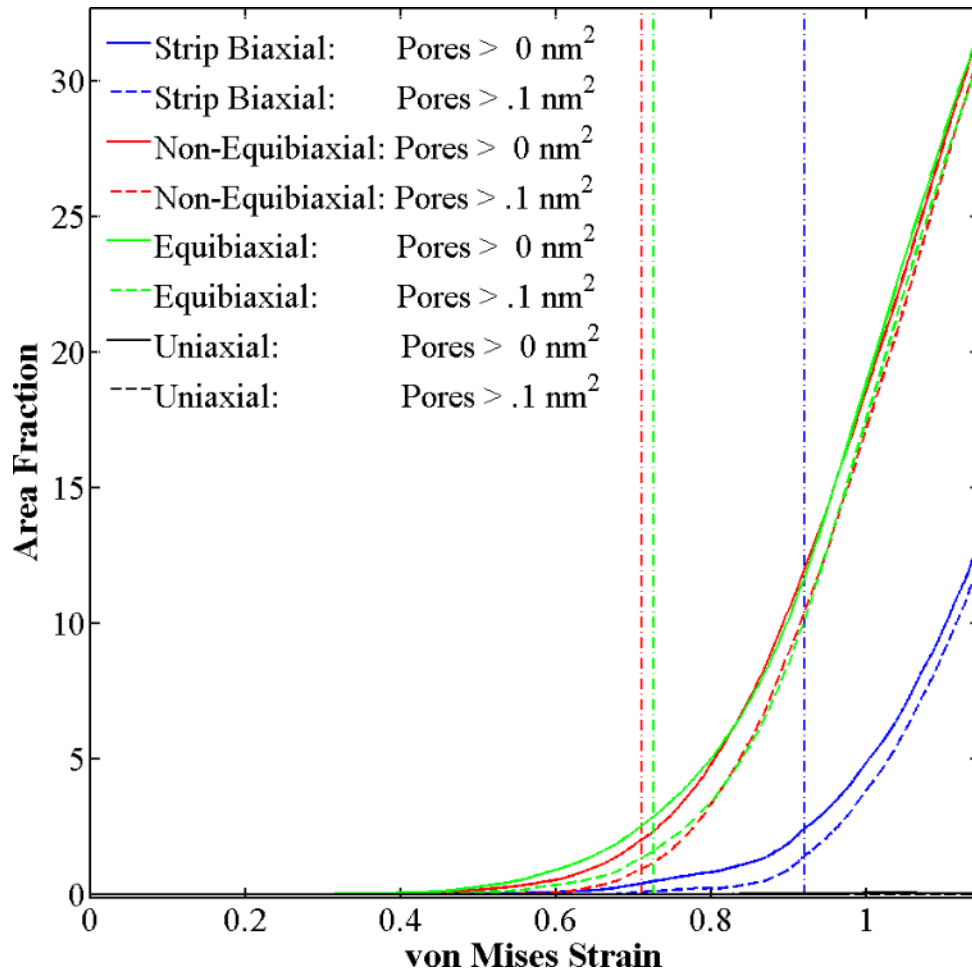


Figure 4.24 Area fraction for different stress states.

Notes: (Equibiaxial, Non-Equibiaxial, Strip Biaxial, and Uniaxial Tension)  
 Simulations performed on the seventy-two phospholipid bilayer when subjected to a von Mises strain rate of  $6.7 \times 10^8$  /sec. Vertical dash lines color matched to their corresponding curve display when full water penetration occurs.

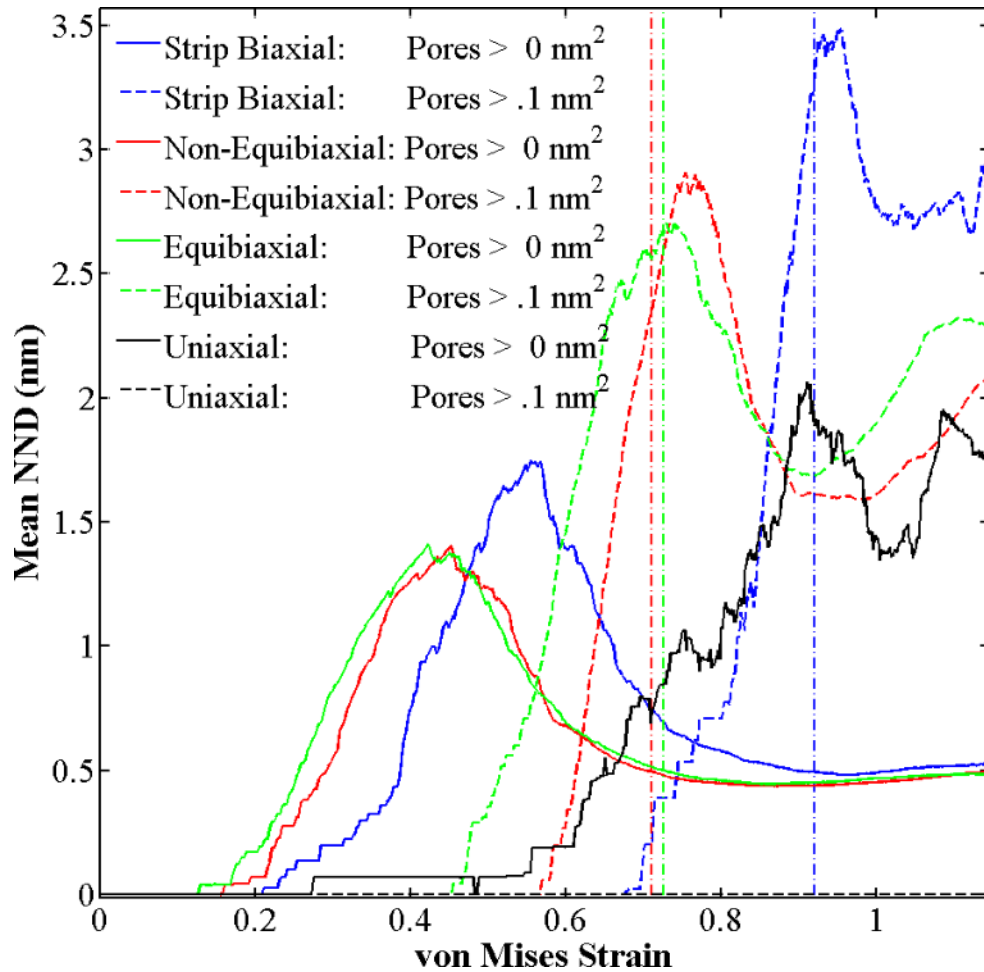


Figure 4.25 Mean nearest neighbor distance for different stress states.

Notes: (Equibiaxial, Non-Equibiaxial, Strip Biaxial, and Uniaxial Tension)  
 Simulations performed on the seventy-two phospholipid bilayer when subjected to a von Mises strain rate of  $6.7 \times 10^8$  /sec. Vertical dash lines color matched to their corresponding curve display when full water penetration occurs.

A progression of the simulation overlaid on the von Mises stress-strain curve is presented for strip biaxial tension in Figure 4.26, equibiaxial tension in Figure 4.27, non-equibiaxial tension in Figure 4.28, and uniaxial tension in Figure 4.29 to illustrate the progression of damage. Looking at the figures together reveals that the initial slope of the curves all change around twenty megapascals indicating some change occurs and that the first pore always seems to appear at around forty megapascals. Furthermore, they



confirm the observations above. Specifically, it confirms that the equibiaxial and non-equibiaxial cases have formed multiple pores by the time water penetration occurs and as poration continues they have a relatively high number of pores forming across the area of the phospholipid bilayer. The strip biaxial case has fewer pores, but they are larger in comparison to the area of the phospholipid bilayer. In contrast, no pores can be seen easily in the uniaxial case confirming that no pores form for the duration of the simulation.

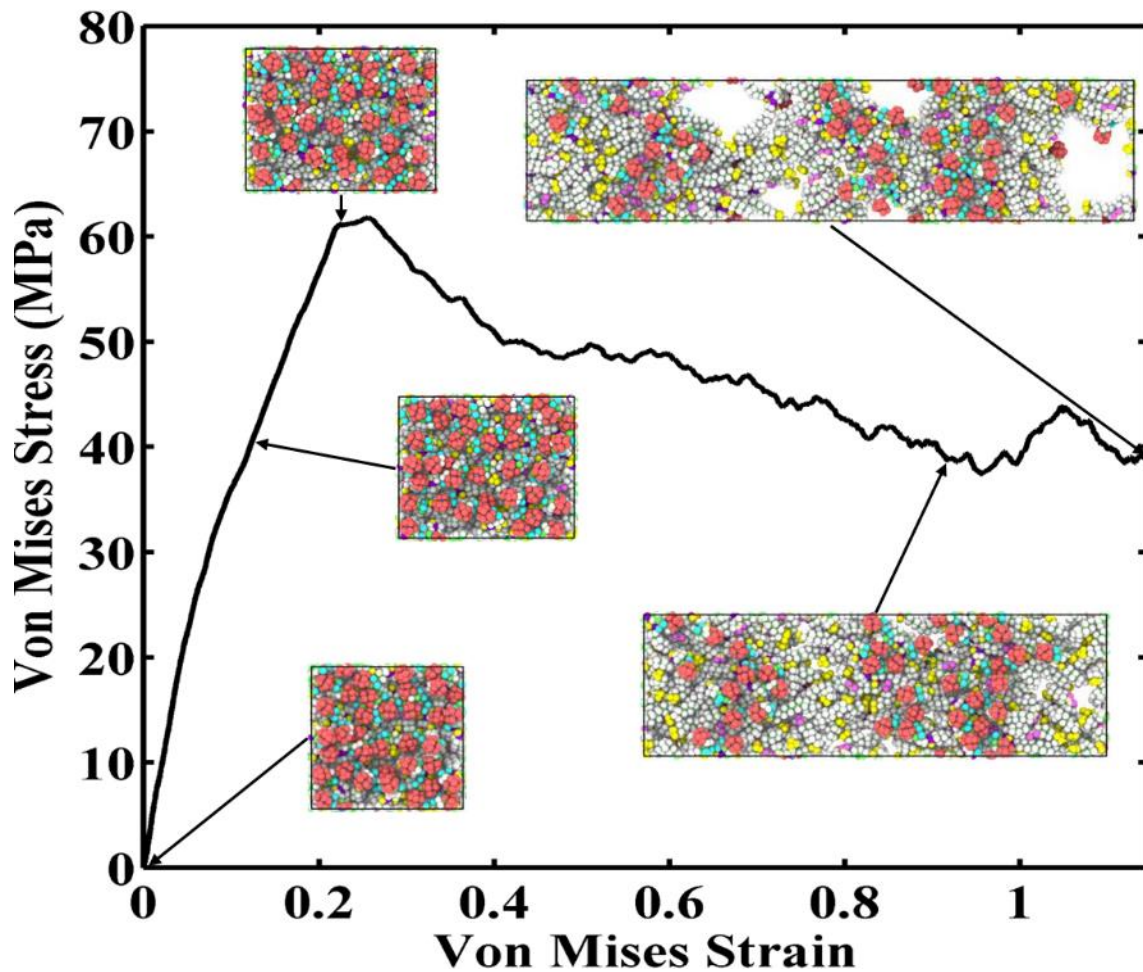


Figure 4.26 Von Mises stress-strain curve for the strip biaxial deformation conditions resulting in a von Mises strain rate of  $6.7e8$  /sec.

Notes: Following the curve from left to right, snapshots of the top of the phospholipid bilayer with water hidden show the phospholipid bilayer during the initial structure, the point when the first detected pore appeared, the first peak stress, water penetration, and the last recorded structure.

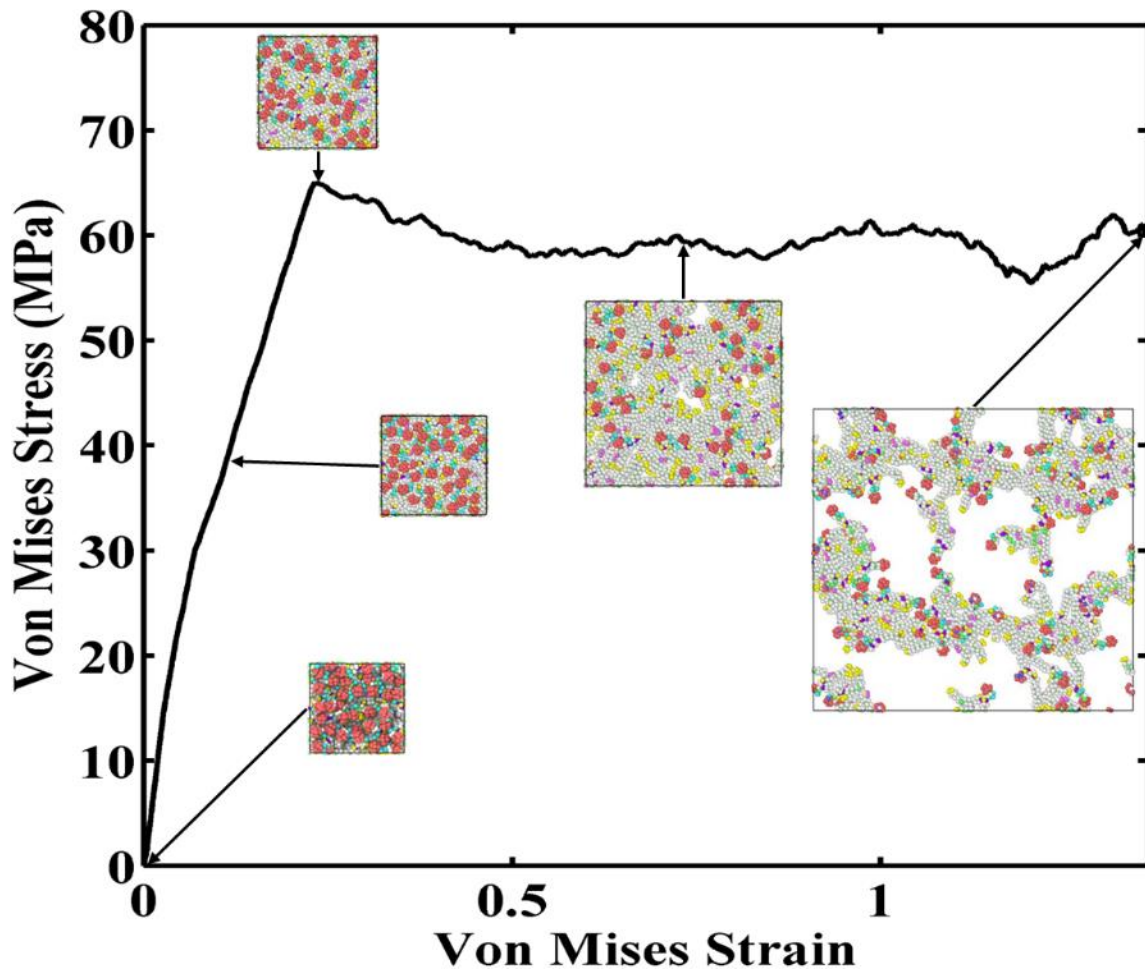


Figure 4.27 Plot of von Mises stress and strain for the equibiaxial deformation conditions resulting in von Mises strain rate of  $6.7e8$  /sec.

Notes: Following the curve from left to right, snapshots of the top of the phospholipid bilayer with water hidden show the phospholipid bilayer during the initial structure, the point when the first detected pore appeared, the first peak stress, water penetration, and the last recorded structure.

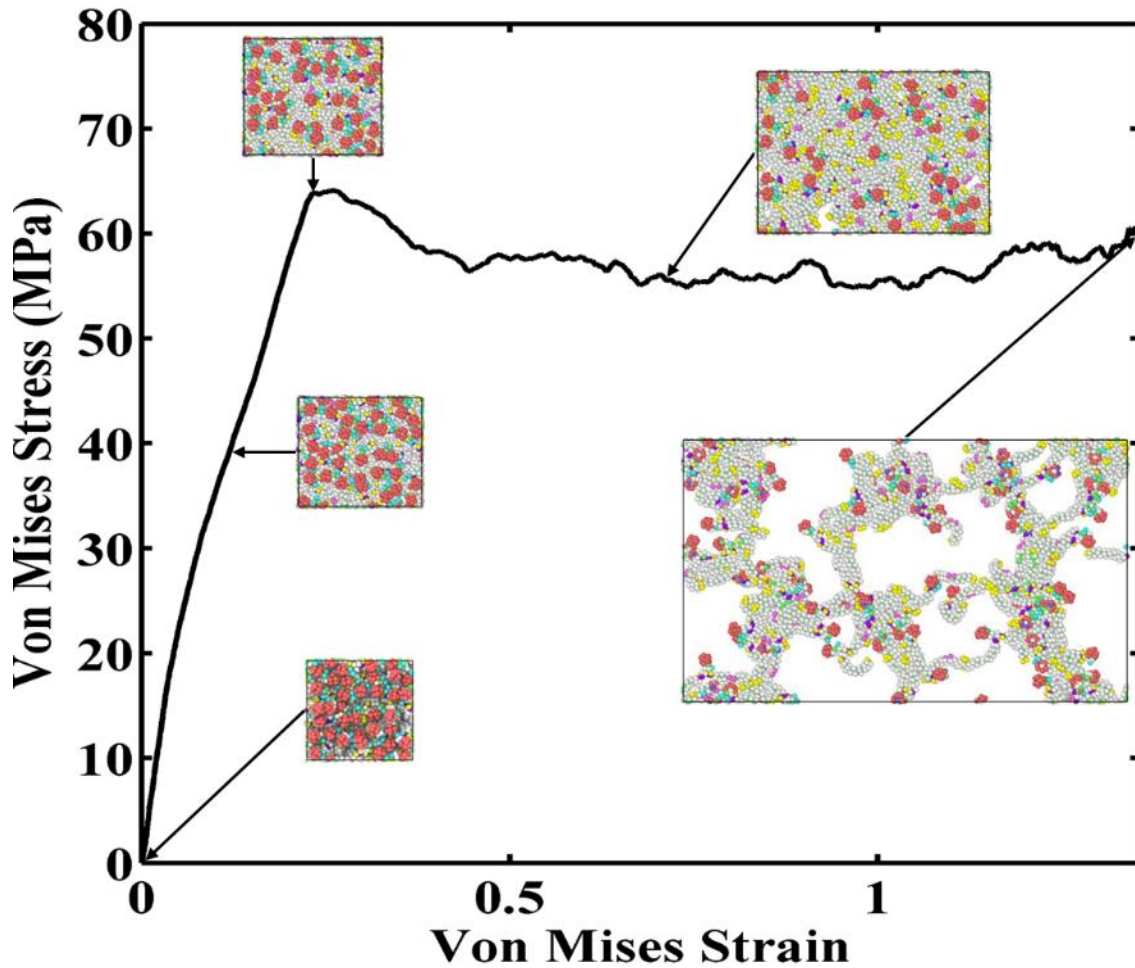


Figure 4.28 Plot of von Mises stress and strain for the non-equibiaxial deformation conditions resulting in a von Mises strain rate of  $6.7e8$  /sec.

Notes: Following the curve from left to right, snapshots of the top of the phospholipid bilayer with water hidden show the phospholipid bilayer during the initial structure, the point when the first detected pore appeared, the first peak stress, water penetration, and the last recorded structure.

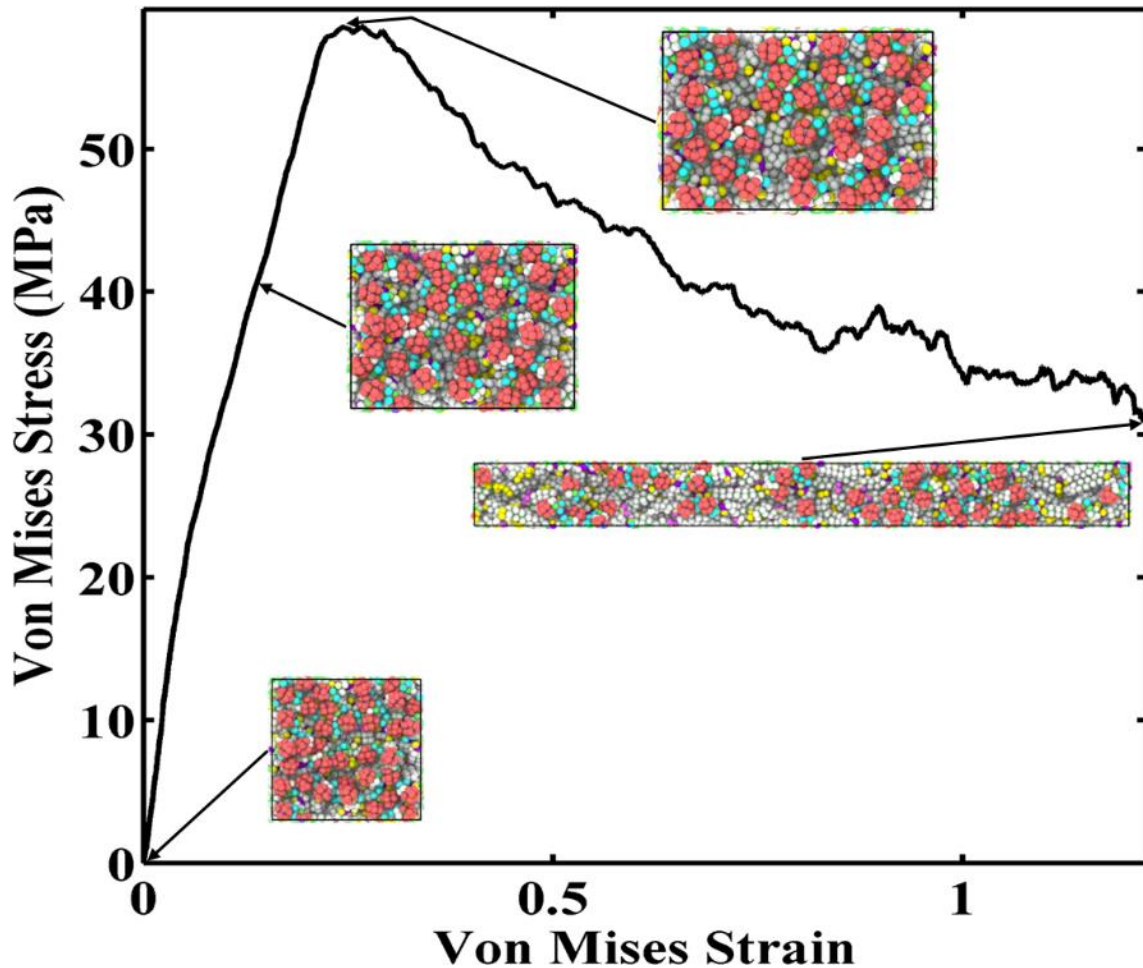


Figure 4.29 Von Mises stress-strain curve for the uniaxial deformation conditions resulting in a von Mises strain rate of  $6.7e08/\text{sec}$ .

Notes: Following the curve from left to right, snapshots of the top of the phospholipid bilayer with water hidden show the phospholipid bilayer during the initial structure, the point when the first detected pore appeared, the first peak stress, and the last recorded structure.

The strain space is explored in Figure 4.30. The principle strains are related to one another for each of the stress states creating a map of bilayer damage and showing a generalization of where the most detrimental stress states occur.

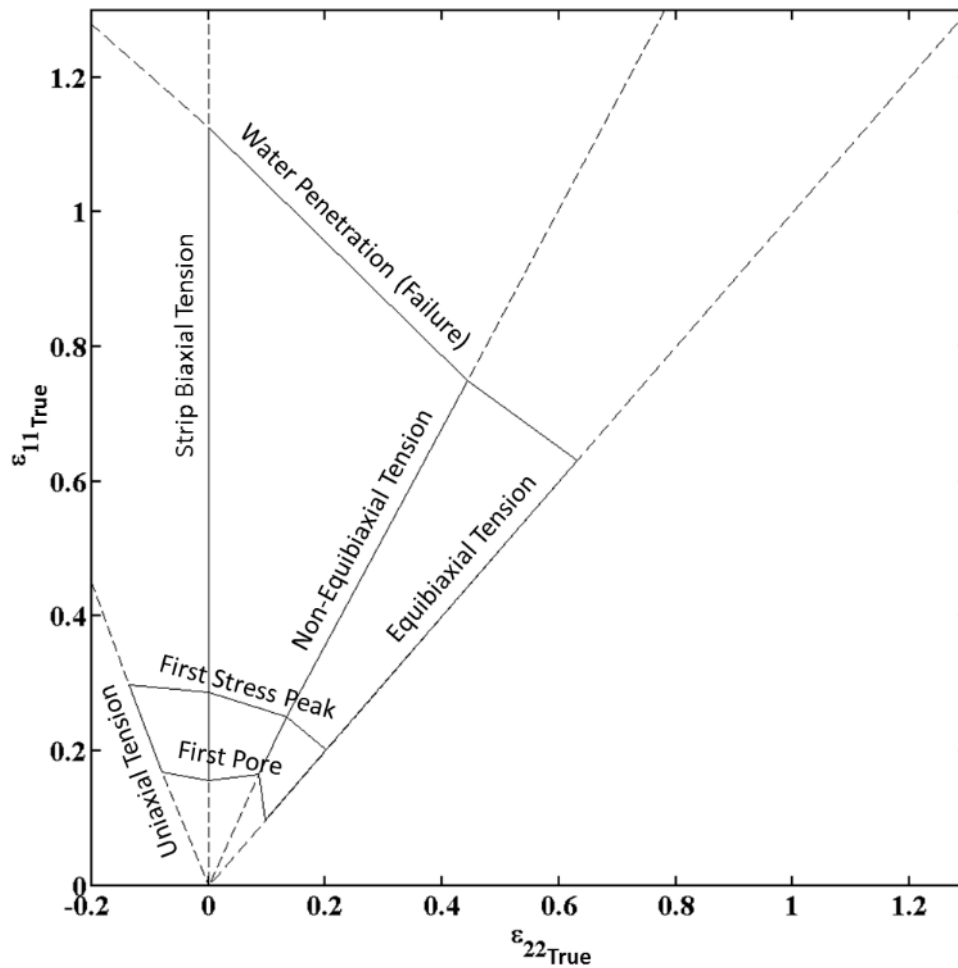


Figure 4.30 Examination of the strain space for different stress states.

Notes: (Equibiaxial, Non-Equibiaxial, Strip Biaxial, and Uniaxial Tension) Simulations performed on the seventy-two phospholipid bilayer when subjected a von Mises strain rate of  $6.7 \times 10^8$  /sec. The First Pore, First Stress Peak, and Water Penetration (Failure) forming curves and each stress state have been labeled.

#### 4.4 Overall Curve Trends

All of the cases shared a similar trend in the beginning of the plot. Specifically, an initial linear portion that was used for calculating elastic constants followed by a secondary linear region which continued until the initial peak. This trend can be seen in Figure 4.31. The initial peak was either the max stress or followed by the max stress

peak. Additionally, the point at which the first pore appeared corresponded closely with forty megapascals for all cases except 72x1y0 which did not reach forty megapascals.

After the initial peak, all cases except 72x1y0 began a period where the stress decreased noticeably. The 72x1y0 case fluctuated around its initial peak value before having a greater peak stress toward the end of deformations. All other cases appeared to reach a point where the stress stabilized as seen in previous figures.

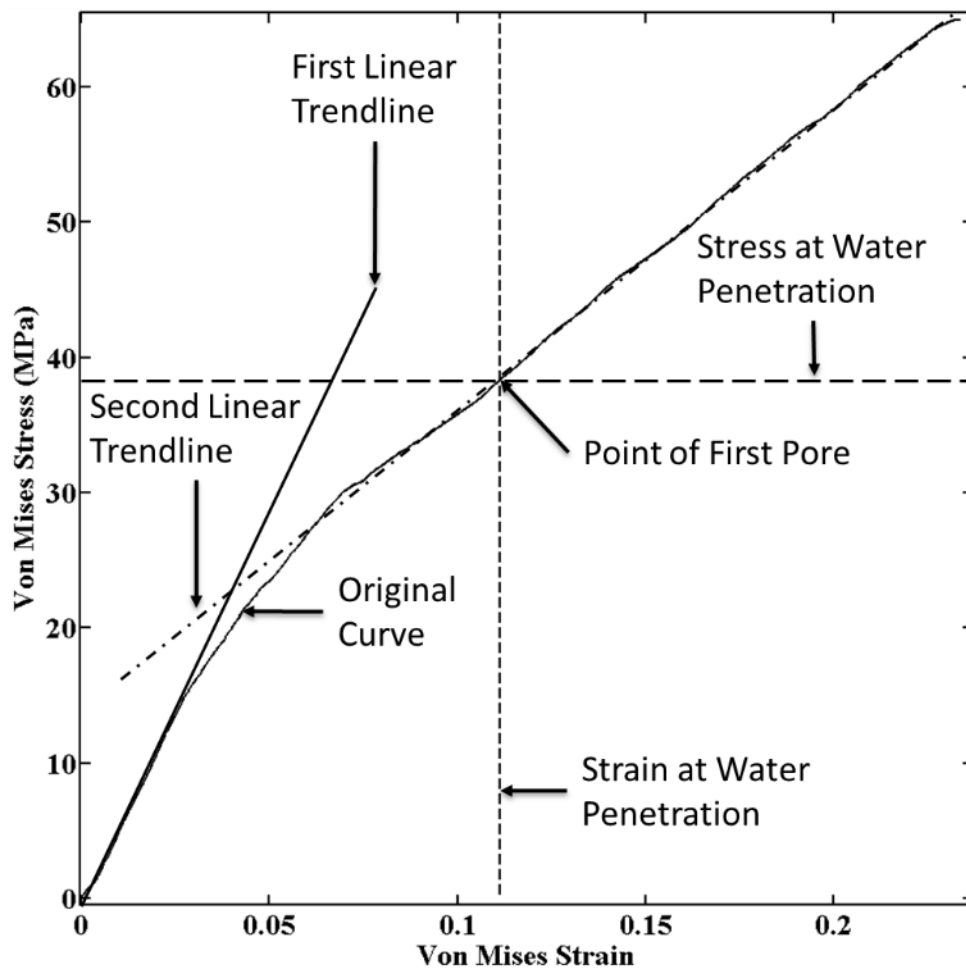


Figure 4.31 Linear portions of the 72x2.8y2.7 case.

Notes: Trendlines have been added for both linear regions where the solid trendline indicates the region used for elastic constant deformations. Lines indicating the stress and strain at the point where the first pore is detected are included as well.

Another interesting trend to note is the pore formation and area density. At some point, each simulation had a plateau effect occur where it appeared the number of pores even became constant or actually began to decrease.

#### **4.5 Elastic Properties**

The elastic modulus was found to be  $E = 370 \text{ MPa}$  as seen in Figure 4.32. Poisson's ratio was found to be  $\nu = 0.3$  for the region highlighted in Figure 4.32 and  $L_{bilayer}$  assumed to be  $5 \text{ nm}$ . These were used to calculate the bulk modulus  $K_b = 310 \text{ MPa}$  and shear modulus  $\mu = 140 \text{ MPa}$ .



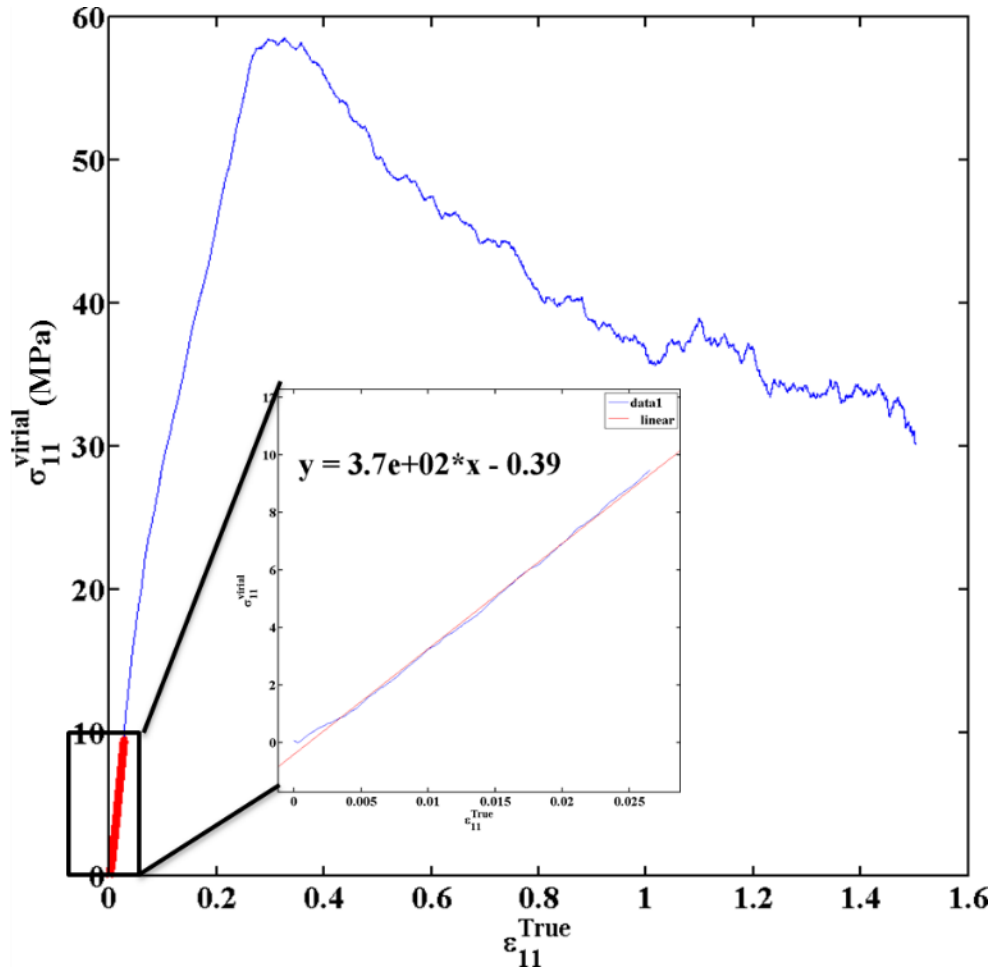


Figure 4.32 Elastic modulus determination using the uniaxial stress-strain curve and a trendline.

Notes: Simulation performed using the seventy-two phospholipid bilayer under uniaxial deformation conditions. Elastic modulus determined using a trendline of the initial linear portion of the curve.

Applying a similar technique to the surface tension vs true strain for the equibiaxial case yields the area compressibility modulus  $K_a = 1.9 \frac{N}{m}$ . Multiplying the bulk modulus found above and the initial bilayer height (due the relation  $K_a = K_b * L_{bilayer}$ ) yields a value of  $K_a = 1.86 \frac{N}{m} \cong 1.9 \frac{N}{m}$  which agrees well with the directly measured value.

## CHAPTER V

### DISCUSSION

#### 5.1 Area per Lipid

The properties of POPC are well known, therefore, properties such as area per lipid can be verified. For the current simulations, the area per lipid is  $\sim 63.7 \frac{A^2}{Lipid}$  for the 72 phospholipid structure and  $\sim 60.1 \frac{A^2}{Lipid}$  for 144 phospholipid structure. These are a little lower than original value of  $64.7 \frac{A^2}{Lipid}$  reported for the force field (Jeffery B. Klauda et al., 2010).

#### 5.2 Surface Tension vs von Mises Stress

Surface tension is often used in the description of phospholipid bilayers and, correspondingly, the elastic area [compressibility] modulus  $K_a$ . The argument for this seems to be that the phospholipid bilayer properties rely almost solely on the elastic area modulus (Cevc). Experimentally, the bilayer is tested in plane leading to a natural adoption of a 2-D definition of stress and stress constants. However, this is counter-productive when applied to computational modeling because it deviates from normal mechanics practice and introduces an extra variable that must be accounted for explicitly which can normally be ignored or assumed constant experimentally. In the case of surface tension, the derivation for molecular dynamics uses the entire box height, but this

is only accurate when the water layer is small (Zhang et al., 1995). During equilibrium simulations, the bilayer height can be assumed constant as in experiments, but during mechanical deformation this assumption is invalid because the bilayer height decreases as the area increases. The alternative proposed is the von Mises equivalent stress which accounts for all components of the stress tensor. However, in the case of the phospholipid bilayer orthogonal deformations, shear components can be neglected because 1. They are significantly lower than the principle stresses and 2. They are not affected by the tensile deformations and add noise because  $\sigma_{12}$ ,  $\sigma_{13}$ , and  $\sigma_{23}$  fluctuate between -5 and 5 MPa both during equilibrium and deformations. This is consistent with the equation for surface tension which also omits the shear stresses. Note that the stress perpendicular to the bilayer is also very small in relation to the other principle stresses during deformations, but it is the same magnitude as the other principle stresses during the equilibrium state and therefore required to accurately calculate the correct surface tension of zero.

In favor for using the von Mises equivalent stress instead of surface tension, plots of the same data should be compared between the two to verify it is appropriate. To do so, the reader is referred to compare Figure 4.2 against Figure 4.3 and Figure 4.18 against Figure 4.19 which have been reproduced in Figure 5.1. When comparing the plots, it is possible to distinguish that the two plots are of the same data, but there are major differences that are apparent. By accounting for the lipid bilayer height (estimated) to calculate surface tension as stress, the reported bilayer stress is initially magnified, which corresponds to the bilayer at full height, with respect to the middle of the plot. This is easiest to see in the top two plots by comparing the first and mid peaks of the case with

the strain rate of  $1.7e8/\text{sec}$  where the surface tension's peak is greater than the mid peak and the opposite is true for the von Mises stress. This becomes even more apparent at the end of the curves where the decrease in height significantly effects the overall trend of all the plots as the bilayer height drops. This drop results in plots of continuously decreasing surface tension throughout the simulation which does not readily provide any useful information. Conversely, the von Mises stress plots yield useful information in a few respects: 1. It is a standard stress measure in that it accounts for all directions of the bilayer 2. Because it relies only on the stresses and knowledge of the system tells us that only two principle stresses are significantly acting on the equivalent stress, it gives an idea what the component stresses may be doing. This will be discussed further below. Due to these reasons, discussion will focus primarily on the von Mises stress except where comparing to the values of prior studies.

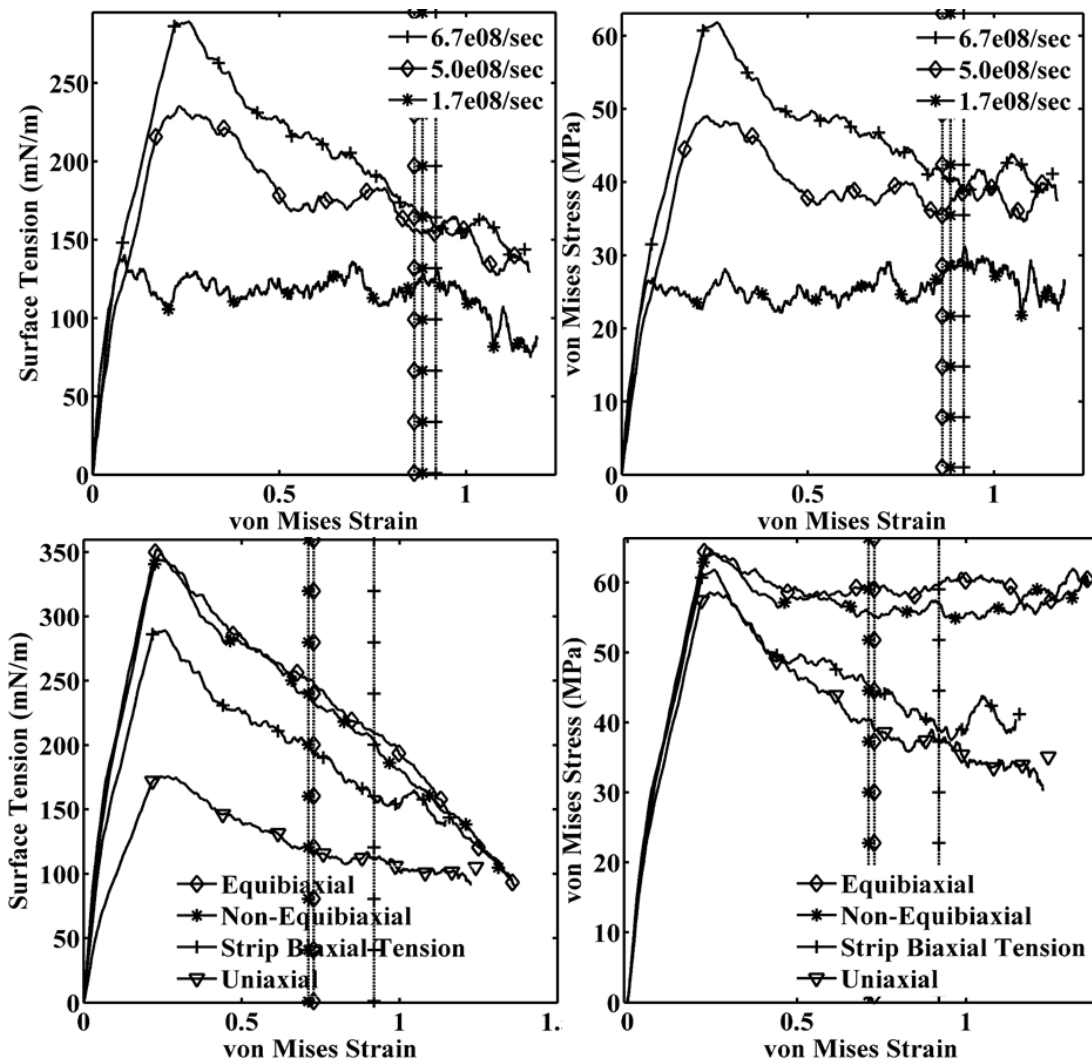


Figure 5.1 Comparison of the surface tension-von Mises strain curves and the von Mises stress-strain curves

### 5.3 Selection of Deformation Rates

Of particular interest in the current study were high rate deformations due to the motivation being traumatic brain injury. That said, when considering strain rates, the rates used were extremely high (on the order of  $10^8/sec$ ) as is typical when performing molecular dynamics. However, based on the size of our system, if the velocity is

translated directly to macroscale deformations, they are only a few meters per second which is often much slower than rates experienced during injuries.

Therefore, rates were chosen to encompass the upper rates already explored in literature and to exceed those rates. Also, three separate rates were considered so the deformation rates and maximum stress values could be correlated assuming a rate dependence. Additionally, when plotting the von Mises strain rates against the stress magnitude at the first peak value, a linear trend resulted. This indicates the phospholipid bilayer stress should be easy to determine given a strain rate. However, it is apparent this linear behavior is limited to some range of deformation rates because it will not hold true when the von Mises strain rate is equal to zero. Consider the following for this case:

$$y = 6.9e - 8 * x + 15 \quad (5.1)$$

$$\text{When } x = 0, \quad y = 15MPa$$

This seems incorrect due to the von Mises stress being zero when at equilibrium- which was the starting point. So there is likely a point where the linearity is no longer valid, likely at quasistatic rates. There should also be an upper limit due to simulation restraints of tensile deformations because at some point the molecules will not move fast enough to keep up with the simulation box when a deformation control is used.

As the reason for their upper limit, Koshiyama and Wada (2011) noted that the diffusion of water was lower than the rates tested. However, no problems were observed for either box diffusion or penetration into the phospholipid bilayer. Additionally, based on an approximation using the equation

([http://www.physiologyweb.com/calculators/diffusion\\_time\\_calculator.html](http://www.physiologyweb.com/calculators/diffusion_time_calculator.html)):

$$t \cong \frac{x^2}{2 * D} \quad (5.2)$$

where  $t$  is time,  $x$  is the distance traveled, and  $D$  is diffusion coefficient constant and the self-diffusion constant of water at 308.15 K is  $D = 2.895e - 5 \frac{cm^2}{s}$  (Holz, Heil, & Sacco, 2000). When assuming the water will not have to diffuse more than three nanometers (which is greater than half the phospholipid bilayer height at equilibrium) due to penetration occurring through both leaflets, the time 1.55 ns is determined. This is close to the fastest observed times of penetration,  $\sim 1.5$  ns. However, the phospholipid bilayer also decreases in height as the bilayer is deformed, so the true time being less than the estimate is possible.

## 5.4 Strain Rate Dependency

### 5.4.1 Effect of Strain Rate

The simulations performed indicate the phospholipid bilayer is highly dependent on strain rate with regards to the peak stress, however, the strain at which poration occurs appears to be less dependent on rate. The higher strain rates result in higher max stress values. Surprisingly, the first peak values plotted against their respective von Mises strain created a perfectly linear relation. This indicates that some physical effect is dictating when the first peak stress occurs. Because the phospholipid bilayer is in the fluid phase, it is assumed the behavior is related to the viscosity of the phospholipid bilayer because it would result in an initial resistance to change. In addition, it is possible that some internal phospholipid rearrangement has begun as a result of internal void formation and phospholipid tail detanglement. However, determining how the chains rearrange and the bilayer viscosity are beyond the scope of the present study. The chain

rearrangement and internal membrane void formation may be revisited in the future as more effective detection methods developed. However, the determination of the viscosity appears to be nontrivial and new methods are still being developed for its determination (Hormel, Kurihara, Brennan, Wozniak, & Parthasarathy, 2014).

#### **5.4.2 Effect on Pore Formation and Water Penetration**

Surprisingly, the strain rate had little correlation with when the bilayer failed. There did not seem to be any pattern to the pore formation when just examining the image analysis curves. In addition, despite having a lower number of pores, the 72x1y0 case had the highest pore area. Evan Evans, Volkmar Heinrich, Florian Ludwig, and Wieslawa Rawicz (2003) proposed two distinct pathways to failure which may help to explain this interesting trend. Specifically, they stated that lower rates were limited by pore enlargement and higher rates were limited by pore formation. The systems tested appear to follow this pattern. The 72x1y0 case develops only a few larger pores, but they expand considerably more than those of the 72x3y0 and 72x4y0 cases, as can be seen in 0. This discovery is a bit surprising considering the rates being tested. In their original paper, E. Evans et al. (2003) worked experimentally at a loading rate of  $\sim .01 - 100 \frac{mN}{s}$ . This is starkly different from the current cases where the 72x1y0 case has a loading rate of  $1.2e12 \frac{mN}{s}$ . If true, this relation could possibly help explain why the 72x1y0 case does not peak and decrease as the other cases, but instead fluctuates around a constant value after peaking before the other cases with regard to strain. Koshiyama and Wada (2011) also noted that there was a trend of higher pore counts when higher rates were used.



In addition,  $\epsilon_{FirstPore}^{VM}$  and  $\epsilon_{Failure}^{VM}$  show no trend but each is similar among the different strain rates, which indicates that the strain at failure is a limiting factor. In other words, the bilayer fails at a certain strain rather than a stress and it is assumed that the differences seen are due to error rather than true differences. The 72x1y0 and 72x4y0 cases reached the pore formation plateau region mentioned shortly after water penetration occurred. However, the 72x3y0 case continued to produce more pores before having a shorter plateau region and decreasing rapidly. This seems to indicate the process is more complex than the just two distinct pathways as suggested by E. Evans et al. (2003).

### 5.4.3 Comparison with Literature

This study agrees with experimental and computational studies qualitatively with regards to the phospholipid bilayer being rate dependent. This trend is simple to see, but validating results quantitatively is more difficult. Experimentally, phospholipid bilayers have been found to lyse at surface tensions of less than  $.04 \frac{N}{m}$  even when stiffened with cholesterol (Needham & Nunn, 1990). However, due to the high rates, experimental results for surface tension cannot be directly compared to those of simulation. This requires that estimates based on experimental data be utilized such as in the equation (E. Evans et al., 2003):

$$\frac{\sigma}{\sigma_{\delta}} \cong \ln \left( \frac{\mathcal{R}_{\sigma}}{\nu_{0\delta} \sigma_{\delta}} \right) \quad (5.3)$$

where  $\sigma$  is the rupture tension,  $\sigma_{\delta}$  is the tension scale for rate exponentiation,  $\nu_{0\delta}$  is a rate prefactor, and  $\mathcal{R}_{\sigma}$  is the loading rate in mN/m as was done in Tomasini et al. (2010) who obtained good agreement with their results at a rate of  $1.4e9$  mN/m/s. However,

taking a similar approach and assuming the values for POPC should be similar to DOPC

( $\sigma_\delta = 4.0 \frac{mN}{m}$ ,  $v_{0\delta} = .22/s$ ) and  $\mathcal{R}_\sigma = 1.2e12 \frac{mN}{s}$  yields 111.8mN/m. The max rate

applied  $\mathcal{R}_\sigma = 3.1e12 \frac{mN}{s}$  yields  $115.6 \frac{mN}{s}$ . Both of these are much lower than the

approximate measured values of 141 and 240 for the lowest and highest rates. Therefore, max stress values do not agree with other simulations or with experimental estimates.

However, the equation was originally derived using experiments at rates of .01 –

$100 \frac{mN}{s}$  which is at least ten orders of magnitude difference using a micropipette and

correlates more closely to the equibiaxial case, so a question arises if the equation is

applicable. The surface-tension curve for the 72x2.8y2.7 case has a loading rate  $\mathcal{R}_\sigma =$

$1.6e12 \frac{mN}{s}$  which is still larger than the lowest strip biaxial case. Therefore, the

calculated value will still be too low when compared to the recorded results which are

considerably higher than those found in the 72x1y0 case. Additionally, Koshiyama and

Wada (2011) obtained results similar in magnitude to those of Tomasini et al. (2010), but

they are loading at a much higher rate (1 m/s equibiaxial for a system  $\sim 40 \text{ nm}^2$ ) which,

under the assumption that POPC and DPPC behave similarly, should yield a loading rate

much higher than that of Tomasini et al. (2010). This seems to contradict the rate

dependence of the system which has been proven true both experimentally and in other

computational studies including Koshiyama and Wada (2011) themselves. Therefore, it

is likely the max stress is at least partially dependent on the force field being utilized or

some other system constraint.

Additionally, the strains at failure do not agree with other studies. In the present study, in terms of  $A/A_0$  to be consistent with other studies, failure occurred when  $A/A_0 = \sim 3.5$  for the equibiaxial case. Using their plot and estimating area at failure allows for  $A/A_0$  to be calculated for Koshiyama and Wada (2011) as  $\sim 2.2-2.5$  depending on the rate. Tomasini et al. (2010), however, appear to have failure at  $A/A_0 = \sim 2$  for all rates they tested. As for experimental data, they lyse at less than seven percent areal strain, but still cannot be compared directly to computational studies due to extreme rate differences.

## 5.5 Phospholipid Bilayer Size Effect

The size of the phospholipid bilayer did not affect the results of the stress at all. By just viewing the stress-strain curves, the two simulations would not be distinguishable. However, the pore formation is affected slightly. Initially, the larger structure does not appear to be forming smaller pores. This leads to a much higher value for  $\epsilon_{FirstPore}^{VM}$  as seen in Table 4.2. When viewing the image analysis plots, this trend is confirmed in Figure 4.12 where the 72x4y0 case's pore count far exceeds that of the 144x7.6y0 case. However, despite having fewer pores, the 144x7.6y0 case quickly exceeds the total pore area of the smaller system. Examining Figure 4.15 helps to explain this trend because the 144x7.6y0 case suddenly goes from having practically no significant pores to having a mean pore area much larger than that of the 72x4y0 case. This appears to follow the proposed idea that higher rates result in some catastrophic defect which results in pore formation by (E. Evans et al., 2003). Despite this, both systems had initial water penetration at practically the same time enforcing the idea that eventual failure is indeed a result of strain. The ability of the larger structure to more

effectively rearrange the phospholipids to prevent the initial pores from being detected suggests that the system may be able to maintain apparent stability more effectively as a larger structure, but this does not affect the final outcome when a defect does occur. However, the method of rearrangement for the phospholipids is beyond the scope of this study and must wait for more effective image analysis methods.

## 5.6 Stress States

The stress states have a distinct effect on the failure of the bilayer. Despite having relatively similar initial peak values, with the  $72 \times 2.8 \times 2.7$  and  $72 \times 3.6 \times 1.7$  cases almost being exactly the same, the strain to failure values are markedly different. Additionally, the  $72 \times 2.8 \times 2.7$  and  $72 \times 3.6 \times 1.7$  trends are drastically different from those of the  $72 \times 4 \times 0$  and  $72 \times 4 \times R$  cases. This can be explained by looking at the stress tensor curves in Figure 5.2. For the  $72 \times 4 \times 0$ , one of the pressures far exceeds the other. In order to reach a state of equilibrium, it attempts to decrease the magnitude of the larger stress while increasing the magnitude of the smaller stress. A similar trend is seen in the  $72 \times 4 \times R$  case, but in that case  $\sigma_{yy} \cong 0$ . This leads to the downward trends seen for these two cases. Similarly, for the  $72 \times 2.8 \times 2.7$  and  $72 \times 3.6 \times 1.7$  cases the stresses are much closer in magnitude which avoids the sudden change by one or both attempting to reach an equilibrium value except for the initial peak which is more dependent on the rate. It should be noted that this is the reason the  $72 \times 1 \times 0$  case from the rate comparison study did not experience the drop seen in other strip biaxial cases because, even though the stresses were different, they were close enough in magnitude that the correction did not dramatically affect the equivalent stress as significantly.

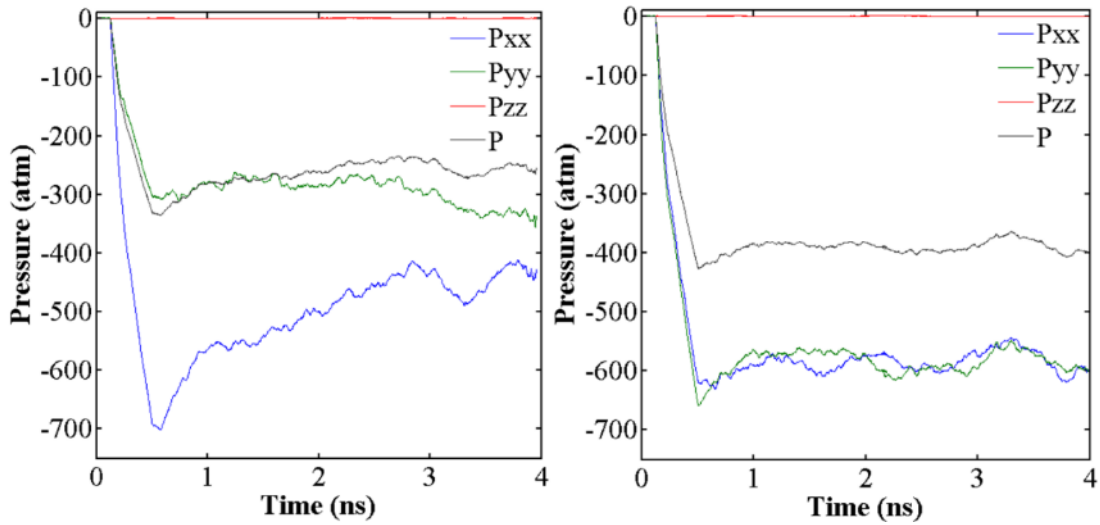


Figure 5.2 Comparison of principle pressures (stress) and overall pressure for the 72x4y0 (left) and 72x2.8y2.7 (right) cases.

So in the case of nonzero biaxial deformations, a higher equivalent stress is maintained during the deformation. Surprisingly, even though the x strain rate is approximately twice that of y in the 72x3.6y1.7 case, there is relatively little difference in the magnitude of the resulting stress ( $\sim 100$  atm at initial peak and less than that afterward). The maintained magnitude of stress potentially explains the decrease in the strain to failure as opposed to all the strip biaxial cases where the stress decreases to well below the initial peak value. This effect means that the strip biaxial cases will result in lower forces on the bilayer as the simulation progresses. Therefore, it is no surprise that the biaxial cases have much greater pore counts and larger pores than the strip biaxial case in the image analysis figures. Again, unexpectedly, the values for the two biaxial cases are very close to one another despite one being a factor of two to one deformation rates. This seems to indicate that the fact that it is being deformed biaxially is more significant than the ratio of the deformation rates. Indeed, viewing Figure 4.27 and

Figure 4.28 confirms how similar the two are due to both having similar peaks, trends, and final structures along with having multiple pores already visible at the point of water penetration. In contrast in Figure 4.26, the 72x4y0 case is much more intact at the end of the simulation. The uniaxial case was unique in that the small pore formation occurred much later in the simulation in the range of when the other cases were already experiencing water penetration and was of the same magnitude of the strip biaxial count for pores  $> .1 \text{ nm}^2$ . Additionally, it formed very few pores large enough to register as being  $> .1 \text{ nm}^2$  and as a result never suffered water penetration. This is easily viewable in Figure 4.29 where, even in the final snapshot, no pores are readily apparent. This is easily explained, however, when the fact that one of the dimensions restricting phospholipid motion was allowed to relax. This allowed the phospholipids to freely flow and fill the box as it deformed creating a state where they could more easily take positions that filled voids as they formed.

The strain space map in Figure 4.30 further displays how much more detrimental the biaxial cases are than the 72x4y0 case by graphically expressing where the first pore, the first stress peak, and failure curves lie. It is apparent that the biaxial cases will fail under much lower strains and should probably be given priority in the future. The increased first pore strain for the 72x3.6y1.7 case is interesting in that it is not on a standard curve that would be drawn for the other points. This could indicate that the 72x3.6y1.7 case allows a little more rearrangement during deformations than the 72x2.8y2.7 case. Additionally, because the bilayer is symmetric, it seems that the 72x3.6y1.7 case could be mirrored on the other side of the 72x2.8y2.7 case to further expand the strain space map.

## 5.7 Elastic Constants

Elastic constants were determined as mentioned in Section 3.3.2.3. Measured values indicate the phospholipid bilayer is a soft material as expected. When compared with published values, both the bulk modulus and the area compressibility modulus were off by one order of magnitude. For the bulk modulus  $K_b = 310 \text{ MPa} = .3 \text{ GPa}$ , the factor is off by  $\sim 10$  with published values of  $\leq 3 \text{ GPa}$  (Cevc, 1993). For the area compressibility modulus  $K_a = 1.9 \frac{\text{N}}{\text{m}}$ , it is off by a factor of 0.1 with published values of  $\sim 0.19 \frac{\text{N}}{\text{m}}$  (Needham & Nunn, 1990). So despite obtaining consistent values between measurements and calculating the area compressibility modulus using the bulk modulus, the resulting values are off by an order of two magnitudes. This would likely affect the results of the deformations and introduces uncertainty in regards to the magnitudes of the stress values. However, this would not affect the trend of rate dependence or the trend of some stress states being more detrimental. Additionally, this should not affect the strains at failure because the water penetration should not be affected by the phospholipid bilayer stiffness assuming the stiffness did not cause a delayed response in pore formation.

## 5.8 Relevance

The phospholipid bilayer model presented in this study is highly generic and, therefore, non-specific to traumatic brain injury. Therefore, results of pore formation due to deformations would be applicable to any potential mechanical cell injury. Cellular mechanical injuries can result from many traumatic scenarios including vehicular accidents, pressure blasts, and blunt impacts. These injuries potentially result in

mechanoporation of the phospholipid bilayer allowing molecules to penetrate the cell membrane according to their gradients disrupting the homeostasis of the cell. The outcome resulting from these molecules penetrating the cell membrane may include a loss of homeostasis and apoptosis, necrosis, or aponecrosis for the individual cells and overall damage to the tissue (Farkas & Povlishock, 2007).

However, it is unclear at this time whether pores that resulted during water penetration would necessarily be detrimental to the overall health of the cell. Larger pores would need to form for ions and large molecules to penetrate the membrane through mechanoporation. If only water penetration occurs, a cell would not suffer a loss of homeostasis if assuming it does not become hyper- or hypo-osmotic. This observation is assuming that in a real scenario the bilayer will be impacted by an impulse injury and allowed to relax as opposed to the current study where all simulations were allowed to continue deformations post water penetration.

## **5.9 Multiscale Modeling**

It is recommended that importing values for the local damage-based (von Mises) stresses and strains be incorporated into internal state variable models for better determination of failure on sub-macro scales. However, more studies should be conducted as described in Section 5.10.1 to verify and validate these values. Bulk, elastic, and shear moduli should also be incorporated into higher length scale models after the discrepancy between experimental material moduli and the measured simulation values are investigated further.

Even though it is the most common reference of stress for phospholipid bilayers, it is not recommended that surface tension be incorporated into current or future ISV



models due to its dependency on the bilayer height which will introduce nonconformity from other materials and will require additional effort to scale up the values into higher length scale models. However, it may be necessary to incorporate the area compressibility modulus in addition to typically used moduli due to the physical properties of the phospholipid bilayer being dominated in-plane rather than as a bulk three-dimensional material.

## **5.10 Future Work**

### **5.10.1 Verification and Validation**

#### **5.10.1.1 Further Analysis and Validation**

The results of the current study should be investigated further with a goal of validation. Currently, there is a question of whether the stress and strain values are accurate due to no experimental validation and discrepancies in the calculated elastic constants.

It is believed that the discrepancy in the elastic constants should be addressed first and then to search for further experimental results in the form of derivations that may validate the values obtained in the study.

#### **5.10.1.2 Comparative Studies for Verification**

If no experimental data can validate the results, then replicating at least a subset of the simulations in another MD simulation software with the CHARMM36 all-atom lipid force field for verification should be considered. Some possible programs to do this are CHARRM, GROMACS, or AMBER, but the final choice will depend on the abilities of each to mimic the current studies as closely as possible.

### **5.10.1.3 Comparative Study with Other Force Fields**

As an alternative form of validation assuming no experimental way is found, another force field could be potentially used to perform the same simulations. This would depend on how easily the force field could be ported into LAMMPS and made to model the current system. Two potential force fields would be a selection from the AMBER or OPLS force field lines.

Although this would not be a true validation as done with experimental test results, it could provide a roundabout validation if any results are within some relative error of one another. A good example would be if the simulations all yielded strain values that were within some pre-determined percentage of the current study's results to allow for simulation error.

### **5.10.2 Add Model Complexity**

The current model was highly simplified in nature when compared to the true cell membrane. To create a more complex model, a number of different aspects can be explored. This is especially important when attempting to create any simulation that is specialized for a particular part of the body.

The first potential addition would be to add ions in the water to determine if they would truly penetrate the bilayer during the simulation time. It is possible statistically, assuming it is possible for the ion penetration would occur, to perform this simulation using typical molecular dynamics. However, this may not be an efficient simulation method and the possibility of steered molecular dynamics should potentially be explored in conjunction with introducing an ion gradient.

The second potential addition would be a more varied phospholipid composition. This addition actually has two parts that could be addressed. The first would likely need to be the introduction of other types of phospholipids. This is imperative for a more realistic value of the bilayer because the bilayer's properties depend on the type of phospholipids present. Second would be to account for the phospholipid inequality between the bilayer leaflets. This addition would be taking the introduction of different phospholipids and arranging them preferentially to the inner or outer leaflet based on known values for specific systems.

The third potential addition would be to add cholesterol to the phospholipid bilayer. It is well known that cholesterol affects the stiffness of the bilayer which makes it of particular interest in the case of mechanical deformations. Additionally, this would be another way to specialize membrane models for specific types of cells.

The fourth potential addition would be portions of the cytoskeleton. Although computationally speaking, it may be more appropriate to treat this addition as a simulation of its own assuming the result could be related back to those of the phospholipid bilayer.

The fifth potential addition would be a small protein or rigid body representing a protein body. This would primarily be intended to serve as pre-existing object that would create an additional restraint when deforming the bilayer to determine if the bilayer fails more easily when objects similar to proteins are inserted.

### **5.10.3 Other Stress States**

In the current study, it has been determined that out of those tested the biaxial deformation conditions were the most detrimental. However, additional stress states exist

that can be tested to further elucidate the deformation and failure of the phospholipid bilayer. Two stress states immediately come to mind that would provide potentially relevant data with regard the motivation of TBI.

The first is compression which would be potentially experienced during a multitude of injury situations. Two immediately come to mind: contusions due to the brain impacting the interior of the skull and blast wave damage. These would result in two lines of simulations depending on rate because the blast wave simulation would result in much higher strain rates than that of normal injury.

The second is shear which can be experienced during TBI diffuse axonal injury (DAI). During DAI, the neuron axon fiber experiences shear which can lead to damage leading to eventual cell death. Performing simulations shearing the bilayer will help to determine if this damage is partially due to bilayer failure or purely an effect of the underlying cytoskeletal damage.

## CHAPTER VI

### CONCLUSIONS

The current study has examined the deformation characteristics of a simplified phospholipid bilayer computationally when placed under a varying strain rates, model sizes, and stress states and three potential properties that could be passed to higher length scale simulations. It was found that the maximum stress is dependent on the strain rate applied, the phospholipid bilayer size does not have an effect on either stress or strain at failure, and the stress state affects the strain at failure.

Additionally, local von Mises stresses and strains along with material moduli would serve as better properties for scaling up in a multiscale internal state variable model than surface tension due to surface tension's dependence on the phospholipid bilayer height.

## REFERENCES

- B., R. V., & B., A. V. (2013). *Overview About Lipid Structure* (P. R. V. Baez Ed.): InTech.
- Barbee, K. A. (2006). Mechanical Cell Injury. *Annals of the New York Academy of Sciences*, 1066(1), 67-84. doi: 10.1196/annals.1363.006
- Bosia, F., Buehler, M. J., & Pugno, N. M. (2010). Hierarchical simulations for the design of supertough nanofibers inspired by spider silk. *Phys Rev E Stat Nonlin Soft Matter Phys*, 82(5 Pt 2), 056103.
- Bramhall, J. (1986). Phospholipid packing asymmetry in curved membranes detected by fluorescence spectroscopy. *Biochemistry*, 25(11), 3479-3486. doi: 10.1021/bi00359a057
- Bratzel, G., & Buehler, M. J. (2012). Sequence-structure correlations in silk: Poly-Ala repeat of *N. clavipes* MaSp1 is naturally optimized at a critical length scale. *Journal of the Mechanical Behavior of Biomedical Materials*, 7(0), 30-40. doi: <http://dx.doi.org/10.1016/j.jmbbm.2011.07.012>
- Cernak, I., Stoica, B., Byrnes, K. R., Giovanni, S. D., & Faden, A. I. (2005). Role of the Cell Cycle in the Pathobiology of Central Nervous System Trauma. *Cell Cycle*, 4(9), 1286-1293.
- Cevc, G. (1993). *Phospholipids Handbook*: CRC Press.
- Cloots, R. J. H., Gervaise, H. M. T., van Dommelen, J. A. W., & Geers, M. G. D. (2008). Biomechanics of Traumatic Brain Injury: Influences of the Morphologic Heterogeneities of the Cerebral Cortex. *Annals of Biomedical Engineering*, 36(7), 1203-1215. doi: 10.1007/s10439-008-9510-3
- Colgan, N. C., Gilchrist, M. D., & Curran, K. M. (2010). Applying DTI white matter orientations to finite element head models to examine diffuse TBI under high rotational accelerations. *Progress in Biophysics and Molecular Biology*, 103(2-3), 304-309. doi: <http://dx.doi.org/10.1016/j.pbiomolbio.2010.09.008>
- Cranford, S. W., & Buehler, M. J. (2012). *Biomateriomics*: Springer.
- Cummings, J. L. (1993). FRontal-subcortical circuits and human behavior. *Archives of Neurology*, 50(8), 873-880. doi: 10.1001/archneur.1993.00540080076020

- Evans, E., Heinrich, V., Ludwig, F., & Rawicz, W. (2003). Dynamic tension spectroscopy and strength of biomembranes. *Biophys J*, 85(4), 2342-2350. doi: 10.1016/S0006-3495(03)74658-X
- Evans, E., Heinrich, V., Ludwig, F., & Rawicz, W. (2003). Dynamic Tension Spectroscopy and Strength of Biomembranes. *Biophys J*, 85(4), 2342-2350. doi: [http://dx.doi.org/10.1016/S0006-3495\(03\)74658-X](http://dx.doi.org/10.1016/S0006-3495(03)74658-X)
- Evans, E., & Smith, B. A. (2011). Kinetics of Hole Nucleation in Biomembrane Rupture. *New J Phys*, 13. doi: 10.1088/1367-2630/13/9/095010
- Farkas, O., & Povlishock, J. T. (2007). Cellular and subcellular change evoked by diffuse traumatic brain injury: a complex web of change extending far beyond focal damage. In T. W. John & I. R. M. Andrew (Eds.), *Progress in Brain Research* (Vol. Volume 161, pp. 43-59): Elsevier.
- Faul, M., Xu, L., Wald, M. M., & Coronado, V. G. (2010). *Traumatic Brain Injury in the United States: Emergency Department Visits, Hospitalizations, and Deaths 2002-2006*. Atlanta (GA): Centers for Disease Control Prevention, National Center for Injury Prevention and Control.
- Fontaine, R. N., Adron Harris, R., & Schroeder, F. (1979). Neuronal membrane lipid asymmetry. *Life sciences*, 24(5), 395-399.
- FRYE, L. D., & EDIDIN, M. (1970). The Rapid Intermixing of Cell Surface Antigens After Formation of Mouse-Human Heterokaryons. *Journal of Cell Science*, 7(2), 319-335.
- Holz, M., Heil, S. R., & Sacco, A. (2000). Temperature-dependent self-diffusion coefficients of water and six selected molecular liquids for calibration in accurate 1H NMR PFG measurements. *Physical Chemistry Chemical Physics*, 2(20), 4740-4742. doi: 10.1039/B005319H
- Hormel, T. T., Kurihara, S. Q., Brennan, M. K., Wozniak, M. C., & Parthasarathy, R. (2014). Measuring Lipid Membrane Viscosity Using Rotational and Translational Probe Diffusion. *Physical Review Letters*, 112(18), 188101.
- Horstemeyer, M., Baskes, M., Prantil, V., Philliber, J., & Vonderheide, S. (2003). A multiscale analysis of fixed-end simple shear using molecular dynamics, crystal plasticity, and a macroscopic internal state variable theory. *Modelling and Simulation in Materials Science and Engineering*, 11(3), 265.
- Horstemeyer, M. F. (2012). *Integrated Computational Materials Engineering (ICME) for Metals: Using Multiscale Modeling to Invigorate Engineering Design with Science*: Wiley.

- Klauda, J. B. (n.d.). Laboratory of Molecular & Thermodynamic Modeling. Retrieved June 23, 2010, from [http://mackerell.umaryland.edu/CHARMM\\_ff\\_params.html](http://mackerell.umaryland.edu/CHARMM_ff_params.html)
- Klauda, J. B., Venable, R. M., Freites, J. A., O'Connor, J. W., Tobias, D. J., Mondragon-Ramirez, C., . . . Pastor, R. W. (2010). Update of the CHARMM All-Atom Additive Force Field for Lipids: Validation on Six Lipid Types. *The Journal of Physical Chemistry B*, *114*(23), 7830-7843. doi: 10.1021/jp101759q
- Koshiyama, k., & Wada, S. (2011). Molecular dynamics simulations of pore formation dynamics during the rupture process of a phospholipid bilayer caused by high-speed equibiaxial stretching. *J Biomech*, *44*(11), 2053-2058. doi: 10.1016/j.jbiomech.2011.05.014
- Kraus, M. F., Susmaras, T., Caughlin, B. P., Walker, C. J., Sweeney, J. A., & Little, D. M. (2007). White matter integrity and cognition in chronic traumatic brain injury: a diffusion tensor imaging study. *Brain*, *130*(10), 2508-2519. doi: 10.1093/brain/awm216
- Laboratory of Computational Biology, National Heart, Lung, and Blood Institute, National Institutes of Health, Bethesda, MD 20892. (n.d.). Retrieved June 23, 2010, from <http://www.lobos.nih.gov/mbs/index.shtml>
- Leach, A. (2001). *Molecular Modelling: Principles and Applications (2nd Edition)*: Prentice Hall.
- Leontiadou, H., Mark, A. E., & Marrink, S. J. (2004). Molecular dynamics simulations of hydrophilic pores in lipid bilayers. *Biophys J*, *86*(4), 2156-2164. doi: 10.1016/S0006-3495(04)74275-7
- Liu, B., & Qiu, X. (2009). How to compute the atomic stress objectively? *Journal of Computational and Theoretical Nanoscience*, *6*(5), 1081-1089.
- Menon, D. K., Schwab, K., Wright, D. W., & Maas, A. I. (2010). Position Statement: Definition of Traumatic Brain Injury. *Archives of physical medicine and rehabilitation*, *91*(11), 1637-1640.
- Needham, D., & Nunn, R. S. (1990). Elastic deformation and failure of lipid bilayer membranes containing cholesterol. *Biophys J*, *58*(4), 997-1009. doi: [http://dx.doi.org/10.1016/S0006-3495\(90\)82444-9](http://dx.doi.org/10.1016/S0006-3495(90)82444-9)
- Ovalle-García, E., Torres-Heredia, J. J., Antillón, A., & Ortega-Blake, I. n. (2011). Simultaneous Determination of the Elastic Properties of the Lipid Bilayer by Atomic Force Microscopy: Bending, Tension, and Adhesion. *The Journal of Physical Chemistry B*, *115*(16), 4826-4833. doi: 10.1021/jp111985z



- Pastor, R. W., & MacKerell, A. D. (2011). Development of the CHARMM Force Field for Lipids. *The Journal of Physical Chemistry Letters*, 2(13), 1526-1532. doi: 10.1021/jz200167q
- Picas, L., Milhiet, P.-E., & Hernández-Borrell, J. (2012). Atomic force microscopy: A versatile tool to probe the physical and chemical properties of supported membranes at the nanoscale. *Chemistry and Physics of Lipids*, 165(8), 845-860. doi: <http://dx.doi.org/10.1016/j.chemphyslip.2012.10.005>
- Plimpton, S. (1995). Fast Parallel Algorithms for Short-Range Molecular Dynamics. *Journal of Computational Physics*, 117(1), 1-19. doi: <http://dx.doi.org/10.1006/jcph.1995.1039>
- Pronk, S., Páll, S., Schulz, R., Larsson, P., Bjelkmar, P., Apostolov, R., . . . Lindahl, E. (2013). GROMACS 4.5: a high-throughput and highly parallel open source molecular simulation toolkit. *Bioinformatics*, 29(7), 845-854. doi: 10.1093/bioinformatics/btt055
- R. Prabhu, M. F. H., Y. Mao, J. Bouvard, E. B. Marin, L. N. Williams, J. Liao. (2014). Simulation Based Analysis of an Experimentally Quantified Traumatic Brain Injury from an In-Theater Blast Explosion. (*Under review, PNAS*).
- Rasband, W. S., ImageJ, U. S. National Institutes of Health, Bethesda, Maryland, USA, <http://imagej.nih.gov/ij/>. (1997-2014).
- Schneider, C. A., Rasband, W. S., & Eliceiri, K. W. (2012). NIH Image to ImageJ: 25 years of image analysis. *Nature Methods*, 9(7), 671-675. doi: 10.1038/nmeth.2089
- Singer, S. J., & Nicolson, G. L. (1972). The Fluid Mosaic Model of the Structure of Cell Membranes. *Science*(4023), 720. doi: 10.2307/1733071
- Stukowski, A. (2010). Visualization and analysis of atomistic simulation data with OVITO—the Open Visualization Tool. *Modelling and Simulation in Materials Science and Engineering*, 18(1), 015012.
- Thom, F. (2009). Mechanical properties of the human red blood cell membrane at -15 degrees C. *Cryobiology*, 59(1), 24-27. doi: <http://dx.doi.org/10.1016/j.cryobiol.2009.04.001>
- Tieleman, D. P., Leontiadou, H., Mark, A. E., & Marrink, S. J. (2003). Simulation of pore formation in lipid bilayers by mechanical stress and electric fields. *J Am Chem Soc*, 125(21), 6382-6383. doi: 10.1021/ja029504i
- Tolpekina, T. V., den Otter, W. K., & Briels, W. J. (2004). Simulations of stable pores in membranes: system size dependence and line tension. *J Chem Phys*, 121(16), 8014-8020. doi: 10.1063/1.1796254

- Tomasini, M. D., Rinaldi, C., & Tomassone, M. S. (2010). Molecular dynamics simulations of rupture in lipid bilayers. *Exp Biol Med (Maywood)*, 235(2), 181-188. doi: 10.1258/ebm.2009.009187
- Wang, J., Wolf, R. M., Caldwell, J. W., Kollman, P. A., & Case, D. A. (2004). Development and testing of a general amber force field. *Journal of Computational Chemistry*, 25(9), 1157-1174. doi: 10.1002/jcc.20035
- Worthington, C. t., & Kharf, R. (1978). Structure determination of lipid bilayers. *Biophys J*, 23(3), 407-425.
- Zhang, Y., Feller, S. E., Brooks, B. R., & Pastor, R. W. (1995). Computer simulation of liquid/liquid interfaces. I. Theory and application to octane/water. *J Chem Phys*, 103(23), 10252-10266. doi: <http://dx.doi.org/10.1063/1.469927>
- Zhou, M. (2003). A new look at the atomic level virial stress: on continuum-molecular system equivalence. *Proceedings of the Royal Society of London. Series A: Mathematical, Physical and Engineering Sciences*, 459(2037), 2347-2392.
- Zimmerman, J., WebbIII, E., Hoyt, J., Jones, R., Klein, P., & Bammann, D. (2004). Calculation of stress in atomistic simulation. *Modelling and Simulation in Materials Science and Engineering*, 12(4), S319.

APPENDIX A  
FORCE FIELD PARAMETERS

The following parameters were used in the LAMMPS data file

Masses

1	1.008
2	1.008
3	1.008
4	1.008
5	1.008
6	1.008
7	12.011
8	12.011
9	12.011
10	12.011
11	12.011
12	12.011
13	14.007
14	15.9994
15	15.9994
16	15.9994
17	15.9994
18	15.9994
19	30.974

Pair Coeffs

1	0.046	1.24726	0.046	1.24726
2	0	0	0	0
3	0.022	2.35197	0.022	2.35197
4	0.028	2.38761	0.028	2.38761
5	0.024	2.38761	0.024	2.38761
6	0.031	2.22725	0.031	2.22725
7	0.07	3.56359	0.07	3.56359
8	0.02	4.05359	0.01	3.38542
9	0.056	3.58141	0.01	3.38542
10	0.078	3.63487	0.01	3.38542
11	0.08	3.6705	0.01	3.38542
12	0.068	3.72396	0.068	3.72396
13	0.2	3.29632	0.2	3.29632
14	0.12	3.02906	0.12	2.49452
15	0.102	3.188	0.102	3.188
16	0.1	2.93997	0.1	2.93997
17	0.12	3.02906	0.12	3.02906
18	0.1	2.93997	0.1	2.93997
19	0.585	3.83086	0.585	3.83086

### Bond Coeffs

1	440	1.34
2	365	1.502
3	360.5	1.1
4	200	1.522
5	750	1.22
6	150	1.334
7	222.5	1.538
8	309	1.111
9	340	1.43
10	222.5	1.53
11	222.5	1.528
12	309	1.111
13	300	1.08
14	215	1.51
15	340	1.43
16	340	1.43
17	322	1.111
18	300	1.08
19	215	1.51
20	0	1.5139
21	450	0.9572
22	580	1.48
23	270	1.6

### Angle Coeffs

1	48	123.5	0	0
2	52	119.5	0	0
3	32	112.2	0	0
4	45	111.5	0	0
5	52	108	0	0
6	33	109.5	30	2.163
7	40	109.6	30	2.2651
8	40	109.6	30	2.2651
9	26.5	110.1	22.53	2.179
10	75.7	110.1	0	0
11	75.7	110.1	0	0
12	40	116	0	0
13	70	125	20	2.442
14	55	109	20	2.326
15	58.35	113.5	11.16	2.561
16	34.5	110.1	22.53	2.179
17	75.7	110.1	0	0

18	58.35	113.6	11.16	2.561
19	58	115	8	2.561
20	26.5	110.1	22.53	2.179
21	33.43	110.1	22.53	2.179
22	67.7	115	0	0
23	75.7	110.1	0	0
24	34.6	110.1	22.53	2.179
25	60	109.5	26	2.466
26	20	120	35	2.33
27	34.6	110.1	22.53	2.179
28	60	109.5	26	2.466
29	60	109.5	0	0
30	35.5	109	5.4	1.802
31	60	109.5	0	0
32	60	109.5	0	0
33	35.5	108.4	5.4	1.802
34	24	109.5	28	1.767
35	40	109.5	27	2.13
36	24	109.5	28	1.767
37	40	109.5	27	2.13
38	40	109.5	27	2.13
39	55	104.52	0	0
40	120	120	0	0
41	98.9	111.6	0	0
42	90	125.9	160	2.2576
43	80	104.3	0	0

Dihedral Coeffs

1	0.91	1	180	1
2	0.18	2	180	0
3	0.17	3	180	0
4	0.3	3	180	1
5	0.14	1	180	1
6	0.17	2	0	0
7	0.05	3	180	0
8	0.19	3	0	1
9	0	5	180	1
10	0.317	3	180	0
11	0.557	2	0	0
12	0.753	1	0	0
13	0.19	3	0	1
14	0	4	0	1
15	0.15	3	180	0
16	1.453	2	180	0
17	0.837	1	180	0

18	0	3	0	1
19	0.267	3	180	1
20	0.173	2	0	0
21	0.781	1	180	0
22	0	3	0	1
23	0.407	2	0	1
24	0.241	1	180	0
25	2.05	2	180	1
26	0.965	1	180	1
27	3.85	2	180	0
28	0.45	1	180	1
29	8.5	2	180	0
30	0.45	1	180	1
31	8.5	2	180	0
32	2.05	2	180	1
33	0.2	3	0	1
34	0	3	0	1
35	0.2	3	0	1
36	0.12	3	0	1
37	0.05	6	180	1
38	0	6	0	1
39	0.03	3	180	0
40	0.432	2	180	0
41	0.332	1	0	0
42	0.101	2	0	1
43	0.142	3	180	0
44	0.074	4	0	0
45	0.097	5	0	0
46	0.162	2	0	1
47	0.047	3	180	0
48	0.105	4	0	0
49	0.177	5	0	0
50	0.19	3	0	1
51	0.16	3	0	1
52	0.26	3	0	1
53	0.407	2	0	1
54	0.241	1	180	0
55	0.23	3	0	1
56	0.965	1	180	1
57	3.85	2	180	0
58	0.1	3	0	1
59	1.2	1	180	1
60	0.1	2	180	0
61	0.1	3	180	0
62	0.19	3	0	1

63	0.26	3	0	1
64	0.23	3	0	1
65	0.2	3	0	1
66	0.2	3	0	1
67	0.2	3	0	1
68	0	3	0	1
69	0	6	180	1
70	0	6	180	1
71	0.2	3	0	1
72	0.19	3	0	1
73	0.19	3	0	1
74	0.19	3	0	1
75	0.16	3	0	1
76	0	3	0	1
77	1	2	180	1
78	0.19	3	0	1
79	3.3	1	180	1
80	-0.4	3	180	0
81	-0.429	4	60	1
82	0.614	3	0	0
83	-0.115	2	60	0
84	0.703	1	180	0
85	0	4	0	1
86	0.607	3	180	0
87	0.254	2	60	0
88	2.016	1	180	0

Improper Coeffs

1	100	0
---	-----	---



APPENDIX B

MODEL RELAXATION OF THE 72x1y0 CASE

## **B.1 Methods**

Restart files pre- and post-penetration were taken from the 72x1y0 case. Both structures were allowed to relax using the NPT ensemble using the same parameters as during equilibration. The structure was assumed to be relaxed when the model volume began to equilibrate.

## **B.2 Results**

The resulting trend from allowing the structure to relax can be seen in Figure B.1. The von Mises stress for both the structure with water penetration and the structure without water penetration quickly drops down to nearly 0 MPa where it stays. Both structures begin to equilibrate at a von Mises strain of  $\sim 0.5$ .

Figure B.2 displays the resulting pore structures present after relaxation. No water bridges formed when the structures were relaxed and the water bridge resulting from deformation did not expand or close during relaxation. As a result, a thin two-water chain was maintained which kept a small pore open through the bilayer.

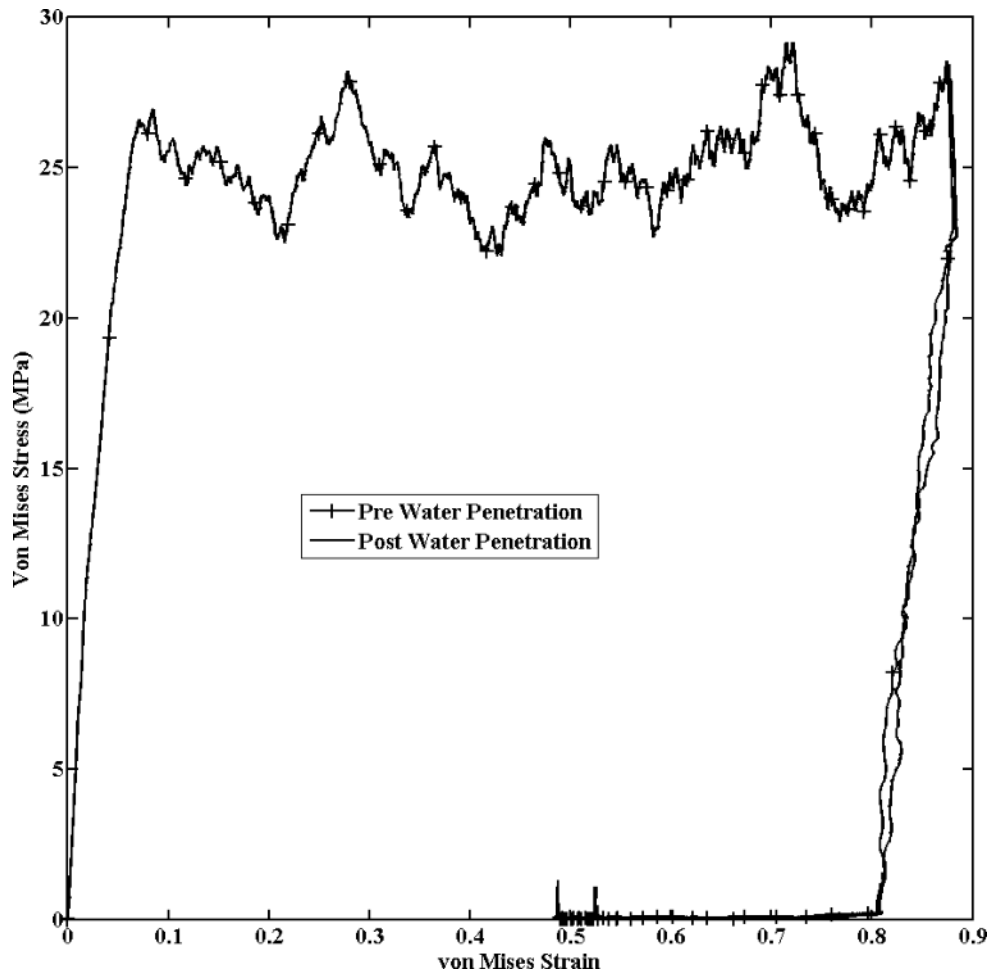


Figure B.1 Von Mises stress-strain curve displaying the effect from allowing the seventy-two phospholipid bilayer to relax after being subjected to 1 m/s strip biaxial tension deformation.

Notes: The lines diverge when the deformation conditions are removed so the box can relax.

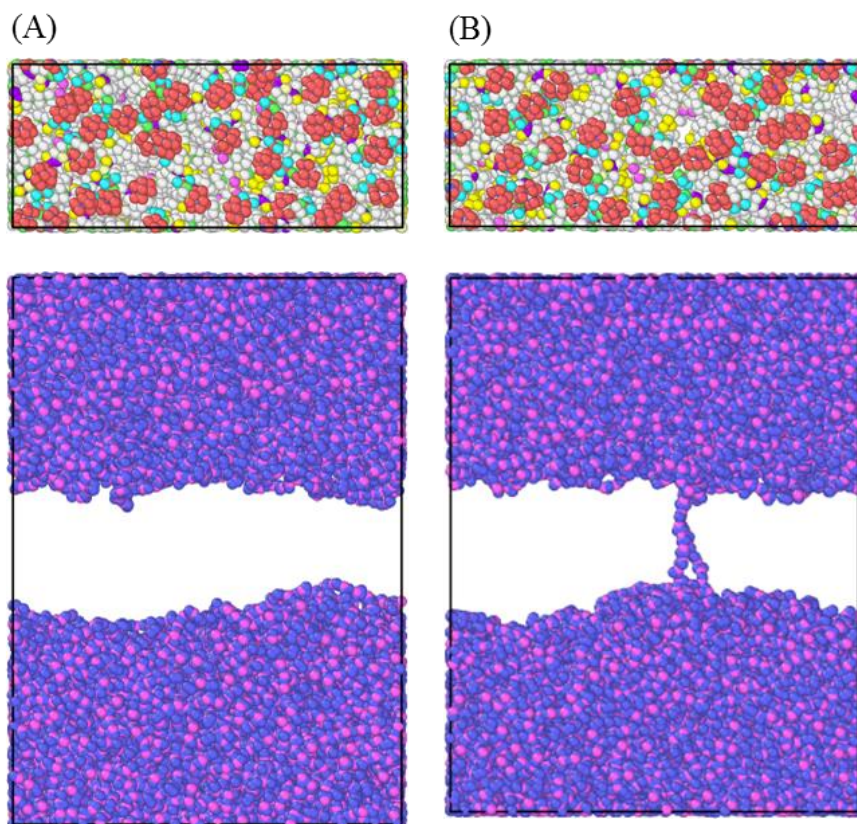


Figure B.2 Snapshots of the relaxation simulations after the volume has begun to equilibrate.

Notes: The top view with water hidden is shown on top and the side view with the phospholipids hidden is shown on bottom for (A) Relaxation initiation is performed prior to water penetration and (B) Relaxation initiation is performed after water penetration.

### B.3 Discussion

Allowing the structures to relax resulted in a minimum stress and a condition where the system was just trying to organize into a lowest energy state. For the structure where water bridges had yet to form, there was no incentive to create a water bridge and all pores that had formed but had not yet created a water bridge closed as the system relaxed. Similarly, for the structure where a water bridge had formed, all pores except the one ones that had formed the water bridge closed as the structure relaxed.

Additionally, the two water chains that initially connected forming the bridge remained

connected, but it was not energetically favorable for the water bridge to expand because this would require more waters being introduced into the hydrophobic region of the phospholipid bilayer. Instead, the waters that had already penetrated kept a small path open between the two leaflets and appears to attempt to minimize exposure from the phospholipid tails.

This thin chain of water would not be large enough to allow the transport of more detrimental ions or other larger molecules which indicates that damage to cells due to mechanoporation may be influenced by objects in the phospholipid bilayer which may not immediately allow the phospholipid bilayer to return to its initial structure.

Interestingly, neither structure returned to the volume of the undeformed simulation box. Rather, the simulation volume became stable when the structures were at approximately 0.5 von Mises strain indicating some change occurred.

APPENDIX C

DEFORMATION REVERSAL OF THE 72x1y0 CASE

## C.1 Methods

Restart files pre- and post-penetration were taken from the 72x1y0 case. Both structures were deformed using the same parameters as strip biaxial cases but with a reversed (compressive) velocity of 1 m/s. The structure was deformed until it reached the length of the pre-deformed structure.

## C.2 Results

The resulting trend from reversing the deformation can be seen in Figure C.1. The von Mises stress for both the structure with water penetration and the structure without water penetration initially decreases to  $\sim 5$  MPa at a von Mises strain of  $\sim 0.5$  but then begin to increase. The case with water penetration results in a maximum stress of  $\sim 45$  MPa when it reaches the pre-deformation box dimensions which is almost twenty megapascals greater than the von Mises stress seen during tensile deformations. The case that did not have water penetration followed a similar trend, but the stress when returned to pre-deformation dimensions was approximately five megapascals lower than the similar structure with water penetration.

Figure C.2 displays the resulting pore structures present after the deformation reversal. No water bridges formed when in the structure that was taken before any water bridges were formed, but the water bridge resulting from deformation expanded during the reverse deformation and another water bridge formed as well. These two water bridges eventually touch and join together. As a result, the initial water bridge became much thicker and expanded the size of the pore.

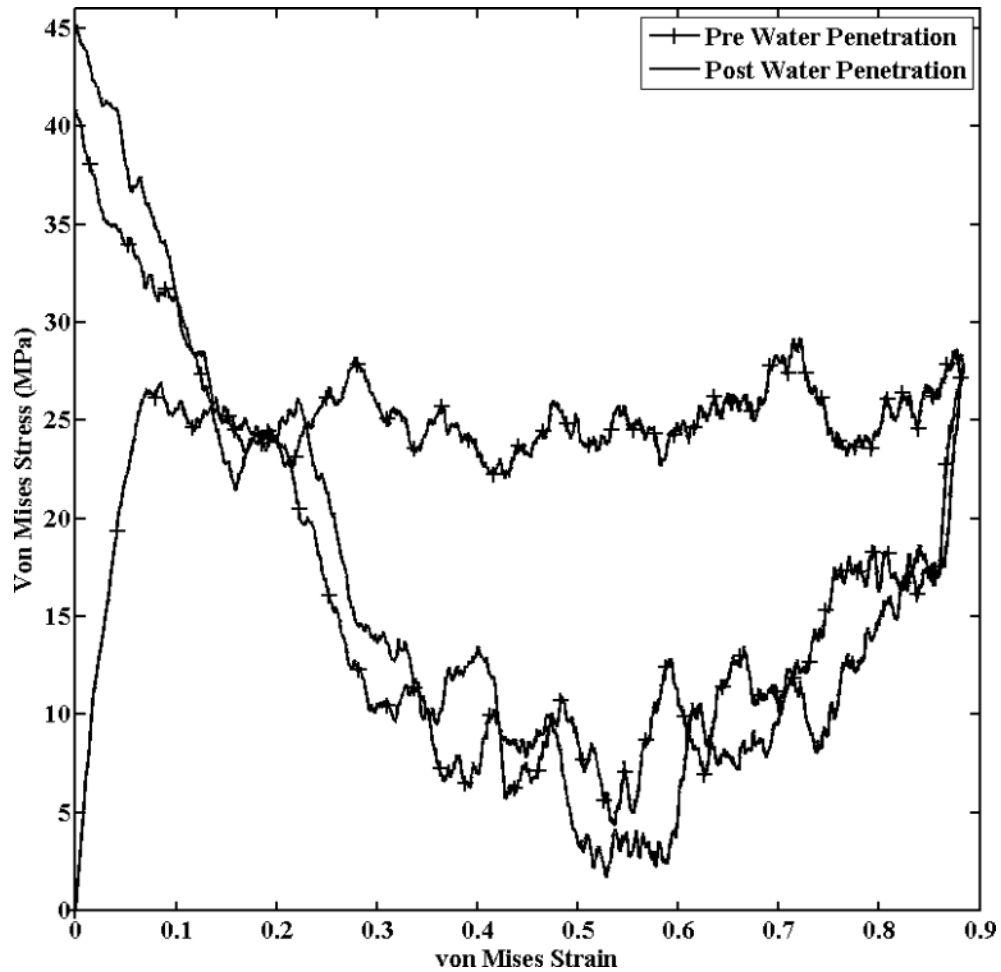


Figure C.1 Von Mises stress-strain curve displaying the effect from reversing the deformation velocity for the seventy-two phospholipid bilayer after being subjected to 1 m/s strip biaxial tension deformation.

Notes: The lines diverge where the reversed deformations are applied.



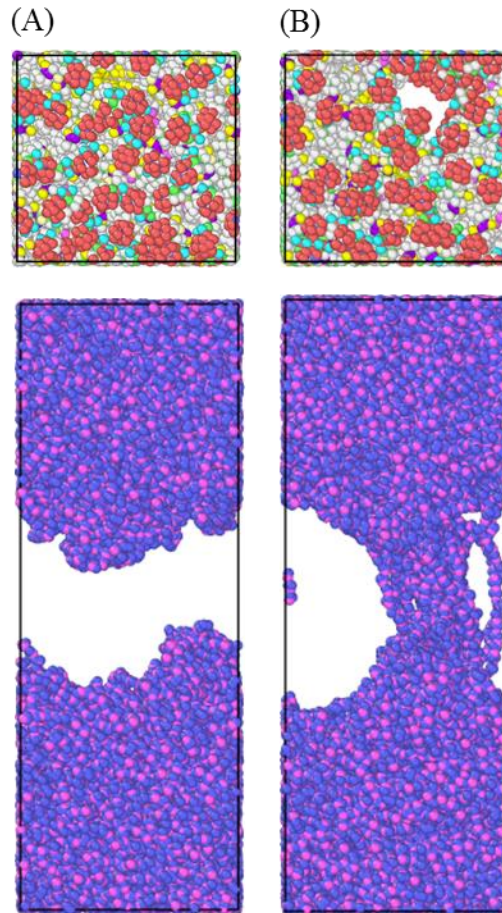


Figure C.2 Snapshots of the reversed deformation simulations when the simulation box has been returned to its original size.

Notes: The top view with water hidden is shown on top and the side view with the phospholipids hidden is shown on bottom for (A) Reversed deformation initiation is performed prior to water penetration and (B) Reversed deformation initiation is performed after water penetration.

### C.3 Discussion

Reversing the deformation of the phospholipid bilayer structure taken after water penetration resulted in sustained stresses which were great enough to cause the initial pore to expand and new pores large enough to sustain a water bridge to form. Although the structure taken before water penetration followed the same trend, it did not form any pores resulting in water bridges which may indicate that pores form more easily once a

pore already exists or simply that the extra expansion allowed the water to penetrate the phospholipid bilayer more easily.

Unlike the relaxation cases, the pore grows much larger when placed under reverse loading. This increase in pore size may indicate that the phospholipid bilayer is susceptible to repetitive deformations. It also shows that it may be possible for molecules larger than water to penetrate the phospholipid bilayer, but select ions or molecules will need to be tested individually along with verifying this behavior occurs in non-strip biaxial stress states.

The lowest stresses during the reverse deformations also occur at  $\sim 0.5$  von Mises strain. This is similar to the value found at the end of the relaxation simulations which further seems to indicate that the deformations seem to have some lasting effect on the structure which is keeping it from returning to the dimensions seen prior to deformations. Indeed, the von Mises stress increases considerably after going below  $.5$  von Mises strain and goes much higher than the stress seen during tensile deformations which indicates the original structure has become unfavorable.